Computational modelling of neurovascular coupling and the BOLD signal

Elshin Joel Mathias

Department of Mechanical Engineering
University of Canterbury

This dissertation is submitted for the degree of
Doctor of Philosophy

June 2017

Declaration

I hereby declare that except where specific reference is made to the work of others, the contents of this dissertation are original and have not been submitted in whole or in part for consideration for any other degree or qualification in this, or any other university. This dissertation is my own work and contains nothing which is the outcome of work done in collaboration with others, except as specified in the text and acknowledgements. This dissertation contains 133 pages including appendices, references, 4 tables and 41 figures.

Elshin Joel Mathias
June 2017

Acknowledgements

This journey would not have been possible if it's not for these few people in my life. First and foremost I would like to express my sincere gratitude to my supervisors Professor Tim David and Dr Michael Plank for sharing their wisdom, guiding me through every step and showering me with kindness and patience throughout this process. I am forever indebted to them for all that they have done for me. I would like to specially thank Professor Tim David for giving me funding for two years through UC HPC and for seven months through Brain Research New Zealand (BRNZ). I also thank of College of Engineering, University of Canterbury for providing a tuition fee scholarship. The funding gave me the time and energy to pursue the research questions with confidence.

I was able to come to New Zealand only because of the support and kindness of my loving family members Mathias Arullappan (Father), Jasmine Varuvel(Mother), Anne Nisha Mathias (Sister), Joseph Alexander Soosaimuthu (Brother in law), Fiona Alexander (Niece) and Ashik Shaun Alexander (Nephew). I would like to extend my gratitude and love for them. I would also like to thank my relatives back home for their continuous support and for taking care of my family in my absence. I would also like to thank Dr Jaijus Pallippadan Johny, Dr Sowmia Jaijus and Johan for giving me a feeling of home in Christchurch.

I extend my thanks to all my colleagues who were part of the BRATS research group especially Dr Katharina Dormanns, Dr Jaijus Pallippadan Johny, Dr Chirstine French, Dr Ealasukanthan Thavanayagam, Tim Van Ginkel, Michelle Goodman, Allanah Kenny, Stewart Dowding, Dr. Constantine Zakkaroff, Dr. Mohsin Shaikh, Grace Strijbis, Lisa Wiesent for their wonderful company and fruitful discussions. I would also like to convey my thanks to members of UC HPC centre for their encouragement and support. Special thanks to Angela Armstrong for her support and help all these years.

I would also like to thank Professor Tim David and Neurological Foundation of New Zealand for providing funding and the opportunity to attend the Australasian winter conferences on brain research (AWCBR) in Queenstown during 2014 and 2015 and the Computational Neuroscience and Neuromorphic Engineering Workshop in Queenstown during 2015.

Abstract

Normal brain function is critically dependent on a continuous supply of blood flow so that even a few seconds of disrupted blood flow can hinder brain function. Our body has employed tight regulatory mechanisms to maintain cerebral blood flow and avoid hyperemia or ischemia. One of the primary mechanisms in which the neurons communicate with the cerebral blood vessels to increase local blood flow to the region in need is termed as neurovascular coupling. Disordered neurovascular coupling has been observed in several brain pathologies such as hypertension, stroke and Alzheimer's disease. It is likely that the disruption of the interactions between neurons and the cerebral vasculature contributes to the initiation and progression of brain dysfunction. Hence understanding this coupling mechanism is of vital importance. Experimental exploration suggests that there are more than one factor controlling the vessel dilation during neural activation. Based on the observation that there are different vasoactive ions in different brain regions of the brain, researchers suggested that neurovascular coupling is brain region dependent. Another recent experiment illustrated that it is not just brain region dependent but also specific to the functions in a certain region of the brain as the same region can be connected to many other regions. This suggests that neurovascular coupling has to be explored based on the function that induces the vascular response. We have not yet arrived at a quantitative relationship of the cellular structures controlling neurovascular coupling primarily due to the complexity of the parameters involved and the difficulty of measuring them in the highly heterogeneous brain. Hence, developing mathematical models simultaneously based on experimental data which can be validated with repetitive experiments may help establish a quantitative relationship of the neurovascular coupling mechanism. To test the model built based on a hypothesis , the model must also be related to well established and accessible experimental technique. fMRI BOLD technique is one of the widely available non invasive experimental technique used to map the active regions in the brain. Even though it is used to study the functions of the brain, the method employed primarily utilizes the neurovascular response. So modelling the fMRI BOLD response based on the neurovascular reponse will enable to simulate an output that can be compared with the experimental data. The aim of this study is to model a certain hypothesis of neurovascular coupling based on experimental data and use it to model the fMRI BOLD response and

compare it to experimental data. A mathematical model was created based on different existing models to simulate the experimentally well supported K^+ signalling mechanism of neurovascular coupling and its associated fMRI BOLD response. Our model predicts the variations of the BOLD response such as initial dip, positive and negative BOLD signals, post stimulus undershoot arising due to the neurovascular and neurometabolic responses. These responses were simulated for different kinds of neural activities such as continuous spiking, bursting and cortical spreading depression. We compared the simulated BOLD response to experimental BOLD signals observed in the hippocampus and cortex under different conditions and it showed reasonably good agreement. While the results of the model suggests that potassium ions released during neural activity could act as the main mediator in neurovascular coupling, along with cytosolic calcium in the smooth muscle cell it certainly does not rule out the possibility of other mechanisms that can coexist and increase blood flow, such as the nitric oxide signalling mechanism or the archidonic acid to EET pathway. The discrepancy in the comparison between simulated and experimental data from the cortex indicates coexistence of other vasoactive factors. This approach of combined quantitative modelling of neurovascular coupling response and its BOLD response will enable more specific assessment of a brain region and could possibly enhance the understanding of the mechanism.

Table of contents

List of figures

List of tables

Abbreviations

20-HETE 20-hydroxy-eicosatetraenoic acid.

ANLSH astrocyte neuron lactate shuttle.

ATP Adenosine triphosphate.

BOLD Blood oxygen level dependent.

CBF cerebral blood flow.

CBV cerebral blood volume.

cGMP cyclic guanosine monophosphate.

$CMRO_2$ cerebral metabolic rate of oxygen.

ECS extracellular space.

EEG Electroencephalography.

EET epoxyeicosatrienoic acids.

fMRI function magnetic resonance imaging.

LTP long term potentiation.

MEG Magnetoencephalography.

NO Nitric oxid.

RF Radiofrequency.

TCA tricarboxylic acid.

Chapter 1

Introduction

1.1 Circulatory system and its regulation in the human body

The circulatory system's function is to mainly provide nutrients for the tissue in need. It also transports waste products away from the tissue and transports hormones from one part of the body to another, thus playing an integral part in maintaining the tissue microenvironment. The circulation is divided into the pulmonary circulation which supplies the lung tissues, coronary circulation which supplies the heart tissues and systemic or peripheral circulation which supplies all the other tissues of the body. The blood vessels in the systemic circulation, based on their size and functions are divided into aorta, artery, arteriole, capillary, venules, veins and venae cavae.The aorta is a large artery which carries blood away from the heart towards different regions of the body and venae cavae are large veins which returns blood back to the heart from other parts of the body. The immediate branches from the aorta are called arteries which have strong muscular walls to facilitate rapid blood flow under high pressure. The arterioles act as small branches between arteries and capillaries and its strong muscular and elastic wall enables it to dilate several fold to cater the needs of the tissue. The capillaries have very thin walls and they serve as an exchange medium between the blood vessels and tissues. The blood, after passing through the capillaries is collected by the venules and is later transported back to the heart through progressively larger veins. Even though the muscular walls of the veins are thin, depending on the needs of the circulation it can dilate and contract and thus act as a reservoir. At any instance, different parts of the circulation have different percentages of the total blood volume. About 64% of the blood volume is in the veins, 13% in the arteries, 7% in the arterioles and capillaries, 7% in the heart, and 9% in the pulmonary vessels [41]. The pulmonary circulation carries deoxygenated blood from the

heart to the lungs and returns oxygenated blood to the heart.
Fundamentally our body employs three principles to regulate blood flow [41]. Firstly, the heart behaves like an automaton wherein the cardiac output is mainly driven by the sum of all the local tissue flows which are returned to the heart by the veins. In addition to this, the nerve signals arising from different parts of the body also help to control the cardiac output more precisely to the needs. Secondly, the arterial pressure is controlled by an extensive system in the body which can function independently of any other regulatory mechanism in the body. Disturbance to normal pressure elicits nervous reflexes which bring about a series of circulatory changes to get the pressure back to normal. Some of these changes include altering blood flow and resistance in the artery. Also, hormone induced pressure control and blood volume induced pressure control are done by the kidneys over prolonged periods. Thirdly, the small arterioles in the circulation can alter its diameter according to the local tissue needs. Some of the local tissue needs include delivery of oxygen, glucose, amino acids and fatty acids, removal of carbon dioxide and hydrogen ions, maintaining concentrations of other ions and transport of useful substances to other regions. Many different theories derived from experimental evidence exist about how the local tissue needs to control the local blood flow. But none in isolation has been proved to explain the complete mechanism of local blood flow control [14].

1.2 Blood flow regulation in the brain

Despite having only 2% of the total body mass, the brain requires almost 15% of the cardiac output to continuously function [83]. The internal carotid and basilar arterial systems supply blood to the brain. These arterial systems are interconnected through a structure called the circle of Willis. The main function of this structure is to compensate and redirect blood flow to stenosed or blocked regions in the brain, thus preventing ischemia. Even though blood flow regulation in the human brain also follows the three fundamental principles applied to any other parts of the body, it is more complex, more regulated and less understood. The brain goes into unconscious state within 5 to 10 seconds of cessation of blood flow. To cater for such a high metabolic rate the blood flow in the brain is also regulated by an unique mechanism termed neurovascular coupling wherein the neurons upon activation communicates with the blood vessels to increase or decrease blood flow. Figure 1.1 shows the architecture of cerebral vasculature in rodents and the availability of different techniques to measure blood flow at different spatial scales. Pial vessels are intracranial vessels on the surface of the brain and they give rise to smaller arteries that eventually penetrate into the brain tissue called the

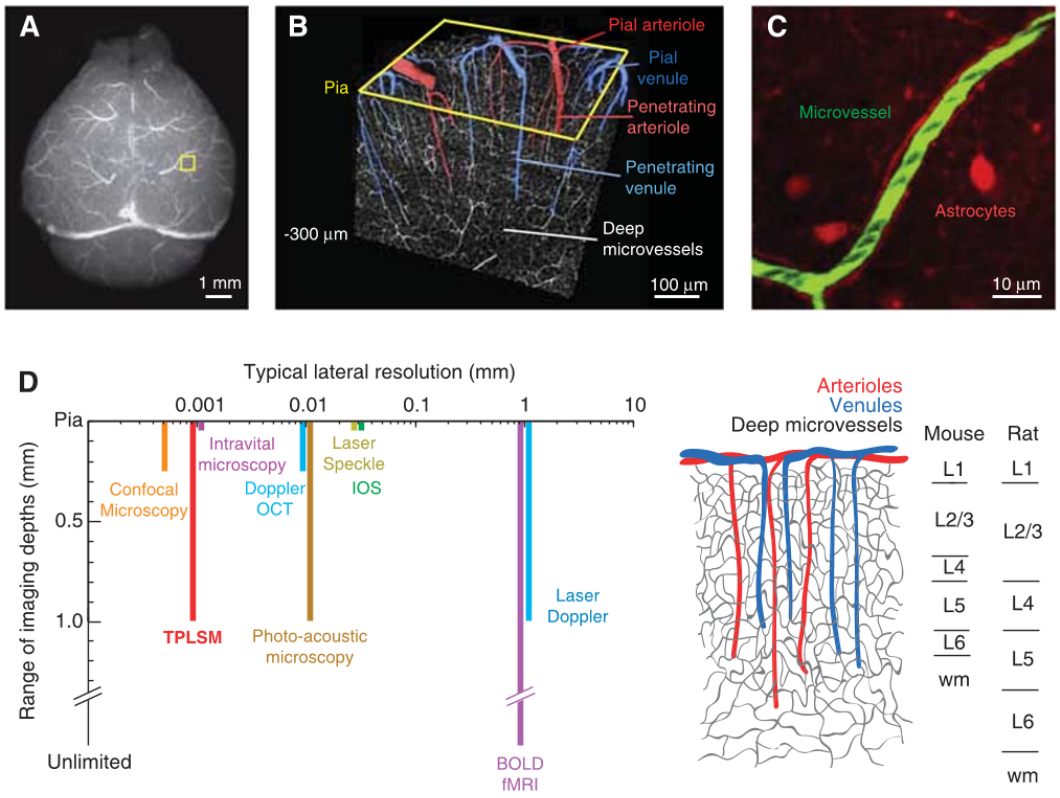

Fig. 1.1 Microarchitecture of rodent cerebral vasculature reproduced from Shih et al [88]. A) Widefield epi fluorescence image of a mouse brain perfused with a fluorescein conjugated gel and extracted from the skull. B) Three dimensional reconstruction of a block of tissue collected by in vivo two-photon laser scanning microscopy (TPLSM) from the upper layers of mouse cortex. C) In vivo image of a cortical capillary, 200 μm below the pial surface, collected using TPLSM through a cranial window in a rat. The blood serum is shown in green and astrocytes are shown in red. D) A plot of lateral imaging resolution against range of depths accessible for common in vivo blood flow imaging techniques. The panels to the right show a cartoon of cortical angioarchitecture for mouse, and cortical layers for mouse and rat in relation to imaging depth.

penetrating arteries. These arteries then are called parenchymal arteries once they penetrate the brain tissue where they are surrounded by astrocytic end feet as shown in Figure 1.1 B,C. In addition to the global blood flow control mechanisms that can regulate blood flow, neurovascular coupling also plays a significant role in catering the region's need. Figure 1.1 D shows the depths and resolution at which different experimental techniques can measure blood.

The cerebral micro environment has a unique ionic composition, establishing the basal conditions for controlling blood flow. The brain tissues are continuously in a bath of cerebrospinal fluid which are produced from the choroid plexus and delivered through the Virchow-Robin

space. Both the cerebrospinal fluid present in the brain tissues and plasma present in the blood have different ionic compositions. Hence the ion channel activity and therefore the membrane potential of the vascular smooth muscle cells can be controlled by these different ionic concentrations in the extracellular compartments. To dynamically regulate the vessel diameter, the ionic changes during neural activation and their influence on the smooth muscle cell's membrane potential is primarily employed. Though their central relationship is known, the exact signalling mechanisms which introduce such changes are still under debate. There is strong evidence to suggest that the star shaped glial cells, astrocytes play a major role in this signalling process. The astrocyte has processes called endfeet that surround the synapses and arterioles and are perfectly positioned to facilitate fast communication between the neuron and the vasculature. Recently, another cell type termed pericytes which wrap around capillaries is also believed to contribute to the neurovascular response as they are intrinsically contractile in nature.

1.3 Hypothesized signalling mechanisms controlling neurovascular coupling

The neurovascular coupling response is believed to be mediated by different signalling mechanisms. This signalling has been explored for over a century due to its essential importance in maintaining normal brain functions. At first in 1890 when Roy and Sherrington [83] proposed this mechanism they reasoned it out with a metabolic negative feedback theory. According to this theory, neural activity leads to a drop in oxygen or glucose levels and increases in CO_2, adenosine, lactate levels. All of these signals could dilate arterioles and hence were believed to be part of neurovascular response. However, recent experiments illustrated that the neurovascular coupling response is partially independent of these metabolic signals [63, 66, 72, 79, 68]. An alternative to this theory was proposed where the neuron releases signalling molecules to directly or indirectly affect the blood flow. Many signalling pathways are found to contribute to the neurovascular respose so far [5].

The K^+ signalling mechanism of neurovascular coupling is supported by many strong evidences. This hypothesis mainly utilizes the astrocyte which is perfectly positioned to enable the communication between the neurons and the blood vessels. The astrocyte and the endothelial cells exhibit a striking similarity in the ion channel expression and this can enable it to control the smooth muscle cell from both the neuronal and the side of the blood vessel [67]. Whenever there is neuronal activation potassium ions are released into the extracellular

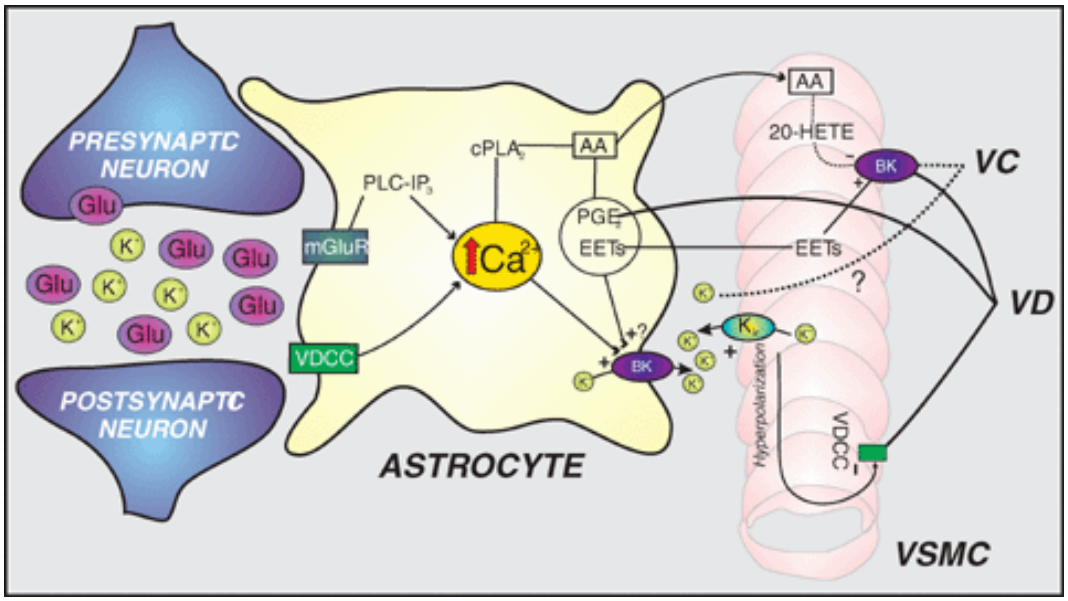

Fig. 1.2 Figure illustrating some of the possible neurovascular coupling signalling mechanisms reproduced from Filosa et al [28]. The activation of the BK channels in the astrocytic endfeet during neuronal activation will cause elevations in perivascular potassium which can lead to K^+ efflux from the vascular smooth muscle cell (VSMC) through the KIR channel causing membrane hyperpolarization and hence dilation through inactivated voltage dependent calcium channels (VDCC). Arachidonic acid metabolites such as EETs and 20-HETE can cause vasodilation (VD) or vasoconstriction (VC) respectively.

space. The astrocyte gets depolarized by taking up potassium released by the neuron and releases it in the endfeet near the arterioles through the BK channels [28]. This increase in extracellular space potassium concentration (3-10mM) near the arteriole hyperpolarizes the smooth muscle cell through the KIR channel and causes dilation. The BK channel in the astrocyte can also be activated by the glutamate released in the synapse during neural activity. Astrocytes have metabotropic glutamate receptors (mGLuRs) situated in the endfeet which get activated by the glutamate released, inducing an increase in calcium concentration in the astrocyte. The BK channels are activated in response to this increase in calcium concentration which then induces dilation through the mechanisms shown in Figure 1.2.

The activation of glutamate receptor in the astrocyte during neural activity can also lead to the production of arachidonic acid metabolites such as epoxyeicosatrienoic acids (EET) which can also dilate the arteriole [103]. EETs are known to coexist with the K^+ signalling mechanism [14]. The arachidonic acids are produced from membrane phospholipids due to the rise in calcium concentration in the astrocyte. These phospholipids can also produce prostaglandins which can also dilate the vessels. When the enzyme CYP4A from the smooth muscle cell comes in contact with arachidonic acid, it produces the metabolite 20-hydroxy-

eicosatetraenoic acid (20-HETE) which leads to constriction of blood vessels [73]. Oxygen is known to modulate the neurovascular coupling response by modulating the production of 20-HETE. Decrease in oxygen concentrations decreases the production on 20-HETE [43]. Nitric oxide(NO) is produced in both the neuron and endothelial cells and have been observed to modulate neurovascular coupling through some pathways. Inhibiting nitric oxide production in different regions of the brain decreased blood flow by different percentages [46]. This showed that in different regions the action of NO modulation is different. It modulates the production of EETs and 20-HETEs and hence can affect both dilation and constriction [82]. It can also modulate dilation through the production of cyclic guanosine monophosphate (cGMP). Both the NO produced from neuron and endothelial cells are found to increase the activity of BK channels in astrocytes and smooth muscle cells [92].
The hypothesis discussed so far has different signalling pathways but all of them alter blood flow to the tissues by modulating the smooth muscle cell. Recent experiments have demonstrated that the capillary diameter itself could be altered by the pericytes surrounding them at 50μm intervals. Pericytes are also known to express contractile proteins. During neural activity, pericytes are observed in brain slices to dilate and constrict in response to glutamate and noradrenaline released respectively [78].Even though pericyte's contribution to blood flow regulation is demonstrated invivo during ischemic conditions [100], it is yet to to be tested under physiologic conditions [42].
The functional variations of a certain region connected to distinct neuronal networks in the brain are also reflected in the neurovascular response when it is stimulated through different pathways. Stimulation of the somatosensory cortex through activation of thalamocortical and transcallosal corticocortical pathways evokes cerebral blood flow by releasing different vasoacitve factors[26]. In addition to that Enager et al also found that the amplitude of this vascular response was different for both stimulus conditions. All these different hypotheses of neurovascular coupling based on experimental evidences makes it clear that neurovascular coupling is a function specific response and more than one type of vasoactive factor is released during any kind of neural activity and they can all act in concert to give a resultant neurovascular response. This makes it extremely important to study the neurovascular response with respect to a the neural function and the associated vasoactive factors released to get the quantitative relationship between them.

1.4 fMRI and its basic principles

Function Magnetic Resonance Imaging(fMRI)is a widely used non-invasive brain imaging technique for studying brain activation. These functional responses are studied by designing appropriate experiments based on a specific hypothesis of that response. The functional responses can range from baseline brain activity to complex cognitive functions. fMRI has both clinical and experimental applications. Surgical planning is done by using well defined protocols to map the auditory, visual, motor and language functions. It is also used to monitor progress in patients recovering from stroke and to understand the extent of damage in cortical functions for patients having neurodegenerative disorders such as Alzheimer's disease [50]. There are certain advantages and disadvantages to fMRI compared to other neuroimaging techniques. To state a few, fMRI is non invasive and its contrast agent is endogenous unlike Positron Emission Tomography(PET). Even though the temporal resolution of fMRI which is of the order of seconds and is better than PET which is in the order of tens of seconds, Electroencephalography(EEG) or Magnetoencephalography(MEG) has much better temporal resolution than fMRI in the order of milliseconds. However EEG and MEG cannot be used to measure the activity of deep structures in the brain. The spatial resolution of fMRI is approximately 2mm cubed voxels for a magnetic strength of 1.5-3 Tesla. Higher magnetic strength will give better spatial resolution [12].

Blood Oxygen Level Dependent(BOLD) contrast is the most common type of fMRI image obtained. It is feasible due to the fact that deoxyhemoglobin is paramagnetic and hence sensitive to the magnetic resonance scanner. A paramagnetic material's nuclei has an odd number of protons or neutrons and is characterized by a non zero spin and an associated nuclear magnetic moment. When a huge magnetic field is applied, the nuclear magnets precess around the applied magnetic field with an angular momentum. This frequency of precession is called Larmor frequency and the direction of precession is either parallel or anti-parallel to the applied magnetic field. These nuclear magnets have a net magnetisation as a result of them aligned in both parallel and anti-parallel directions. When a RadioFrequency(RF) pulse is applied at the Larmor frequency, the net magnetisation of nuclear magnet moves out of alignment and hence the it starts to precess around the magnetic field creating a oscillating magnetic field. This can be detected with a coil. The time it takes for the nuclear magnet to come back to its original state of alignment with the huge magnetic field is called T1 and T2 is the time constant for decay of the signal induced in the RF coil. TE or echo time is the interval between the time of RF pulse application to time when signal is acquired. Usually many repetitions of the RF pulses are applied to a given slice of tissue to analyse the signal changes. This time interval between the application of two RF pulses is termed TR or repetition time and it determines how fast a single brain image is acquired.

During neural activity, the deoxyhemoglobin content of a tissue voxel is determined by the combination of cerebral blood flow(CBF), cerebral metabolic rate of oxygen($CMRO_2$) and cerebral blood volume(CBV) collectively termed as the hemodynamic response. For approximately 1s of neural activity 10-12s of hemodynamic response is elicited with a small delay. CBF is increased due to the neurovascular coupling mechanism and $CMRO_2$ is increased due to the consumption of oxygen for neural activity and CBV is increased due to the increase in CBF. The ratio of the fractional change of CBF to the fractional change in $CMRO_2$ during activation and their mismatch is the physical basis for the BOLD signal. Increase in deoxyhemoglobin content decreases the BOLD signal. As the CBF increases more than $CMRO_2$ in most brain areas, the deoxyhemoglobin content in the tissue voxel decreases, increasing the resultant BOLD signal.

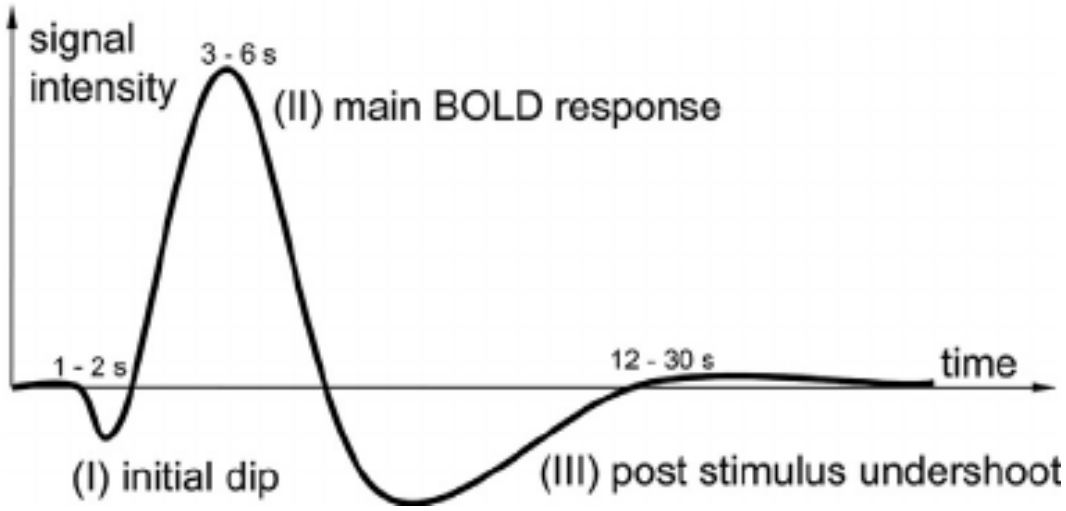

Fig. 1.3 A typical BOLD response. Figure reproduced from Siero et al [90]. The main BOLD response can be positive or negative depending on the interplay between CBF and $CMRO_2$. The shape of the response has a wide range. The initial dip and post stimulus undershoot are not always observed in some regions of the brain and the cause behind these responses are debated so far.

A typical BOLD signal as shown in Figure 1.3 has an initial dip followed by a positive or negative BOLD response and then a post stimulus undershoot. The shape of this response varies according to the interplay between CBF ,$CMRO_2$ and CBV [12]. Many studies have tried to find the correlation between BOLD response and neural activity. Even though the BOLD response correlated better with synaptic activity, there was some correlation between spiking and BOLD response as well [6]. On the contrary there are studies which found that none of these aspects of neural activity correlated with the BOLD response [25]. This

confusion can only be solved by establishing the exact relationship between neural activity and the BOLD response.

1.5 Research Aims

Disordered neurovascular coupling has been observed in several brain pathologies such as hypertension, stroke and Alzheimer's disease [50]. It is likely that the disruption of the interactions between neurons and the cerebral vasculature contributes to the initiation and progression of brain dysfunction. Hence understanding this coupling mechanism is of vital importance. The neurovascular coupling mechanism is still unclear primarily due to the complex interactions between many parameters and the difficulty in accessing, monitoring and measuring them in the highly heterogeneous brain. Hence a solid theoretical framework based on existing experimental knowledge is necessary to study the relation between neural activity, the associated vasoactive factors released and their effects on the vasculature. Such a framework should also be related to widely available experimental data such as fMRI so that it can be validated against repetitive experiments and generate verifiable hypothesis. The neural basis of fMRI has also been debated for long time and it was always just correlated with underlying neural activity. A quantitative understanding of fMRI simply cannot arise without understanding the neurovascular coupling mechanism and its associated metabolism. This study is a step towards constructing a model to simulate the fMRI BOLD signal with a certain hypothesis of neurovascular coupling underlying the simulated BOLD signal, see Figure 1.4.
The objectives of the study are

- To model the K^+ signalling hypothesis of neurovascular coupling mechanism and its associated neurometabolic response based on three different models available in the literature
- To use the neurovascular and neurometabolic responses to simulate the fMRI BOLD response based on a model available in the literature
- To simulate the BOLD response under different physiological scenarios such as continuous spiking, bursting, cortical spreading depresssion and hypoxia and examine under what conditions the simulated responses match the experimental observations

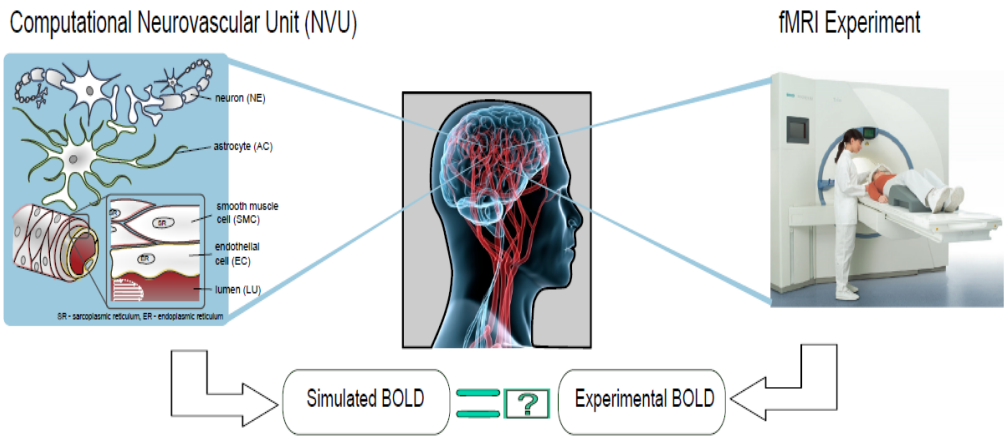

Fig. 1.4 Proposed method to test a hypothesis of neurovascular coupling. Simulated fMRI BOLD signal with a hypothesis of neurovascular coupling compared with the experimentally observed fMRI BOLD signal. Image of fMRI experiment was reproduced from an article by Susanne [9].

1.6 Thesis structure

Chapter 1 gives an introduction to the regulation of blood flow in the human body and neurovascular coupling mechanism in the brain. It gives a gist of various underlying hypotheses behind the neurovascular coupling mechanism and explains the fMRI technique which depends on this mechanism. It goes on to explain how modelling the mechanism along with the fMRI BOLD signal may contribute to the understanding of both. Based on those explanations specific objectives of the thesis towards that direction is given.
Chapter 2 describes and reviews the relevant literature to the study. The experimental studies of neurovascular coupling and fMRI BOLD are discussed along with the mathematical modelling attempts to simulate them.
Chapter 3 describes the basic components used to simulate the neurovascular coupling mechanism. Previously published models of neuron and vascular response through astrocyte signalling are replicated and the reason why they should be coupled is discussed.
Chapter 4 describes the coupling between the models discussed in previous chapter and the results for some parameter changes is presented and discussed.
Chapter 5 describes the model of fMRI BOLD signal and also describes CBF and $CMRO_2$ responses obtained from the neurovascular coupling model. The results of simulated fMRI BOLD signal from CBF and $CMRO_2$ responses is presented and discussed.
Chapter 6 gives the sensitivity of model outputs to certain parameters. It also examines if the presented model is able to simulate experimental results and discusses the results.
Chapter 7 gives a conclusion to the model presented and the results simulated. It also dis-

cusses the limitations of the model and the next step towards simulating the physiological mechanism and the experimental technique.

Chapter 2

Neurovascular coupling and the fMRI BOLD signal : A Review

In this chapter the relevant studies of neurovascualar coupling, oxygen metabolism and fMRI BOLD signal are highlighted. At first experimental studies and reviews that suggest different hypotheses of neurovascular coupling are described. The K^+ signalling hypothesis of neurovascular coupling is chosen due to its strong experimental support. Next the fMRI studies that tried to correlate BOLD with underlying neural activity is described to show how underlying neural activity is correlated with BOLD signal. Energy consumption of different kinds of neural activities are described. Then the different models of cellular structures involved in neurovascular coupling and models of fMRI BOLD signal are described.

2.0.1 Experimental studies of neurovascular coupling

Thomas et al [67] reviewed how the ion channels communicate with each other to control cerebral blood flow. The primary focus was to explore the role of ion channels in dynamically modulating the parenchymal arteriole smooth muscle cell membrane potential, thereby controlling the arteriolar diameter. They also remarked that the similarities in ion channel expression in the astrocytic endfeet and smooth muscle cell can help control the smooth muscle cell membrane potential precisely. The interaction of the channels such as BK (Big potassium), IK (Transient potassium), IP_3R (Inositol trisphosphate), and TRP4 (Transient receptor potential cation) present in the astrocytic endfeet and the channels such as SK (Ca^{2+}-activated potassium channels), IK, IP_3R, and TRP4 present in the endothelium are found to be active during neurovascular coupling. They have also been found to contribute to a process which leads to the release of vasoactive substances. In addition to emphasizing

the role of astrocyte and endothelium in controlling the blood flow the authors highlighted the possible role of capillary pericytes in fine tuning the vascular tone as they are present in over 90% capillaries and retinal pericytes are known to posses voltage dependent calcium channels (VDCCs).

Enager et al [26], for the first time, assessed the differences in neuronal responses and

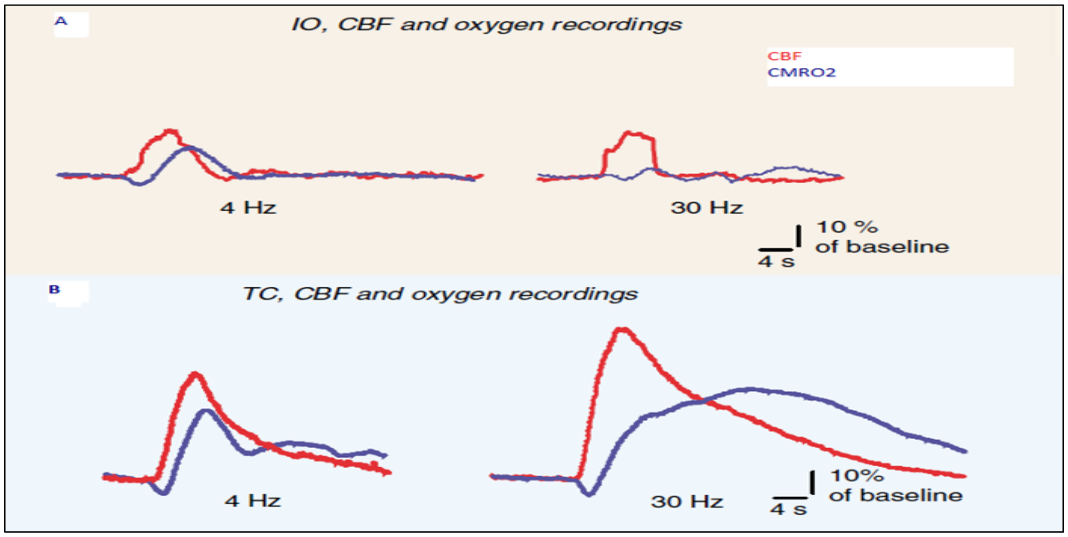

Fig. 2.1 Figure illustrating pathway specific variations in the neurovascular coupling and metabolic responses reproduced from Enager et al [26].A) CBF and tissue oxygen recordings in the somatosensory cotex shown for 4Hz (left) and 30Hz (right) after the infraorbitral(IO) nerve was stimulated. B) CBF and tissue oxygen recordings in the somatosensory cotex shown for 4Hz (left) and 30Hz (right) after the transcollosal afferents (TC) was stimulated.

changes in CBF and $CMRO_2$ in specific cortical areas that are evoked by two distinct neuronal networks. The enzymes capable of producing or releasing vasoactive factors and the neuronal cell types were identified with double immunocytochemistry. When the infraorbitral(IO) nerve was stimulated, it excited thalamocortical neurons in layer 1 of the barrel cortex followed by an activation in layers 2 and 3. When the transcollosal afferents (TC) was stimulated, it excited the septa located neurons on the contralateral side in layers 3 and 4 followed by an activation in layer 2. They reported that for the same level of glutamatergic synaptic activity, the increases in CBF and $CMRO_2$ were greater when evoked by corticocortical afferents than by thalamocorotical afferents shown in Figure 2.1. They also reported that at low and high stimulation frequencies interneurons with different contents of vasodilators were activated. These findings suggest that the responses of CBF and $CMRO_2$ reflect distinct properties of activated neurons in addition to the evoked synaptic activity.

Based on experimental evidence, Filosa et al [29] proposed a pathway for neurovascular coupling in the mammalian brain. Significant amount of evidence suggest that astrocytes

which make up half of the brain volume have important functions including mediating communication between the neurons and micro vessels. With their endfeet projected to both neuronal synapses and blood vessels, astrocytes are uniquely positioned to enable this fast communication. There are high densities of K^+ channels present in astrocytic endfeet near the synapses and blood vessels. Based on these facts Filosa et al proposed that the activation of BK channels in the endfeet near to blood vessels due to depolarization can lead to K+ efflux into the perivascular space. This efflux can hyperpolarize the KIR (Inwardly rectifying potassium) channels present in the vascular smooth muscle cells which can result in dilation. While strongly supporting rapid vessel response through K^+ signaling mechanism with evidence they also added that the evidence also suggested that the vasoactive factors like arachidonic acid(AA) metabolites can help to maintain the vessel response during sustained neuronal activation.

2.0.2 Experimental studies correlating the neural origin to fMRI BOLD signal

Lauritzen and Gold [62] studied the relationship between brain function and the neurophysiological correlates of signals used in functional neuroimaging. They used the rat cerebellar cortex for the study as the basic functional design of their intrinsic neuronal networks is relatively simple compared to other parts of the central nervous system. The purkinjee cells were activated by appropriate stimulus and the frequency dependency of the CBF response and spike rate was studied. They found that the CBF response neither correlated with spontaneous spikes nor with the complex spikes consistently. It implies that the BOLD signal could not be an indicator of the underlying spike activity. They also studied the relationship of synaptic activity with BOLD by monitoring the local field potential(LFP) which is an indicator of synaptic function. They summed up the LFP amplitude for the entire stimulation period and compared it with the associated CBF response. They found the there was a linear relationship between both and hence the BOLD response could be an indicator of the underlying pre-synaptic and post-synaptic activities. They also suggested that the mechanisms that transform neural activity to blood flow response was slow as they observed that the vascular response took several seconds to develop in contrast to the LFP which increased in a few milliseconds.

Ekstrom [25], in his review challenged the view of a particular aspect of neural activity being correlated to the BOLD response. He produced several examples to suggest that spiking, local field potential and BOLD response can be dissociated. Some studies have

also suggested that their relationship is both behaviour and region dependent. Primarily two possible explanations were given by him for such a case. A circuitry based explanation fits a region which receives input from multiple regions of the brain and provides spiking responses or synaptic response for different inputs. This was also strongly suggested by the work of Enager et al [26] who studied the pathway specific neurovascular response. Another explanation could arise from the vasculature wherein a certain region of the brain has much higher capillary density compared to another region. This could mean that the region with low capillary density may have higher metabolism than cerebral blood flow . The consequence of which is a negative BOLD signal.

2.0.3 Energy consumption in the brain

Chih and Roberts [20] critically reviewed the energy substrates for neurons during neural activity. The conventional hypothesis is that glucose usage in neurons and astrocytes increases during neural activity. Glucose is metabolized by glycolysis (anaerobic) to pyruvate and produces 2 Adenosine triphosphate (ATP) molecules. Pyruvate either enters the tricarboxylic acid(TCA) cycle or is converted to lactate by lactate dehydrogenase. Even though the percentage of consumption of glucose through aerobic and anaerobic pathways is variable, it is approximately 90% and 10% respectively [80]. Another hypothesis that has gained significant attention recently is the astrocyte neuron lactate shuttle(ANLSH) hypothesis. According to this the glucose is entirely metabolized in the astrocytes to lactate which is then taken up and used by the neuron during neural activity. By comparing glucose and lactate as energy substrates for neurons during neural activity Chih and Roberts suggest that lactate can't be an efficient energy substrate for various reasons and glucose is the primary energy substrate in both neurons and astrocytes adhering to the conventional hypothesis. Factors like the slow increase in lactate levels during neural activity, rapid increase in glycolysis following activation and the likelihood that this activation might suppress lacate oxidation stand against the ANLSH hypothesis.

Ames et al [2]reviewed the energy metabolism related to function in the central nervous system. He suggests that the inability to completely understand the energy metabolism is due to the difficulty in monitoring and measuring the rapid changes in metabolic demands in the highly heterogeneous brain. The processes that require energy and the speculative estimates of their relative demands were given based on different experimental data. As per the estimate, the vegetative processes that maintain the homeostasis including protein synthesis accounted for 10-15% of the total energy consumption. The costliest of the functions is restoring the ionic gradients during neural activation. The Na^+/K^+ exchange pump is

estimated to consume 40-50%, while the Ca^{2+} influx from organelles and extracellular fluid consumes 3-7%. The processing of neurotransmitters such as uptake or synthesis consumes 10-20%, while the intracellular signaling systems which includes activation and inactivation of proteins consumes 20-30%. The rest of the energy 20-30% is estimated to be consumed by the axonal and dendritic transport in both directions. He also suggests that the mechanisms that reduce the neural activity when the energy levels are low could have evolved to ensure that the energy levels remain within safe limits.

Attwell and Laughlin [7] reviewed the energy budget for signaling in grey matter of the

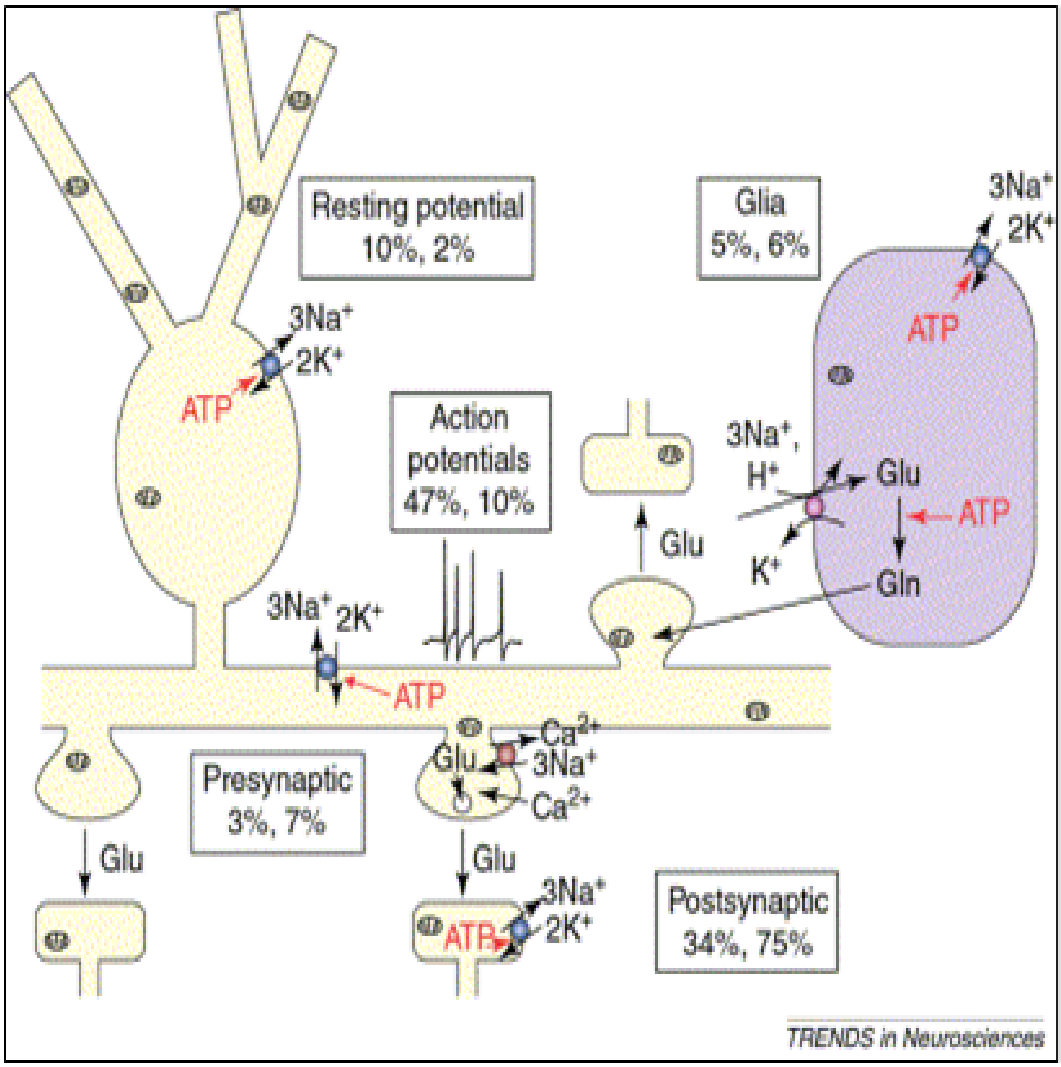

Fig. 2.2 Figure showing energy estimates of different subcellular processes for neurons (yellow) and glia (mauve) during grey matter signalling, reproduced from Attwell and Laughlin [7]. Estimates are given for rodents (first value) and primates (second value) assuming that primates have ten fold increase in synaptic density per neuron compared to rodents.

rodent brain. They used that data to calculate the energy cost of mammalian grey matter, specifying the metabolic cost of mechanisms that generate and transmit neural signals. Based on the evidence that excitatory neurons out number inhibitory neurons by a factor of 9 to 1, and 90% synapses release glutamate, all cells were assumed as glutamergic for simplification. They analyzed the transmitter release triggered by a single neuron to estimate the energy needs of various components of signaling in the brain. This information was then used to estimate the energy used by different cellular processes and the relation between energy usage and action potential frequency. For a mean firing rate of 4 Hz, the estimated energy cost for generating action potential was 47%, maintaining resting potential was 13%, glutamate recycling was 3%, driving pre-synaptic Ca^{2+} entry was 3%, and reversing ion fluxes by post synaptic receptors was 34%. The values for the rodent brain was adjusted according to the data from the human brain to estimate the energy cost of the human brain as shown in Figure 2.2. Important differences in the human brain such as increases in energy usage for action potential with increasing axon and dendritic length, 3-10 fold lower density of neurons in the human brain were considered in the estimation.

2.0.4 Models of cellular structures involved in neurovascular coupling

Farr and David [27] developed a mathematical model that describes potassium and EET signaling pathways of neurovascular coupling as per the suggestions of the experimental work of Filosa and Blanco [29]. The mechanism described in the model starts with the release of potassium and glutamate from the neuron during neural activity which is taken up by the Na^+/K^+ exchange pump and glutamate receptors in the astrocyte respectively. The astrocyte model was based on the model of Bennett et al [8]. While the influx of potassium depolarizes the astrocyte, the glutamate activates release of IP_3(Inositol triphosphate) from the cytosol which increases intracellular calcium concentration. The AA(arachiodonic acid) derived EETs (epoxyeicosatrienoic acid) which are produced due to increases in cytosolic calcium concentration and the calcium concentration itself gate the BK channel in the astrocyte. The model of smooth muscle cell and endothelial cell is based on the model of Koenigsberger et al [58] with an addition of a KIR channel. The efflux of K^+ into the perivascular space activates the KIR channel and hyperpolarizes the smooth muscle cell closing the voltage operated calcium channels which decreases the calcium concentration in the smooth muscle cell. The decrease in Ca^{2+} concentration leads to dilation of the arteriole. Neuronal activation of about 60s caused 15% arteriolar dilation in the model. Even though the model provided qualitative description of neurovascular coupling there was a large delay in vessel dilation following neural activation.

Based on the work of Farr and David, Dormanns et al [24] developed a mathematical model to study the K^+ signaling pathway of neurovascular coupling. They replaced the astrocyte model of Farr and David with a model by Ostby et al [77] which included a phenomenological change of extracellular ions due to neural activity. They also extended it by adding a BK channel to the astrocyte which can enable communication to the smooth muscle cell through the KIR channel to induce dilation or constriction. The kinetics of the BK channel is purely driven by membrane potential of the astrocyte unlike the model of Farr and David wherein it was dependent on the calcium concentration as well. Hence K^+ influx during neural activity directly gates the BK channel by depolarizing the astrocyte. They also investigated the influence of Ca^{2+} and agonist concentration in neurovascular coupling. Based on model results, they suggested that Ca^{2+} may be necessary but may not be the only pathway for neurovascular coupling. For higher values of the rate of IP_3 production, oscillation is induced in the model by calcium induced calcium release(CICR) mechanism which inhibits neurovascular coupling.
Chang et al [16] developed a mathematical model to study the effects of metabolic and perfusion on cortical spreading depression(CSD) which is a slow moving ionic and metabolic disturbance in the cortical brain tissue. They used the neuron model based on Kager et al [56] and induced CSD in it to study the effects of hypoxia. The vascular response was based on the neurovascular model of Farr and David [27]. In addition to this the variations of vascular response on factors like species, individual and metabolic states were also considered. The key features of the model are that the Na^+/K^+ exchange pump in the neuron was dependent on the tissue oxygen concentration which depends on the vascular supply and oxygen consumption. They found that during CSD the metabolic demands exceeds the physiologic limits placed on oxygen delivery and it induces vasoconstriction which further reduces oxygenation in the tissue. The model predicted faster and longer duration of CSD waves due to the contribution of the vasculature and oxygen consumption.

2.0.5 Models of fMRI BOLD signal

The dynamic changes of deoxyhemoglobin content and their corresponding changes in blood volume and fMRI BOLD signals during neural activation was described by Buxton et al [13]. In addition to that they tested the model against finger-tapping task experimental BOLD data and have found good agreement. The model assumes that the blood flow during neural activation is negligible compared to the blood volume. This blood volume is then modelled as an expandable venous balloon which receives blood from the capillary bed. With this model they simulated the different transients observed in the BOLD signal such as initial

dip, overshoots and post stimulus undershoot. Though the model was simple, it represented how blood oxygenation changes due to blood flow along with the blood volume changes can explain the BOLD signal transients.
Buxton et al [12] integrated different models and developed a mathematical framework to determine the hemodynamic response to brain activation. The fMRI BOLD response was determined from oxygen extraction fraction and cerebral blood volume. The balloon model [13] was used to describe the transients of cerebral blood volume and deoxyhemoglobin. The CBF and $CMRO_2$ which determine the oxygen extraction fraction were modelled as linear convolutions of the neural activity. The model was able to determine the experimentally observed variations in the BOLD signal such as initial dip and post stimulus undershoot. By having a delay in the CBF response to that of $CMRO_2$ response, the initial dip was simulated and the transients of the cerebral blood volume contributed to the post stimulus undershoot. Even though the model did not have much quantitative account for the mechanisms causing the variations of CBF and $CMRO_2$ response, it did provide a reliable framework for simulating the fMRI BOLD response with the temporal profiles of CBF and $CMRO_2$.
There have been a number of papers published which are specific to energy consumption in the brain or neurovascular coupling or BOLD response but none to our knowledge which integrated the neurometabolic and neurovasular effects leading to a BOLD response. This work was hence focussed towards simulating the fMRI BOLD response with a certain hypothesis of neurovascular coupling. In particular the experimental evidences and suggestions of Enager et al [26] and Ekstrom [25] threw light on the importance of examining the neurovascular response and neurometabolic response with respect to the neural activity that evoked it.

2.0.6 summary

Many mechanisms such as the K^+ signalling mechanism, the nitric oxide signalling mechanism or the archidonic acid to EET pathway are found to contribute to the neurovascular respose so far [5]. The K^+ signalling mechanism of neurovascular coupling is supported by many strong evidences. This hypothesis mainly utilizes the astrocyte which is perfectly positioned to enable the communication between the neurons and the blood vessels. The astrocyte and the endothelial cells exhibit a striking similarity in the ion channel expression and this can enable it to control the smooth muscle cell from both the neuronal and the side of the blood vessel [67]. Whenever there is neuronal activation potassium ions are released into the extracellular space. The astrocyte gets depolarized by taking up potassium released by the neuron and releases it in the endfeet near the arterioles through the BK channels [28]. This increase in extracellular space potassium concentration (3-10mM) near

the arteriole hyperpolarizes the smooth muscle cell through the KIR channel and causes dilation. Amidst the difficulty in monitoring and measuring the rapid changes in metabolic demands in the highly heterogeneous brain, the speculative estimates of the relative demands of the processes that require energy were given based on different experimental data by Ames et al [2]. As per the estimate, the Na^+/K^+ exchange pump is estimated to consume 40-50%. The K^+ signalling mechanism of neurovascular coupling along with an estimate of energy consumption during the process will enable to model the oxygenation changes in the tissue. By combining the models of Chang et al[16], Kager et al[55], Dormanns et al [24] and Buxton et al [12] an integrative model of neural activity, its associated neurovascular coupling signalling mechanism, its associated metabolism and consequently its fMRI BOLD signal changes can be simulated. This study will be a step towards constructing detailed models based on experimental data to simulate the fMRI BOLD signal with a certain hypothesis of neurovascular coupling, it's associated metabolic and blood volume responses.

Chapter 3

Models of the different components of Neurovascular coupling

3.1 Introduction

In this chapter, the basic units of neurovascular coupling model comprising the neuron, astrocyte, smooth muscle cell and the endothelial cell that are used to describe the K^+ signalling mechanism are explained. Model of each cell type is based on different existing models and hence replicating some of those previously published results will help to justify why coupling them will render them to model neurovascular coupling. A lumped parameter approach was used where only time derivatives are considered and spatial derivatives are neglected. Inter compartmental communication was enabled using ion channels, Na^+/K^+ -ATPase pump, and leak channels. In each domain the model variables were described by a set of ODEs based on the conservation of mass and Kirchoff's law and solved using MATLAB routine ode15s with a relative tolerance of $1e^{-3}$, absolute tolerance of $1e^{-6}$ and maximum step of 1.

3.2 The neuron(NE) model

The neuron model is based on the work of Chang et al [16] and Kager et al[55] who studied cortical spreading depression. The combination of both their model is used to describe neural activation, restoration of ionic gradients and consumption of Na^+/K^+ -ATPase pump. The neuron model based on hippocampal pyramidal cells was first presented by Kager et al for studying seizures and cortical spreading depression. It was also the first cortical neuron model with time dependent ionic concentrations and it helped them study the influence of

high extracellular potassium on the neural activity. The three major ions sodium, potassium and chlorine and their associated ion channels which contribute to the neural activation are considered in their model. There are three compartments namely soma, dendrite and extracellular space (ECS). A representation of the neuron model along with the ion channels and pumps is shown in Figure 3.1.

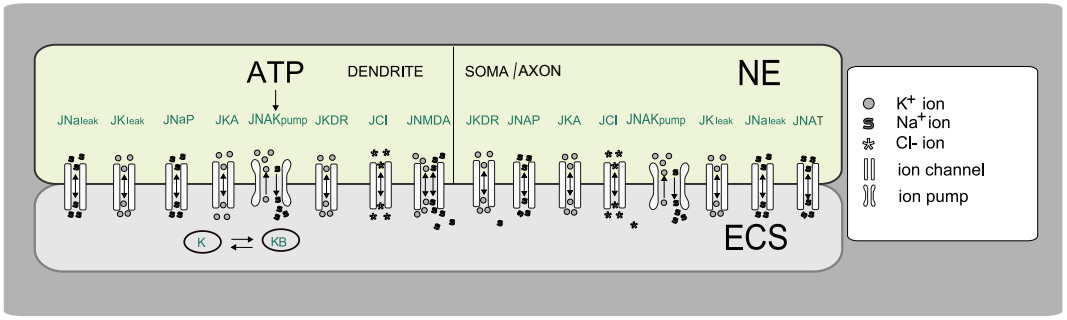

Fig. 3.1 Neuron model based on Chang et al [16] and Kager et al[55].The ion channels for sodium are transient sodium (NaT), persistent sodium (NaP) and sodium leak channels (Naleak) and the ion channels for potassium are delayed rectifier potassium channel (KDR), transient potassium channel (KA) and potassium leak channel (Kleak). N-methyl-D-aspartate (NMDA) receptor mediated channel allows both sodium and potassium. The NAKpump(Sodium potassium exchange pump) moves out three intracellular sodium ions and two extracellular potassium ions against their electrochemical gradients.

3.2.1 Ion channels, cross membrane currents and the Na^+/K^+ exchange pump

The soma compartment has three sodium ion channels namely the transient sodium (NaT), persistent sodium (NaP) and sodium leak channels (Naleak) and three potassium channels namely delayed rectifier potassium channel (KDR), transient potassium channel (KA) and potassium leak channel (Kleak). In addition to these the dendrite compartment also has an N-methyl-D-aspartate (NMDA) receptor mediated channel which can allow both the sodium and potassium currents to flow through it. The cross-membrane currents of all the ion channels except the leak ion channel were modelled using the Goldman-Hodgkin-Katz (GHK) equation given as

$$I_{Ion,GHK} = m^p h^q \frac{g_{Ion,GHK} F v_m [[Ion]_i - exp(\frac{-v_m}{\phi})[Ion]_e]}{\phi[1 - exp(\frac{-v_m}{\phi})]} \tag{3.1}$$

where $I_{Ion,GHK}$ (mA/cm^2) is the current of a particular ion through an ion channel, $g_{Ion,GHK}$ $(cm/s^-1)$is the maximal conductance value and permeability is absorbed into this parameter, v_m (mV) is the membrane potential, $\phi = PT/F$ where P is the universal gas constant , T the absolute temperature and F Faraday's constant, $[Ion]_i$ (mM) and $[Ion]_e$ (mM) are the concentrations of a particular ion inside and outside the membrane respectively. The conductance is channel specific and concentration of ion is compartment specific. The electrically excitable property of the neuron is simulated using the classical Hodgkin Huxley kinetic description [45]. The variables m and h are the fraction of activation and inactivation gates in the open state respectively. The parameters p and q are the number of individual activation and inactivation gates per channel respectively. The rate at which the activation gates open and close in response to the membrane potential is modelled according to the equation

$$\frac{\mathrm{d}m}{\mathrm{d}t} = \frac{m_\infty(v_m) - m}{\tau_m(v_m)} \tag{3.2}$$

where

$$m_\infty(v_m) = \frac{\alpha_m(v_m)}{\alpha_m(v_m) + \beta_m(v_m)} \tag{3.3}$$

and

$$\tau_m(v_m) = \frac{1}{\alpha_m(v_m) + \beta_m(v_m)} \tag{3.4}$$

The function $m_\infty(v_m)$ is called the steady-state activation curve. The value of m tend asymptotically to the steady state if voltage is held constant for a sufficient length of time. The function τ_m is the characteristic time scale of the activation gate describing the variation of the characteristic time scale with of the membrane potential. These equations state that the closed activation gates, $(1-m)$, open at rate $\alpha_m(v_m)$, while the open activation gates, m, close at a rate $\beta_m(v_m)$. The rate functions, $\alpha_m(v_m)$ and $\beta_m(v_m)$, are functions that depend on the voltage across the membrane. Similarly the rate at which the inactivation gates close in response to membrane potential is modelled. Thus the varying response of different channels to membrane potential is modelled with the experimental data containing maximal conductance and rate functions of the activation and inactivation gates of the individual channels. The rate functions α and β are usually determined through a mix of theoretical and empirical considerations. These exponential forms are modified to fit the experimental data using curve fitting. The expressions used in the neuron model that describe the voltage-dependent rate functions are based on a model of hippocamppal pyramidal cells [96] and morphological parameters are based on reconstructed hippocampal neurons [15]. The sodium, potassium

and chlorine leak currents are calculated by the Hodgkin-Huxley(HH) model given by

$$I_{Ion,HH} = g_{Ion,HH}(v_m - E_{Ion}) \tag{3.5}$$

where $g_{Ion,HH}$ is the constant conductance for the specific ion and E_{Ion} is the Nernst potential for the specific ion and is given by

$$E_{Ion} = \frac{PT}{zF} log \frac{[Ion]_e}{[Ion]_i} \tag{3.6}$$

here z is the valence of the ionic species and the subscripts e and i correspond to the extracellular space and intracellular space respectively. The primary role of Na^+/K^+ ATPase exchange pump in the neuronal membrane is to restore ionic concentrations to their homoeostatic state during neural activation. The Na^+/K^+ ATPase pump is a transmembrane protein with two extracellular binding sites for potassium, three intracellular binding sites for sodium, and a single intracellular binding site for ATP. The pump moves out three intracellular sodium ions and two extracellular potassium ions against their electrochemical gradients and hence the need for energy. Both the soma and dendrite compartments have a Na^+/K^+ exchange pump. Since the energy in the form of ATP is highly dependent on tissue oxygen concentration, the exchange pump current in the neuronal membrane is modelled as a variable dependent on the availability of oxygen. The potassium and sodium pump currents in the soma and dendrite are given by $I_{*,K,pump} = -2I_{*,pump}$ and $I_{*,Na,pump} = 3I_{*,pump}$ respectively($*$ is either s for somatic or d for dendritic). The total current due to the sodium/potassium exchange pump in the soma and dendrite is given by

$$I_{*,pump} = I_{max}\gamma_{*,pump,1}([K^+]_e, [Na^+]_i, *)\gamma_{*,pump,2}([O_2]) \tag{3.7}$$

where I_{max} is the maximum pumping rate of the Na^+/K^+ exchange pump with

$$\gamma_{*,pump,1}([K^+]_e, [Na^+]_i, *) = \left(1 + \frac{[K^+]_{e,0}}{[K^+]_e}\right)^{-2} \left(1 + \frac{[Na^+]_{i,0}}{[Na^+]_{i,*}}\right)^{-3} \tag{3.8}$$

where $[K^+]_{e,0}$ and $[Na^+]_{i,0}$ are the baseline concentrations of extracellular potassium and intracellular sodium respectively. This expression describes that the action of the pump depends on the concentrations of extracellular potassium and intracellular sodium. The second pump represents the oxygen dependent production of ATP by the mitochondria[21, 44]

taking the form

$$\gamma_{*,pump,2}([O_2]) = 2\left(1+\frac{[O_2]_0}{(1-G)[O_2]+G[O_2]_0}\right)^{-1} \tag{3.9}$$

in this case $[O_2]$ is the tissue oxygen concentration encompassing the neurovascular unit, $[O_2]_0$ is the equilibrium value of oxygen concentration and G is the percentage of ATP production that is independent of oxygen. This expression indicates that the pumping rate will be reduced whenever there is a decrease in the oxygen level in the tissue.

Table 3.1 Rate expressions and parameter values used in the voltage dependent channel currents of the neuron model, from Chang et al[16]

Currents mA/cm^2	$g_{Ion,GHK}$ cm/s^-1	**Gates** $m^p h^q$	**Voltage dependent rate functions** ms^-1
$I_{Na,P}$	2×10^{-6}	m^2h	$\alpha_m = \frac{1}{6(1+exp[-(0.143v_m+5.67)])}$ $\beta_m = \frac{exp[-(0.143v_m+5.67)]}{6(1+exp[-(0.143v_m+5.67)])}$ $\alpha_h = 5.12\times10^{-8}exp[-(0.056v_m+2.94)]$ $\beta_h = \frac{1.6\times10^{-6}}{1+exp[-(0.2v_m+1.25)]}$
$I_{K,DR}$	10×10^{-5}	m^2	$\alpha_m = 0.016\frac{v_m+34.9}{1-exp[-(0.2E_m+6.98)]}$ $\beta_m = 0.25exp[-(0.25v_m+1.25)]$
$I_{K,A}$	1×10^{-5}	m^2h	$\alpha_m = 0.02\frac{v_m+56.9}{1-exp[-(0.1v_m+5.69)]}$ $\beta_m = 0.0175\frac{v_m+29.9}{exp(0.1v_m+2.99)-1}$ $\alpha_h = 0.016exp[-(0.056v_m+4.61)]$ $\beta_h = \frac{0.5}{1+exp[-(0.2v_m+11.98)]}$
I_{NMDA}	1×10^{-5}	mh	$\alpha_m = \frac{0.5}{1+exp\left(\frac{13.5-[K^+]}{1.42}\right)}$ $\beta_m = 0.5-\alpha_m$ $\alpha_h = \frac{1}{2000\left(1+exp\left[\frac{[K^+]e-6.75}{0.71}\right]\right)}$ $\beta_h = 5\times10^{-5}-\alpha_h$
I_{NaT}	10×10^{-5}	m^3h	$\alpha_m = 0.32\frac{-v_m-51.9}{(exp[-(0.25v_m+12.975)]-1)}$ $\beta_m = 0.28\frac{v_m+24.89}{(exp[-(0.2v_m+4.978)]-1)}$ $\alpha_h = 0.128exp[-(0.056v_m+2.94)]$ $\beta_h = \frac{4}{1+exp[-(0.2v_m+6)]}$

3.2.2 Membrane potential and Ionic concentration

In reality the membrane potential depends on the membrane potential difference and concentration gradients. Here, the membrane potential of the soma and dendrite is calculated based on the assumption that the flow of ions between the two compartments is only due

to the difference in membrane potential between them. The total cross membrane currents are the sum of the voltage dependent sodium and potassium currents, sodium, potassium and chlorine leak currents, and the sodium-potassium exchange current. The membrane potentials of the neuronal compartments are governed by the differential equations of the form

$$C_m \frac{\mathrm{d}v_{m,s}}{\mathrm{d}t} = -I_{s,tot} + \frac{1}{2R_a\delta_d^2}(v_{m,d} - v_{m,s}) + I_{stim} \tag{3.10}$$

$$C_m \frac{\mathrm{d}v_{m,d}}{\mathrm{d}t} = -I_{d,tot} + \frac{1}{2R_a\delta_d^2}(v_{m,s} - v_{m,d}) \tag{3.11}$$

here C_m is the membrane capacitance per unit surface area, R_a is the input resistance of the effective dendritic tree, δ_d is the half length of the effective dendritic tree,$v_{m,s}$ and $v_{m,d}$ are the membrane potentials of soma and dendrite respectively. I_{stim} is the stimulating current defined as a function of time. $I_{s,tot}$ and $I_{s,tot}$ are the total cross-membrane ionic currents per unit surface area for soma and dendrite written as

$$I_{*,tot} = I_{*,Na,tot} + I_{*,K,tot} + I_{*,Cl,tot} \tag{3.12}$$

The rates of change of ionic concentration in the soma and dendrite are due to the membrane currents and the exchange between the soma and dendrite. The exchange between the somatic and dendritic compartments is modelled by a flux proportional to the difference between their ion concentrations. Here, the ionic concentration of the soma and dendrite is calculated based on the assumption that the flow of ions between the two compartments is only due to the difference in ionic concentration between them. The equation describing the rate of change of ions in the soma is again of the general form

$$\frac{\mathrm{d}[Ion]_{i,s}}{\mathrm{d}t} = -\frac{A_s}{FV_s} I_{s,Ion,tot} + \frac{D_{Ion}(V_d + V_s)}{2\delta_d^2 V_s}([Ion]_{i,d} - [Ion]_{i,s}) \tag{3.13}$$

The notation, D_{Ion} , is the ion diffusion coefficient in aqueous solution taking into account tortuosity and volume fraction [75]. The quantities A_s and A_d are the surface areas of the soma and dendrite respectively in the total fixed volume given by the sum of the fixed somatic volume V_s, dendritic volumeV_d, and extracellular volume,V_e. The equation describing the rate of change of ions in the dendrite is

$$\frac{\mathrm{d}[Ion]_{i,d}}{\mathrm{d}t} = -\frac{A_d}{FV_d} I_{d,Ion,tot} + \frac{D_{Ion}(V_s + V_d)}{2\delta_d^2 V_d}([Ion]_{i,s} - [Ion]_{i,d}) \tag{3.14}$$

The local rates of change of the extracellular space ions are due to the membrane currents from the soma and dendrite. To ensure electro-neutrality, the initial extracellular concentration of the anion Cl^- is chosen to be equal to the sum of the concentration of cations Na^+ and K^+ in the extracellular space. Also, the initial intracellular concentration of chlorine is chosen in such a way that its Nernst potential matches a resting membrane potential of -70 mV. The existence of immobile anions has been assumed in the soma and dendrites to achieve intracellular electro-neutrality. The equations describing the rate of change of ions in the extracellular compartment is given by

$$\frac{\mathrm{d}[Ion]_e}{\mathrm{d}t} = \frac{1}{f_e F}\left(\frac{A_s I_{s,Ion,tot}}{V_s} + \frac{A_d I_{d,Ion,tot}}{V_d}\right) \tag{3.15}$$

where extracellular space volume fraction is given by $f_e = V_e/(V_s + V_d)$. The extracellular space volume was defined as 15% of the intracellular space volume based on published data [69, 70]. A phenomenological potassium buffering is represented by the following chemical reaction.

$$[K^+]_e + B \rightleftarrows_{Y_1}^{Y_2} [K^+]_b \tag{3.16}$$

The potassium buffer concentration is given by the differential equation

$$\frac{\mathrm{d}[K^+]_b}{\mathrm{d}t} = Y_2[K^+]_e(b_0 - [K^+]_b) - Y_1[K^+]_b \tag{3.17}$$

where b_0 is the initial buffer concentration, Y_1 is the constant backward buffering rate, Y_2 is the forward buffering rate given by a function of extracellular potassium written as

$$Y_2 = \frac{y_3}{1 + exp(-([K^+]_e - 5.5)/1.09)} \tag{3.18}$$

where the parameter y_3 and Y_1 are the buffering strength and they have the same numerical value. The difference between the neuron model based on Chang et al and the neuron model based on Kager et al has to be noted as we have used the combination of these models to simulate neural activity. Chang et al [16] only considered the channels that contribute to cortical spreading depolarization and hence did not include the transient sodium channel (NaT) which is the primary sodium channel in neurons. The effect of not including this channel on the neural membrane potential dynamics is quite dramatic. On the other hand, Kager et al [55] did not have lateral diffusion of ions between the two compartments and also did not have an oxygen dependent Na^+/K^+ exchange pump.

Table 3.2 Initial resting values and other parameter values of the neuron model and model of vasculature, from Chang et al[16] and Dormanns et al[24]

Parameters	Values	Units	Description
v_m	-70	mV	membrane potential
$[K^+]_e$	3.5	mM	extracellular space potassium ion concentration
$[K^+]_i$	133.5	mM	intracellular potassium ion concentration of neuron
$[Na^+]_e$	140	mM	extracellular space sodium ion concentration
$[Na^+]_i$	10	mM	intracellular sodium ion concentration of neuron
$[O_2]_0$	2×10^{-2}	mM	baseline concentration of oxygen in the tissue
$[O_2]_b$	4×10^{-2}	mM	blood oxygen concentration
$[K^+]_b$	135	mM	buffer concentration
b_0	500	mM	initial buffer concentration
Y_1	8×10^{-4}	s^-1	buffering strength
y_3	8×10^{-4}	$s^-1 mM^-1$	buffering strength
R_a	1.83×10^5	Ω	input resistance of dendritic tree
δ_d	4.5×10^{-4}	m	half-length of dendrite
A_s	1.586×10^{-9}	m^2	surface area of soma
A_d	2.6732×10^{-8}	m^2	surface area of dendrite
V_s	2.160×10^{-15}	m^3	volume of soma
V_d	5.614×10^{-15}	m^3	volume of dendrite
S_e	4.1179×10^{-8}	m	volume to surface area ratio of the extracellular space
C_m	7.5×10^{-5}	$s/\Omega cm^2$	membrane capacitance
I_{max}	0.013	mA/cm^2	Na^+/K^+-ATPase rate
D_{Na^+}	1.33×10^{-1}	m^2/s	Sodium diffusion coefficient
D_{K^+}	1.96×10^{-1}	m^2/s	Potassium diffusion coefficient
D_{Cl^-}	2.03×10^{-1}	m^2/s	Chlorine diffusion coefficient
$R_{0_{pas}}$	20×10^{-6}	m	radius of the artery without applied stress
H	0.6	$-$	scaling factor of initial radius
Y_{pas}	66×10^3	Pa	Young's moduli for the passive vessel
Y_{act}	167×10^3	Pa	Young's moduli when vessel is active
Δp	4×10^3	Pa	Transmural pressure
η	10^4	$Pa\ s$	viscosity

3.3 Results of the neuron model

The results of previously published models are replicated and the effects of variations to certain parameters in the model are presented in this section. The behaviours of the neuron model such as spiking, bursting, and cortical spreading depression characterized by steady

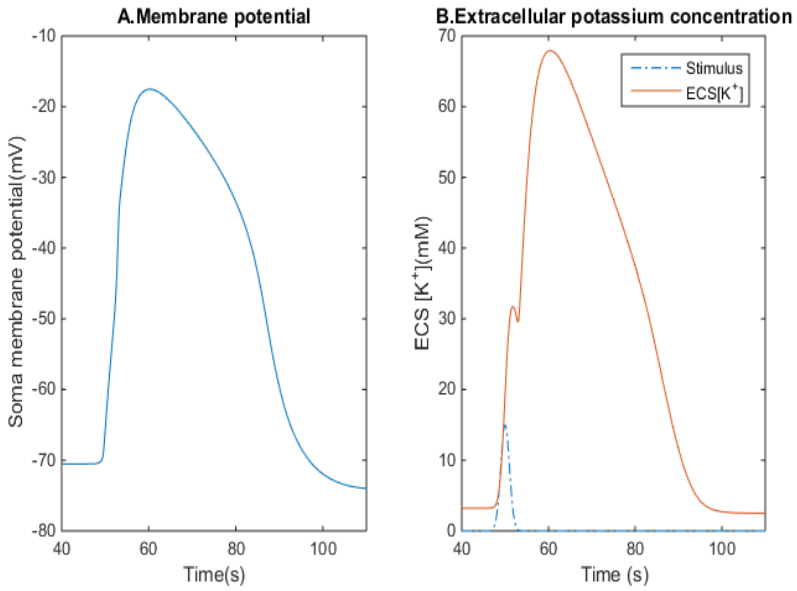

(a) Soma membrane potential (A) and Extracellular potassium concentration (B) during CSD simulated without the NaT channel

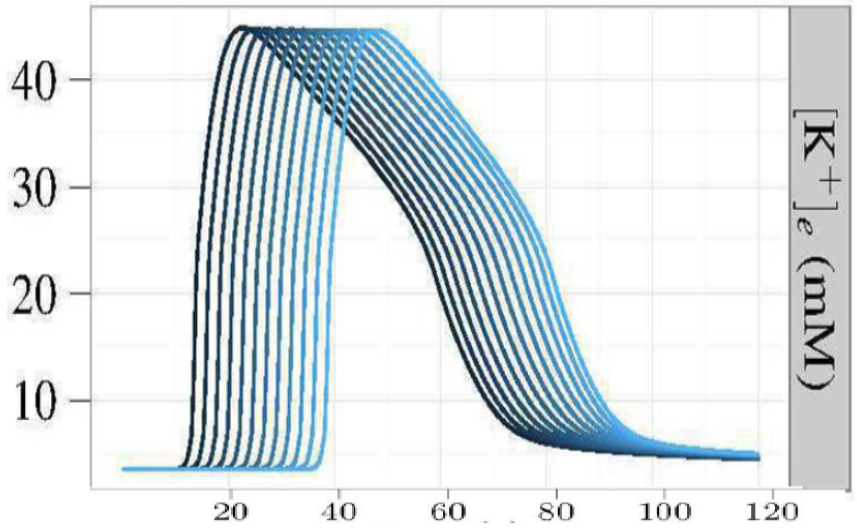

(b) Extracellular potassium concentration during CSD reproduced from chang et al [16]

Fig. 3.2 Comparison of ECS potassium concentration during CSD simulated without NaT channel with that of the result of Chang et al [16]. The neuron model is stimulated with a extracellular potassium input in Gaussian form with stimulus intensity of 15mM, mean=50 and variance=2s. A huge rise in extracellular potassium is seen(See a)B) due to the steady depolarization of the neuron(See a)A). A huge rise in extracellular potassium was also observed spatially by Chang et al as shown in b.

depolarisation are simulated and examined.

3.3.1 Cortical spreading neuron model without NaT channel

The neuron model behaviour is simulated without the oxygen dependent term in equation 3.7 as it is not coupled to the vasculature here. The Chang et al model did not include a NaT channel as they were only interested in stimulating cortical spreading depression. To compare the results, the neuron model is stimulated with a flux of extracellular potassium in Gaussian form with a stimulus intensity of 15 mM, mean=50 and variance=2s. Figure 3.2 shows the soma membrane potential and extracelluar potassium profiles obtained. The extracellular potassium concentration peaked to about 65mM due to steady depolarization of the membrane potential. This is characteristic of spreading depression as observed by Chang et al[16]. This efflux of potassium happens once the stimulus intensity is high enough to cross a threshold and open the voltage dependent ion channels.

3.3.2 Cortical spreading neuron model with NaT channel

The neuron model is then compared to the model of Kager et al who studied seizures and cortical spreading depression. Figure 3.3C,D shows the behaviour of the neuron model as observed by Kager et al for a depolarizing pulse of $20 mA/cm^2$ applied to cell soma for 500ms. Figure 3.3C shows firing at high rate which continues well beyond the stimulus duration. Once the firing stops it eventually enters into a steady depolarized state. Prolonged firing after stimulus was not observed in the simulated data but the firing for about 500ms and eventually entering a depolarised state for about 40 s was seen (Figure 3.3A,B) similar to Kager et al.

The sodium transient ion channel is included and the soma is then stimulated with a current in rectangular form with intensity 8×10^{-4}mA/cm^2 for 1s. The Figure 3.3 shows similar behaviour to that of Kager et al. Initially a few spikes are observed in membrane potentials and then enters the inactivated depolarized state. The difference between the two models is that the rate at which the potassium concentration increases is higher in the combined neuron model due to the oxygen dependency of the Na^+/K^+ ATPase pump.

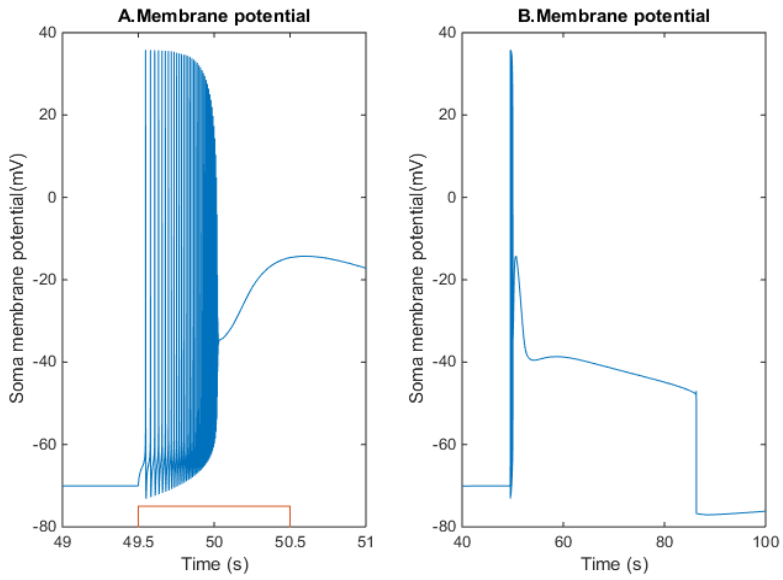

(a) A,B: Soma membrane potential during CSD simulated with NaT channel

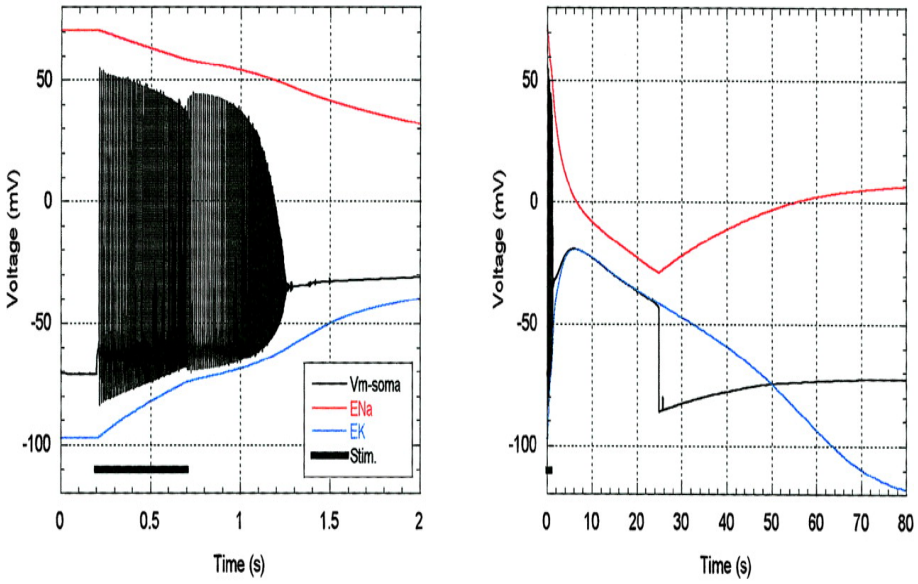

(b) C,D: Soma membrane potential during CSD reproduced from Kager et al [55]

Fig. 3.3 Comparison of soma membrane potential during CSD simulated with NaT channel with that of the result of Kager et al [55]. A stimulating current in rectangular form with 8×10^{-3}mA/cm^2 intensity and 1s duration was applied to the cell soma and the membrane potential is plotted in two different time scales(a) following Kager et al. Seizure discharges followed by cortical spreading depolarization reproduced from Kager et al [55]. A depolarizing pulse of $20mA/cm^2$ applied to cell soma for 500ms. Figures C and D has membrane potential and Nernst potentials of sodium and potassium.

3.3.3 Behaviour of neuron model for varying values of maximum pumping rate

A typical neuron fires an action potential when the combined post synaptic potential drives its membrane potential beyond a certain threshold. This firing will continue as long as the extracellular ionic changes are maintained in a physiological range. The neuron model is used here as a substitute for group of neurons in a certain region which can exhibit many different behaviours such as continuous spiking and bursting. To observe normal spiking for longer periods the extracellular potassium has to be tightly regulated. This is achieved by increasing the maximum pumping rate of Na^+/K^+ ATPase exchange pump which restores the ionic equilibrium. Figure 3.4 shows the continuous spiking observed in the neuron membrane potential by increasing the maximum pumping rate of the Na^+/K^+ ATPase exchange pump to four times of its original value. This drastic change in membrane potential is due to the fact that the extracellular potassium is maintained in the physiological range (4-10mM).

Bursting is characterized by continuous spiking followed by quiescent periods. This characteristic is observed in most neuron types in the brain when a sub threshold current is applied. This behaviour is employed in a variety of mechanisms in the brain such as central pattern generator, neural synchronization, neural coding, plasticity, and attention. As it is an intrincic property of ion channel expression, the patterns of bursting are diverse. Figure 3.5 shows bursting in the neuron model and its associated potassium ion changes. When a sub threshold current is given to the neuron model bursting is generated.

Figure 3.6 also shows bursting in the neuron model and its associated potassium ion changes. The maximum pumping rate of Na^+/K^+ ATPase exchange pump which restores the ionic equilibrium was further increased to $5I_{max}$ to change the regulation of ECS ions and examine the effects on the behaviour of the neuron. The frequency of bursting here has increased as the voltage dependent gating of the ion channels also depends on the extracellular potassium concentrations. In addition to that, the threshold current required to generate bursting also increased as the ECS ions are more tightly regulated.

3.4 Model describing K^+ signalling mechanism

The model describing K^+ signalling mechanism is based on Dormanns et al [24]. Communication of the signalling mechanism and the change in vessel radius is simulated using three cell types and a model describing formation of cross bridges and its associated viscoelastic change in arterial wall. The hypothesis of neurovascular coupling used in this model is primarily based on the experimental result of Filosa et al[29] who demonstrated that during

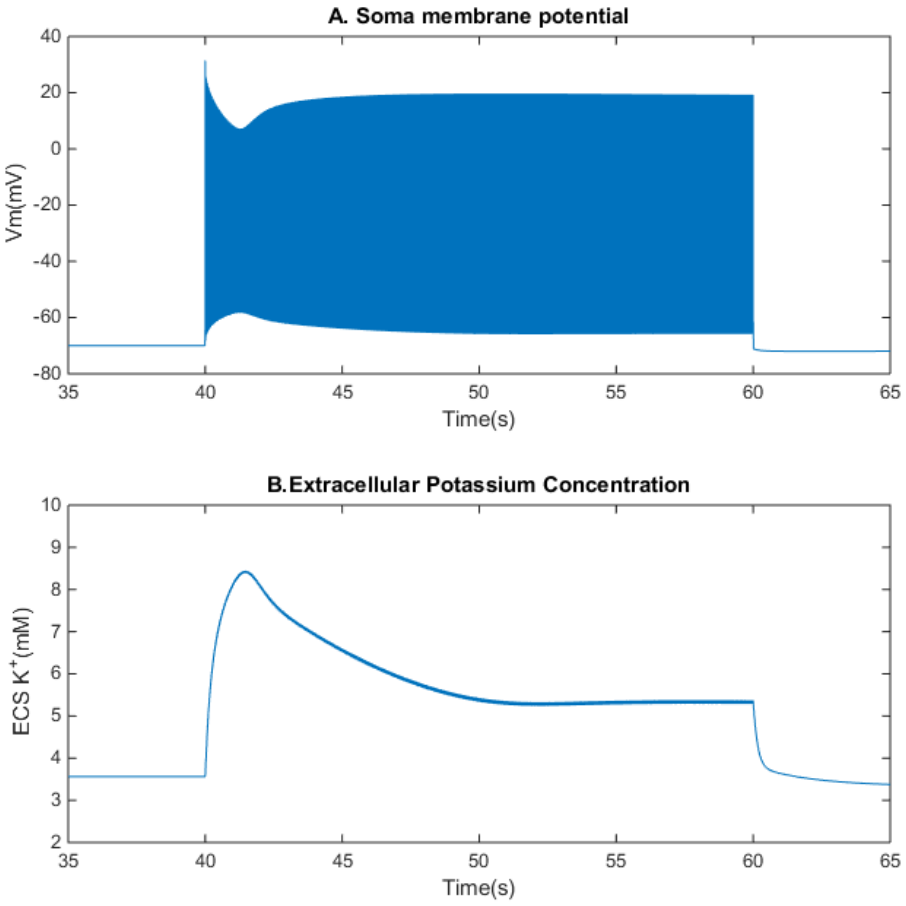

Fig. 3.4 Continuous spiking observed in the neuron model when the maximum pumping rate of the Na^+/K^+ ATPase exchange pump is increased to $4I_{max}$ to tightly regulate ECS potassium. A stimulus amplitude of $0.014 mA/cm^2$ and duration of 20 s in rectangular form was used in this simulation.

neural activity, the calcium activated large conductance potassium channels(BK) in the astrocyte and the inward rectifying channels in the smooth muscle cells(KIR) facilitate the neurovascular coupling mechanism. To describe this mechanism they used models of those cellular structures involved and extended them to add the necessary channels mentioned in the experimental data. The different models used and their extensions are described below.

3.4.1 Astrocytic(AC) cell model

The flux equations used in the astrocytic model are based on the model of Ostby et al [77]. They looked at the volume changes that occur in the astrocyte and synapse during neural

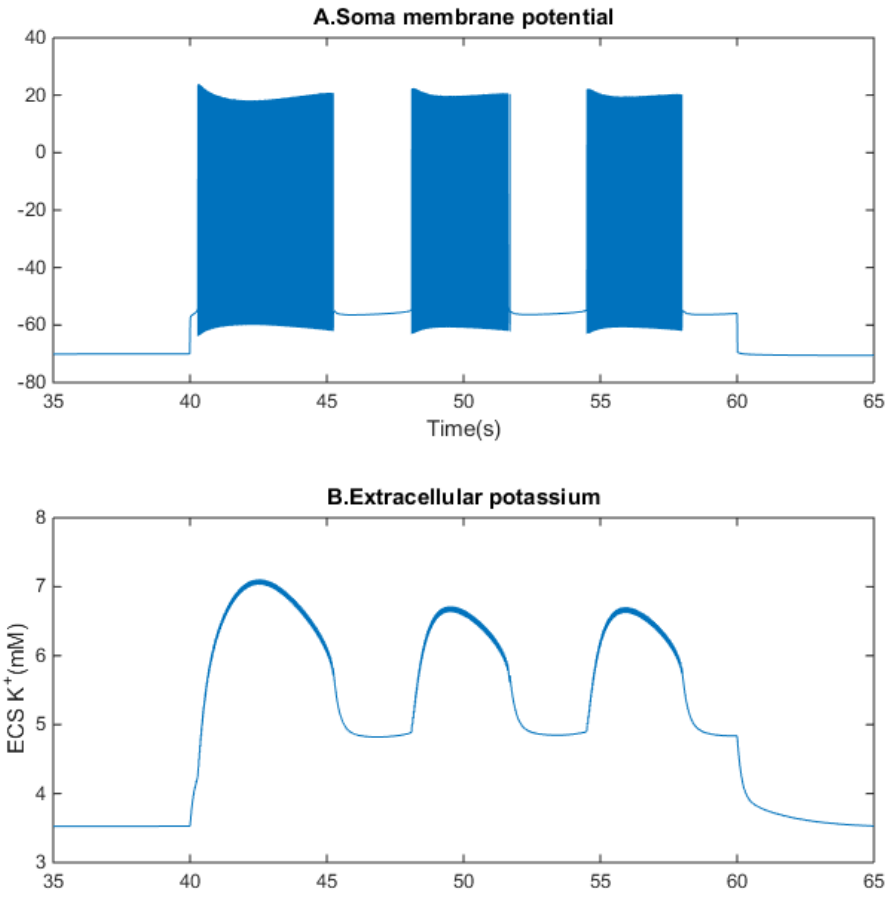

Fig. 3.5 Bursting observed in the neuron model when a sub threshold current is given to the soma. A stimulus amplitude of $0.012 mA/cm^2$ and duration of 20 s in rectangular form was used in this simulation.

activation to study the activity induced shrinkage of extraneuronal space as shown in Figure 3.7. The volumes of both the astrocyte and synapse are variables in this model and all fluxes are scaled by a volume-surface ratio of that particular compartment. With the assumptions that the sum of the volumes of the astrocyte and synaptic space is a constant and the neural activity induced extraneuronal space shrinkage is 30%, they estimated the rate at which the K^+ ions are expelled from the neuron and Na^+ ions are drawn into the neuron. The processes that can contribute to the shrinkage phenomenon such as the action of the Na^+/K^+-ATPase pump, transport of sodium, potassium and chloride ions through various ion channels, water transport through aquaporin(AQP4) channels in the perisynpatic membranes were studied in this model. The ion channels for potassium (J_{KCC1}, J_{NKCC1}, J_K, J_{NaK} and J_{BK}), sodium

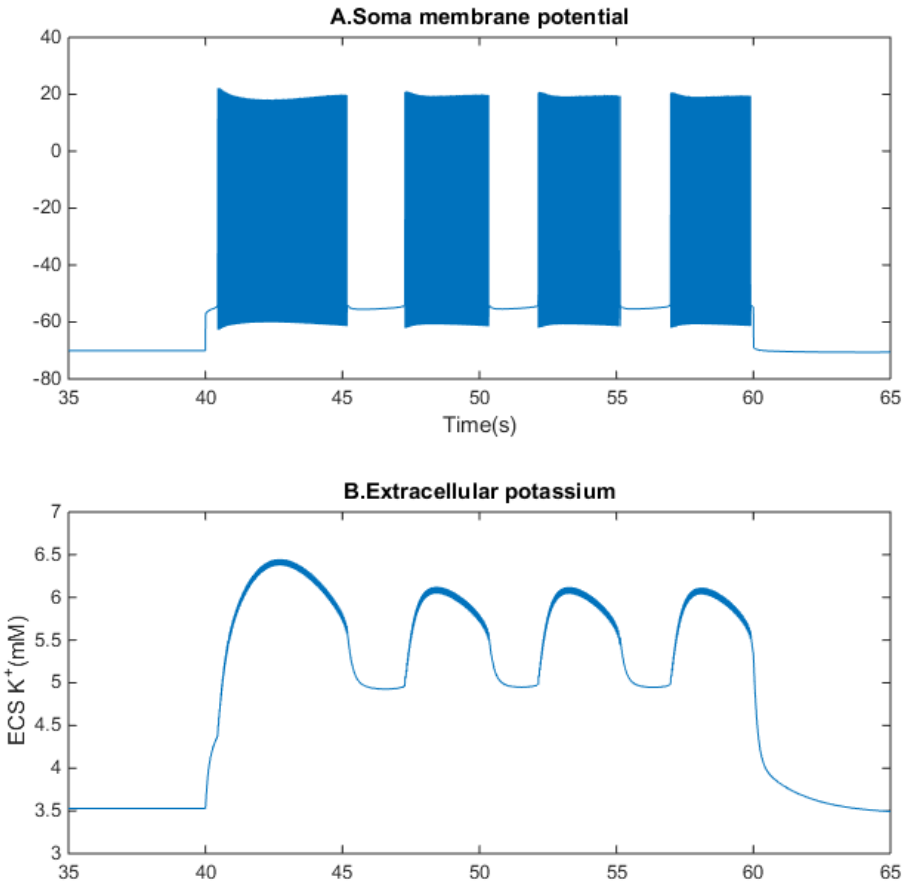

Fig. 3.6 Bursting frequency change observed in the neuron model when the maximum pumping rate of the Na^+/K^+ ATPase exchange pump is further increased to $5I_{max}$. A stimulus amplitude of $0.015 mA/cm^2$ and duration of 20 s in rectangular form was used in this simulation.

(J_{NBC}, J_{NKCC1}, J_{NaK} and J_{Na}), chloride (J_{KCC1}, J_{NKCC1} and J_{Cl}) and bicarbonate (J_{HCO_3}) were included.

In the astrocyte model, activity of the neuron is implemented by an influx of K^+ ions (J_{K_s}) and with a corresponding Na^+ ions uptake by the neuron (J_{Na_s}). They modelled the neural activity dependent K^+ ionic changes using a beta distribution with its parameters set in such a way that during stimulation, the time taken for it to peak is 5s and at 30s after stimulation it is at 70% of its peak. Buffering of potassium ions is modelled as a block function with a decay constant between 30s-40s after stimulation. In addition to that they switched ON or OFF the NKCC1 and KCC1 co-transporters during neural activity to study their relative contribution to extraneuronal space shrinkage. The differential equations and fluxes used in

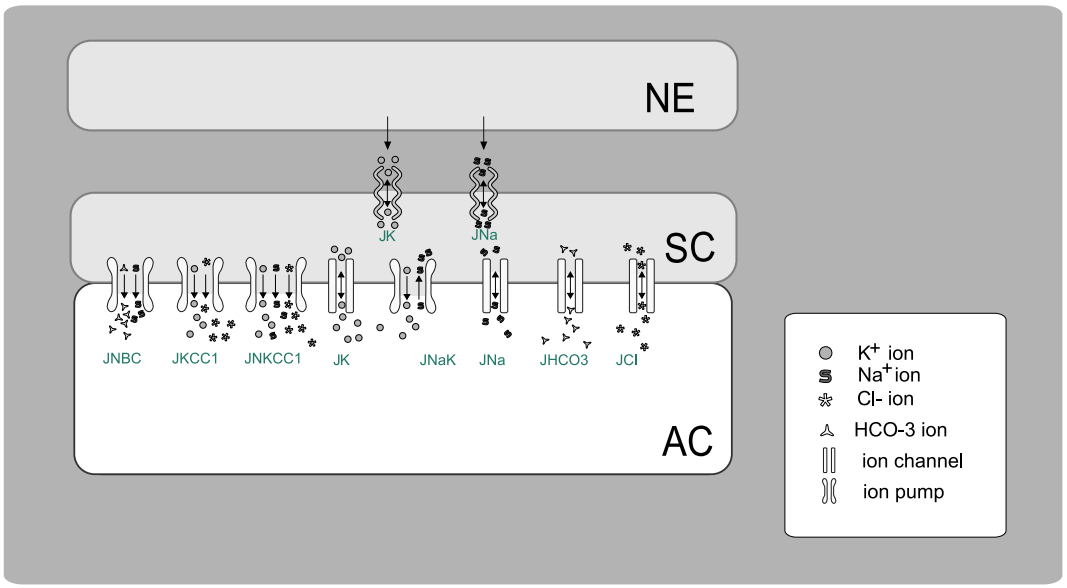

Fig. 3.7 Astrocyte model based on Ostby et al[77]

this model can be found in Dormanns et al [24].

3.4.2 Model of the vasculature

The model of the vasculature shown in Figure 3.8 is based on Koenigsberger et al [58] who studied the effects of pressure on vasomotion by describing the calcium dynamics in a population of coupled smooth muscle cells and endothelial cells. The model of Hai and Murphy [40] was used to relate the calcium level in the smooth muscle cell and the formation of cross bridges between the actin and myosin filaments. The blood vessel dilation or constriction is then calculated using a visco-elastic mechanical model which takes the fraction of attached myosin cross bridges as input and gives radius change as output.

3.4.2.1 Vascular smooth muscle cell (SMC) and Endothelial cell (EC) model

A cyclic variation in vessel diameter is termed vasomotion. This happens due to the synchronous oscillations of calcium in the smooth muscle cells. To study the effects of endothelial vasoactive factors on vasomotion, Koenigsberger et al developed a model that describes the calcium concentration in the smooth muscle cell, sarcoplasmic reticulum, endothelial cell and endoplasmic reticulum by a set of differential equations. The dynamics of calcium in the smooth muscle cell is affected by the calcium concentration in the cytocol, calcium

concentration in the sarcoplasmic reticulum, the cell membrane potential, the open state probability of calcium-activated potassium channels and the inositol triphosphate (IP_3) production whereas the dynamics of calcium concentration in the endothelial cell is affected by the calcium concentration in the cytocol, calcium concentration in the endoplasmic reticulum , cell membrane potential and the IP_3 concentration. When agonists such as ATP bind to cell surface receptors, it activates Phospholipase C(PLC). It induces release of secondary messengers such as IP_3 which in turn releases calcium from the intracellular stores. This leads to vasconstriction. The synchronous oscillations are then achieved by inter cellular communications (both homocellular and heterocellular) through gap junctions mediated by electrical, calcium and IP_3 couplings. As the assumption of Dormanns et al is that an aggregate of cells can be considered as one compartment of each cell type, they only considered heterocellular coupling between the cells. With that model they showed calcium oscillations for certain values of endothelial agonist production rate. The three types of coupling used between the SMC and EC are given by the diffusional flux equations below
Heterocellular calcium coupling between SMCs and ECs:

$$J^{EC-SMC}_{Ca^{2+}-cpl} = -P_{Ca^{2+}}([Ca^{2+}]_i - [Ca^{2+}]_j) \tag{3.19}$$

Heterocellular voltage coupling between SMCs and ECs :

$$V^{EC-SMC}_{cpl} = -G_{coup}(v_i - v_j) \tag{3.20}$$

Heterocellular IP_3 coupling between SMCs and ECs :

$$J^{EC-SMC}_{IP_3-cpl} = -P_{IP_3}((IP_3)_i - (IP_3)_j) \tag{3.21}$$

where the subscripts i,j refers to EC and SMC respectively. Even though the gap junctions can have voltage gating properties, the conductances ($P_{Ca^{2+}}$, G_{coup}, P_{IP_3}) are considered as constants in this model. The differential equations, fluxes and parameter values used in the contraction and mechanical model can be found in Dormanns et al [24].

3.4.2.2 Contraction and Mechanical Model

Actin and myosin filaments that slide over each other due to the formation of cross bridges is the fundamental unit of contraction in the smooth muscle cell. The cross bridge formation is simulated based on the model of Hai and Murphy [40]. This model is based on the assumptions that the regulation of contraction is done only by calcium dependent myosin

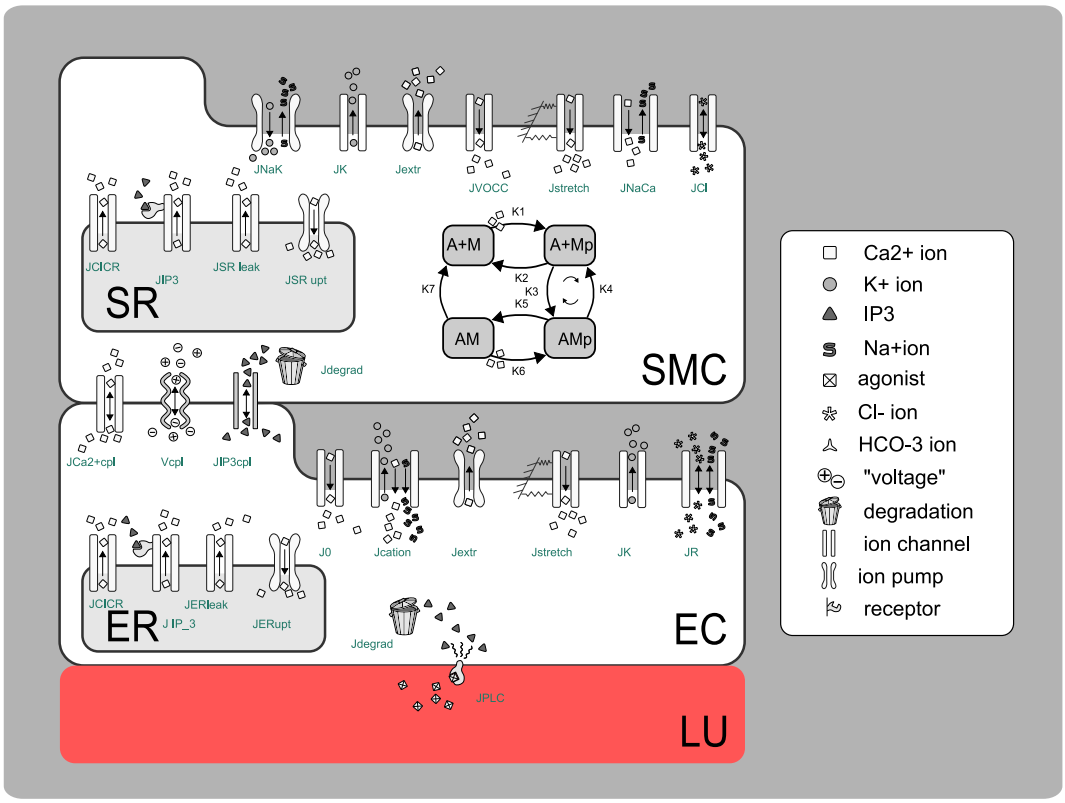

Fig. 3.8 Model of vasculature based on Koenigsberger et al [58]

phosphorylation, each myosin head acts independently and only dephosphorylation of an attached cross bridge lead to the formation of a latch bridge. In the process of contraction, the mysoin can exist in four possible states namely free nonphosphorylated cross bridges (M), free phosphorylated cross bridges (Mp), attached phosphorylated cross bridges (AMp), and attached dephosphorylated latch bridges (AM). The fraction of myosin in any of these states is described by the following differential equations.
Fraction of free phosphorylated cross-bridges (dimensionless):

$$\frac{\mathrm{d}[Mp]}{\mathrm{d}t} = K_4[AMp] + K_{1_j}[M] - (K_2 + K_3)[Mp] \tag{3.22}$$

Fraction of attached phosphorylated cross-bridges (dimensionless):

$$\frac{\mathrm{d}[AMp]}{\mathrm{d}t} = K_3[Mp] + K_{6_j}[AM] - (K_4 + K_5)[AMp] \tag{3.23}$$

Fraction of attached dephosphorylated cross-bridges (dimensionless):

$$\frac{\mathrm{d}[AM]}{\mathrm{d}t} = K_5[AMp] - (K_7 + K_{6_j})[AM] \tag{3.24}$$

Fraction of free non-phosphorylated cross-bridges (dimensionless):

$$[M] = 1 - [AM] - [AMp] - [Mp] \tag{3.25}$$

where K_n(n=1,2,..,7)and the calcium dependent rate constants K_{1_j}, K_{6_j} that represent phosphorylation of M to Mp and of AM to AMp respectively are given by

$$K_{1_j} = K_{6_j} = \gamma_{cross}[Ca^{2+}]_i^n \tag{3.26}$$

where the constant γ_{cross} characterizes the Ca^{2+} sensitivity of the calcium activated phosphorylation of myosin. The fraction of attached cross bridges (F_r) is then given by the equation

$$F_r = frac[AM_p] + [AM][AM_p]_{max} + [AM]_{max} \tag{3.27}$$

A visco-elastic mechanical model based on the work of Kudryashov et al [60] was used to find the change in radius of the artery based on the fraction of the attached myosin crossbridges. Active stress in the circumferential direction of the smooth muscle cell is proportional to the fraction of attached myosin cross bridges and the active stress is related to the radius through Laplace's law. The radius change is given by the equations

$$\frac{\mathrm{d}R}{\mathrm{d}t} = \frac{R_{0_{pas}}}{\eta}\left(\frac{R\Delta p}{h} - Y(F_r)\frac{R - R_0(F_r)}{R_0(F_r)}\right) \tag{3.28}$$

here $R_{0_{pas}}$ is the radius of the artery in the passive state without any stress applied, η is the viscosity of the arterial wall, Δp is the transmural pressure, h the vessel wall thickness such that

$$Y(F_r) = Y_{pas} + F_r\,(Y_{act} - Y_{pas}) \tag{3.29}$$

$$R_0(F_r) = R_{0_{pas}} + F_r\left(H - R_{0_{pas}}\right) \tag{3.30}$$

where the passive and active Young's moduli, Y_{pas} and Y_{act}, and baseline radii, $R_{0_{pas}}$ are estimated based on the experimental data of Gore et al [35]. H is a scaling factor for baseline radius. The parameter values used in the contraction and the mechanical model is from Dormanns et al[24].

3.4.2.3 Communication between the astrocyte and smooth muscle cell

To model the interaction between the astrocyte and the vasculature Dormanns et al added a BK channel to the astrocyte, a KIR channel to the smooth muscle cell and a perivascular space compartment to enable communication between them. These channels were added based on the experimental suggestion of Filosa et al who examined the local K^+ signalling mechanism of neurovascular coupling. Figure 3.9 shows the extension made to the astrocyte and vasculature model.

The BK channel flux of the astrocyte is given by the equation

$$J_{\mathrm{BK},k} = \frac{g_{\mathrm{BK},k}}{F} w_k \left(v_k - E_{\mathrm{BK},k}\right) \tag{3.31}$$

where $E_{\mathrm{BK},k}$ if the nernst potential of the BK channel given by

$$E_{\mathrm{BK},k} = \frac{R_{\mathrm{gas}} T}{z_K F} \ln\left(\frac{[K^+]_p}{[K^+]_k}\right) \tag{3.32}$$

where K_p and K_k are the K^+ concentrations in the perivascular space and astrocyte compartments respectively, z_K is the ionic valence, and F is the Faraday's constant. The membrane voltage mediated open probability of the BK channel w_k is given by the differential equation

$$\frac{\mathrm{d}w_k}{\mathrm{d}t} = \phi_w \left(w_\infty - w_k\right) \tag{3.33}$$

where ϕ_w is the characteristic time constant given by

$$\phi_w = \psi_w \cosh\left(\frac{v_k + v_6}{2v_4}\right) \tag{3.34}$$

Here v_4 is the voltage associated with the opening of half the population of channels in the astrocytic cell and v_6 is the calcium dependent parameter which is assumed to be a constant as this model does not consider calcium concentration in the astrocyte. ψ_w is the charateristic time for the open probability of the BK channel. The conductance $g_{\mathrm{BK},k}$ is estimated from the experimental data of Filosa et al [29].

The flux through the KIR channel that is an extension to the smooth muscle cell is given by the equation

$$J_{\mathrm{KIR},i} = F_{\mathrm{KIR}}, ig_{\mathrm{KIR},i}(v_i - v_{\mathrm{KIR},i}) \tag{3.35}$$

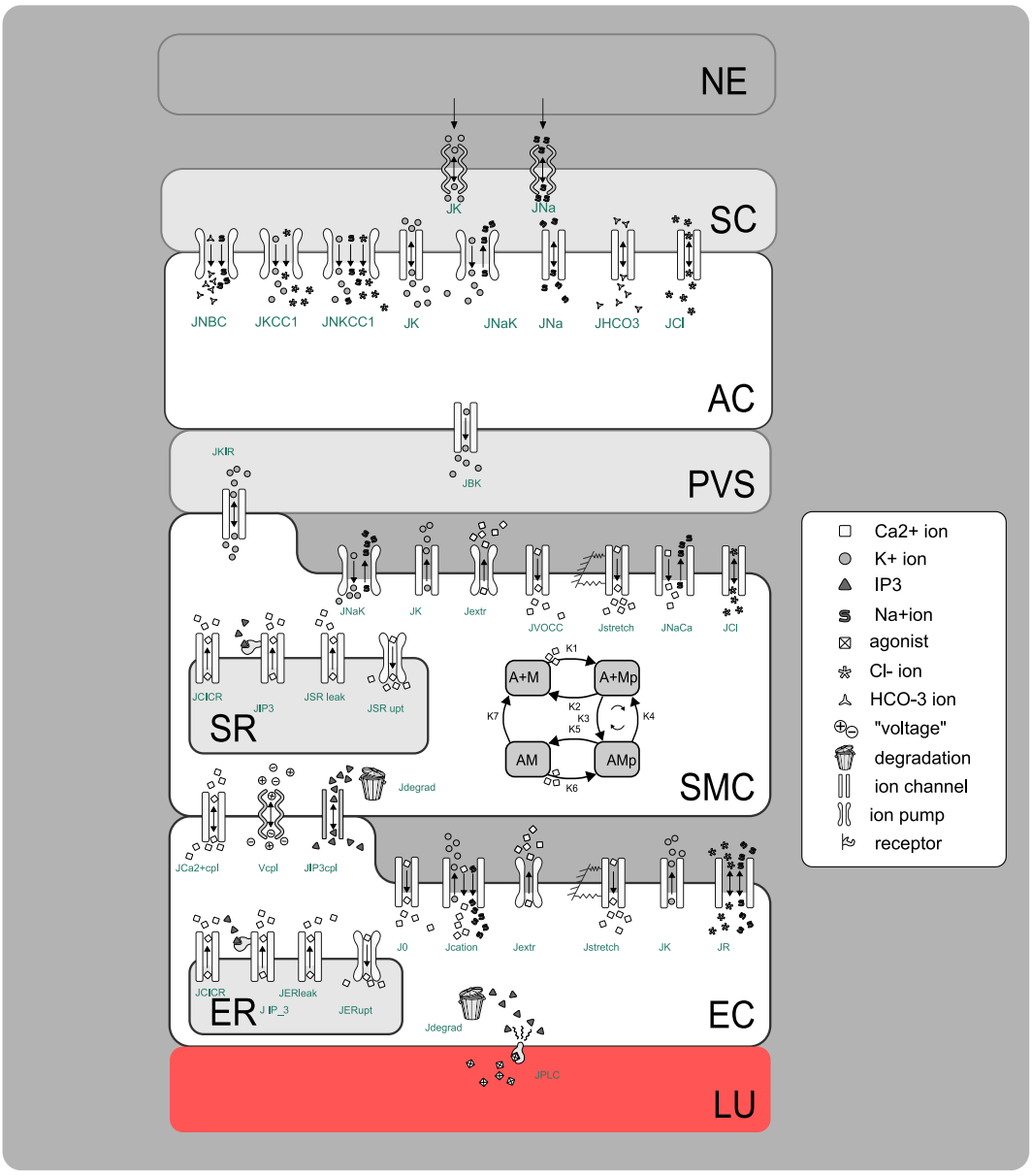

Fig. 3.9 Communication between the astrocyte and the smooth muscle cell through the perivascular space. Figure adapted and modified with permission from Dormanns et al [24]

where $v_{\mathrm{KIR},i}$ is the Nernst potential of the KIR channel(in mV) and $g_{\mathrm{KIR},i}$ is the conductance of the KIR channeland they are given by:

$$v_{\mathrm{KIR},i} = z_1[K^+]_p - z_2 \tag{3.36}$$

$$g_{\mathrm{KIR},i} = \exp(z_5 v_i + z_3[K^+]_p - z_4) \tag{3.37}$$

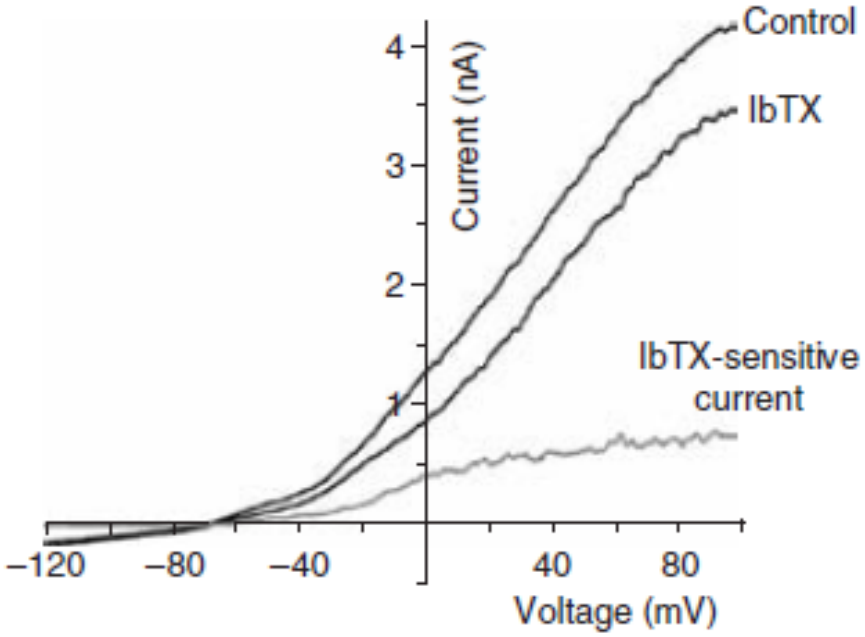

Fig. 3.10 BK channel I-V curve of astrocyte before and after 7 min exposure to a specific BK channel inhibitor IbTX (200 nM). Currents were recorded in response to 200ms long voltage ramps from –120 mV to 100 mV with a holding potential of –80 mV. The IbTX-sensitive current is the difference between the control and the IbTX exposed I-V curve. The conductance of whole cell astrocytic BK channel is then obtained by finding the slope of the IbTX-sensitive I-V curve. Figure reproduced from Filosa et al [29].

z_1 and z_2 are obtained by fitting a linear function to the data of Filosa et al. The parameters z_3, z_4 and z_5 are estimated by plotting the conductance function for three different values of perivascular potassium concentrations against the experimental data of Filosa et al. It is shown in figure 3.11.

The concentration of K^+ concentration in the perivascular space is given by the equation

$$\frac{dK_p}{dt} = \frac{J_{BK,k}}{R_{pk}} + \frac{J_{KIR,i}}{R_{ps}} - R_{decay}([K^+]_p - [K^+]_{p,min}); \tag{3.38}$$

where R_{pk} is the volume ratio of PVS to AC, R_{ps} is the volume ratio of PVS to SMC, $[K^+]_{p,min}$ is the steady state perivascular potassium concentration.

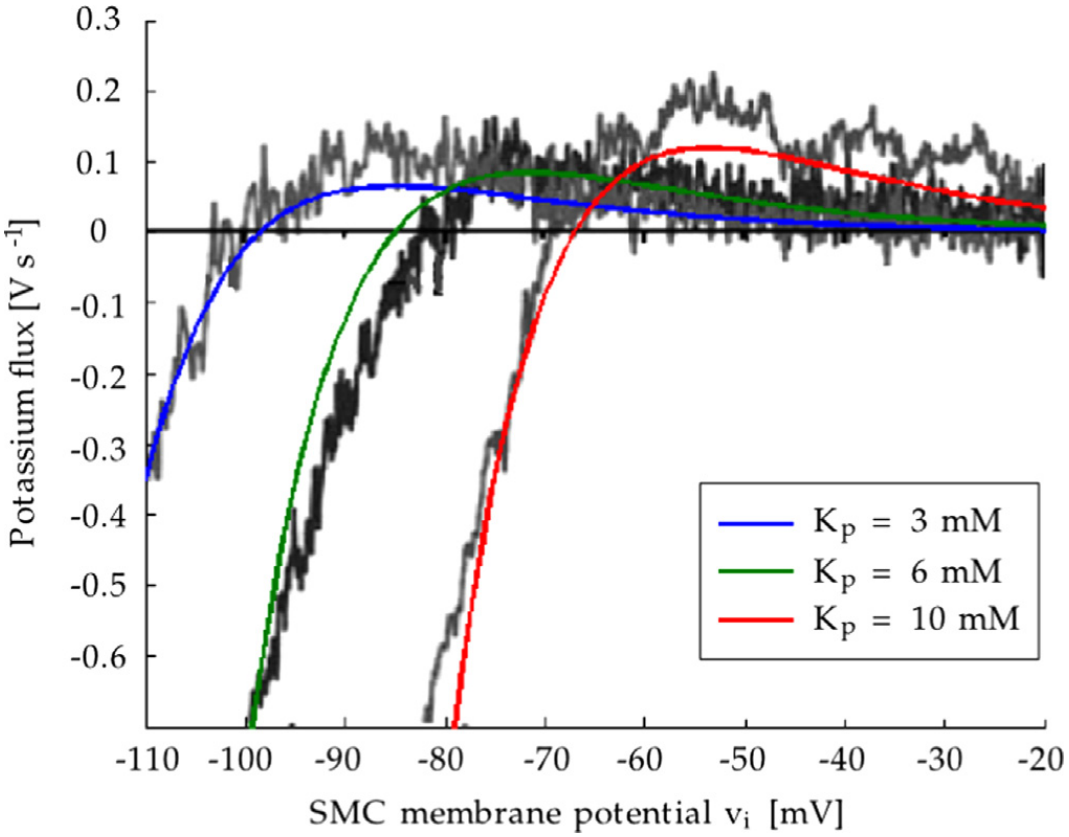

Fig. 3.11 Experimental data of Filosa et al is plotted against the conductance function $g_{\mathrm{KIR},i}$, reproduced from Dormanns et al [24]. Experimental Ba^{2+} sensitive current densities are obtained and averaged I-V relationships from three cells for 3mM$[K]_0$ and four cells for both 6mM$[K]_0$ and 10mM$[K]_0$ are plotted against the KIR conductance function for similar values of perivascular potassium concentrations.

3.5 Results of the Vascular response through K^+ signalling mechanism

The vascular model is stimulated with a input form described in section 3.1.1 representing ionic changes during neural activity. Figure 3.12 illustrates how neural activity leads to vessel dilation though the K^+ signaling pathway in the neurovascular coupling model. Depolarisation of the neuronal membrane leads to a rise of K^+ in the synaptic space (see Figures 3.12A). It results in an increased K^+ uptake by the astrocyte which consequently undergoes depolarization. This causes a K^+ efflux at the end-feet of the astrocyte through the BK channel into the perivascular space as shown in (Figure 3.12B). The higher level of K^+ in the perivascular space(Figure 3.12C) activates the KIR channel on the smooth muscle cell causing a further increase in the efflux of potassium into the perivascular space(Figure

3.12D). This efflux of cytosolic K^+ hyperpolarizes the SMC, forcing the voltage-operated Ca^{2+} channel (VOCC) to close (Figure 3.12E, 3.12F), preventing further influx of Ca^{2+} into the SMC. The decreased intracellular Ca^{2+} concentration in the smooth muscle cell decreases the fraction of attached myosin cross bridges which results in vessel dilation (Figure 3.12G, 3.12H).

The vascular response is also simulated by changing the agonist production rate from $0.18\mu\text{Ms}^{-1}$ to $0.4\ \mu\text{Ms}^{-1}$. This acts as a stimulus from the endothelial side in addition to the stimulus through astrocyte. Figure 3.13 shows the how the vascular response is affected by this luminal stimulus. The radius starts oscillating and also lead to constriction of the artery. Neurovascular coupling is suppressed in this process.

3.6 Discussion

In this chapter, we have presented a neuron model with time dependent ionic concentrations, a model of vasculature and astrocyte. The results give some general conclusions on neuron models with time dependent ionic concentrations. As long as the potassium concentration is maintained in the physiological range the neuron model will either be in a state of continuous firing or will be in a state of bursting. If it is not maintained by proper regulatory mechanisms, the neural model will eventually enter spreading depression mode. This is especially true in the neuron model used in this study as it was specifically designed to study cortical spreading depression. Both the NaP (sodium persistent) channel and the potassium dependent NMDA (N-methyl-D-aspartate) channel included in the neuron model acts synergestically to drive the extracellular potassium high. Spreading depolarization and seizures observed follow a common mechanism to be generated. Increases in ionic currents produce spreading depolarizations which in turn further increases the ionic concentrations. These results indicate the importance of potassium ion regulation in the brain.
Increasing the value of the maximum pumping rate introduces fast spiking and bursting dynamics in the neuron model. As the aim of the neuron model is to approximately quantify the extracellular changes that occur due to a large number of neurons in a certain region, repetitive firing and bursting are generated by tightly regulating the ionic changes. The channel maximal conductances, gating functions and pump strength determine the intrinsic ability and type of bursting in neurons. While certain type of bursting is correlated to gamma frequency (30-70 Hz), the spreading depolarization is correlated with the delta band (0.5 to 4Hz)[49].

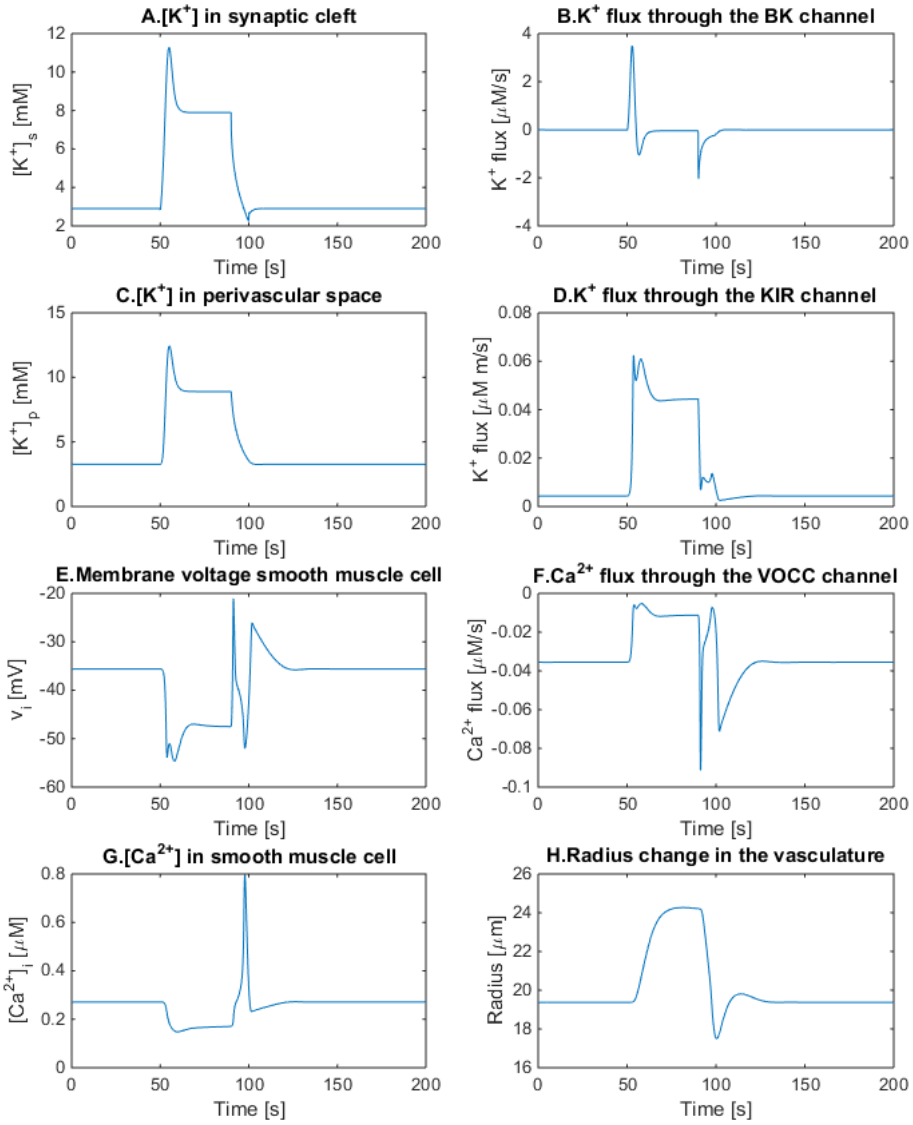

Fig. 3.12 Vascular response simulated with model of Dormanns et al. An efflux of potassium into the synaptic space during neural activation lead to dilation of the vessel through K^+ signalling mechanism

Every neuron in its active state requires high amounts of energy and hence it employs many signalling mechanisms to provide the energy they require. Based on the strong evidence supporting K^+ signalling mechanism, the neuron model communicates with the vasculature through that mechanism. The increase of K^+ ions in the SC results in an increased K^+

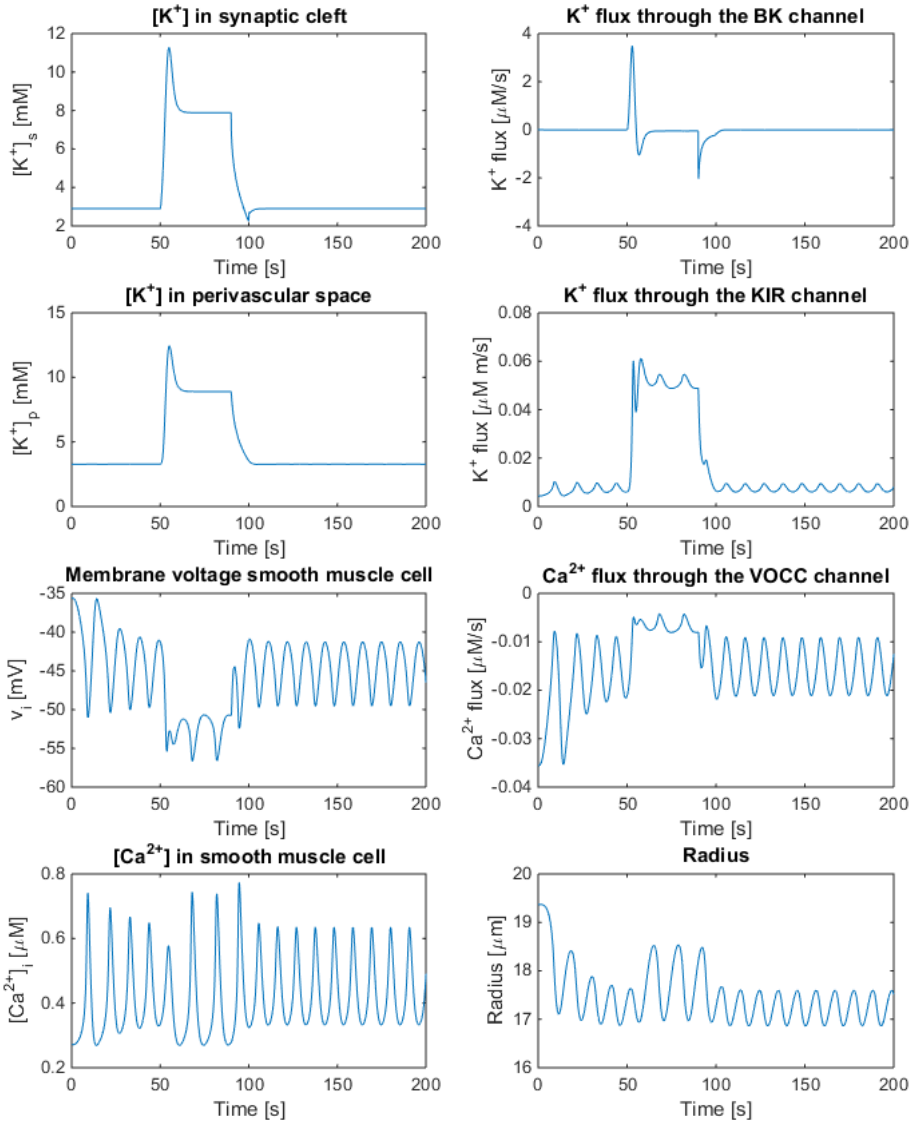

Fig. 3.13 Agonist induced vessel oscillation in the Dormanns et al model. Simulated with the same neural input and parameter values similar to Figure 3.12 except the change of agonist production rate in the endothelium from $0.18\mu\text{Ms}^{-1}$ to $0.4\ \mu\text{Ms}^{-1}$

uptake by the astrocyte which consequently undergoes depolarization. This results in a K^+ efflux from distant portions of the cell. Since most of the K^+ conductance of astrocytes is located at the end-feet, the outward current-carrying K^+ would flow out of the cell largely through these locations. Consequently, the K^+ is 'siphoned' to the end-feet of the astrocyte

and released into the perivascular space which leads to an increase of K^+ in the PVS. This K^+ release leads to a repolarization of the membrane voltage and is the input signal for the smooth muscle cell.
While the results of the model suggests that potassium ions released during neural activity could act as the main mediator in neurovascular coupling, along with cytosolic calcium in the smooth muscle cell it certainly does not rule out the possibility of other mechanisms that can coexist and increase blood flow, such as the nitric oxide signalling mechanism or the archidonic acid to EET pathway [27]. The high potassium efflux from the neuron leading to vasoconstriction in the model shows that the neurovascular coupling response cannot be thought of as a linear time-invariant system of neural activity in any region as some earlier studies suggested [10]. This also emphasizes the need to understand how each of the experimentally identified vasoactive factors influence the blood vessel response.

3.7 Conclusions

The fundamental units of the neurovascular coupling model such as the neuron, astrocyte and vasculature were presented in this section and the results arising out of them were discussed. The neuron model exhibits different kinds of behaviours such as continuous spiking, bursting and cortical spreading depression for varying regulation of extracellular potassium concentration. In this model the regulation is primarily done by the Na^+/K^+ ATPase exchange pump and the phenomenological potassium buffer. For certain sub threshold stimulus currents the model generates bursting and for high threshold currents it goes into cortical spreading mode. The neurovascular response simulated with the model of Dormanns et al provided 23% increase in radius for a 50s long stimulation and it provided only a 2% increase for 10s long stimulation. The vascular response of the model entered an oscillatory state for certain values of IP_3 production rate in the endothelium and this suppressed the neurovascular coupling mechanism with contraction.

Chapter 4

Integration of the neuron, astrocyte and the vasculature

4.1 Introduction

In this chapter the coupling between the neuron, astrocyte and vasculature is described and the vascular responses for different kinds of neural activity are presented. A distinction has to be made here between the extracellular space and the synaptic space. The extracellular space can be broadly referred to as the space outside any cell. However the synapse is a specific space between two neurons where communication between them happens and it is much smaller compared to the extracellular space. Even though it is a continuum with extracellular space, the ionic and chemical composition is different. Little evidence exists in the literature to distinctly quantify the ionic movements between extracellular space and synaptic space. However strong evidence exists to suggest that during normal neural activity the communication between the neuron and the astrocyte occurs near the synaptic side of the neuron, as the astrocyte endfeet is perfectly positioned there structurally [51]. Experimental studies also suggests that during cortical spreading depression the communication between neurons happens through the extracellular space. Hence appropriate assumptions are taken to model normal neural activity and cortical spreading depression.

4.2 Coupling between the neuron and astrocyte

The neuron model exhibits both normal and abnormal characteristics and hence they are coupled to the astrocyte in two different ways corresponding to the behaviour of the neuron.

The one where the neuron model behaves pathologically with characteristics of cortical spreading depression, the communication happens between the neurons through propagating waves of potassium in the extracellular space. This means that only a fraction of ions entering the extracellular space can enter the synapse as the astrocytic endfeet is only positioned near the synapse. Hence the CSD neuron model is coupled to the astrocyte by assuming that a fraction of the ions entering the extracellular space enters the synapse. It is also assumed that the K^+ signalling mechanism is the only active neurovascular mechanism during neural activity and the Na^+/K^+ ATPase pump which restores ionic homoeostasis is the only active consumer of oxygen during this process. The mathematical model which describes the K^+ signalling pathway of neurovascular coupling supported by validation with the experimental work of Filosa at al [29] has six compartments comprising a synaptic space, astrocyte, perivascular space, smooth muscle cell, endothelial cell and lumen compartment. The synaptic space and astrocyte model was based on Ostby at al [77] and was extended by adding a BK channel at the endfeet. In this astrocyte model, the length of the astrocyte can vary while its cross-sectional area remains fixed. Therefore, ionic variables are converted from concentration $[Ion]_c$ to the number $N_{c,Ion}$ of moles of ion per unit cross-sectional area via

$$N_{c,Ion} = S_c[Ion]_c, \tag{4.1}$$

where S_c is the length of the particular compartment. Ostby et al modelled the flux of sodium and potassium from the neuron into the synaptic space as a phenomenological input term. We modify this by assuming that the flux from the neuron into the synaptic space is equal to a fraction of the flux from neuron into the extracellular space. The fraction is equal to the volume ratio of the synaptic space to the extracellular space. The modified equations of the astrocyte model for this case are such that

$$\frac{\mathrm{d}N_{syn,Na^+}}{\mathrm{d}t} = \frac{\mathrm{d}N_{e,Na^+}}{\mathrm{d}t}\frac{S_{syn}}{S_e} - J_{Na^+,SC\to AC} \tag{4.2}$$

$$\frac{\mathrm{d}N_{syn,K^+}}{\mathrm{d}t} = \frac{\mathrm{d}N_{e,K^+}}{\mathrm{d}t}\frac{S_{syn}}{S_e} - J_{K^+,SC\to AC} \tag{4.3}$$

where $J_{ion,SC\to AC}$ is the net flux of ion from the synaptic cleft to the astrocyte as defined by the model of Ostby. The second one is where the neuron model functions normally by spiking or bursting to communicate with another neuron. In this case the communication happens through the synaptic side. To facilitate synaptic transmission the action potential has to travel along the axon till it reaches the synapse. This causes ionic efflux and influx near the synapses and the synaptic cleft which can then communicate with the astrocyte effectively as the astrocytes express high density of ion channels near the synapses [74]. The coupling

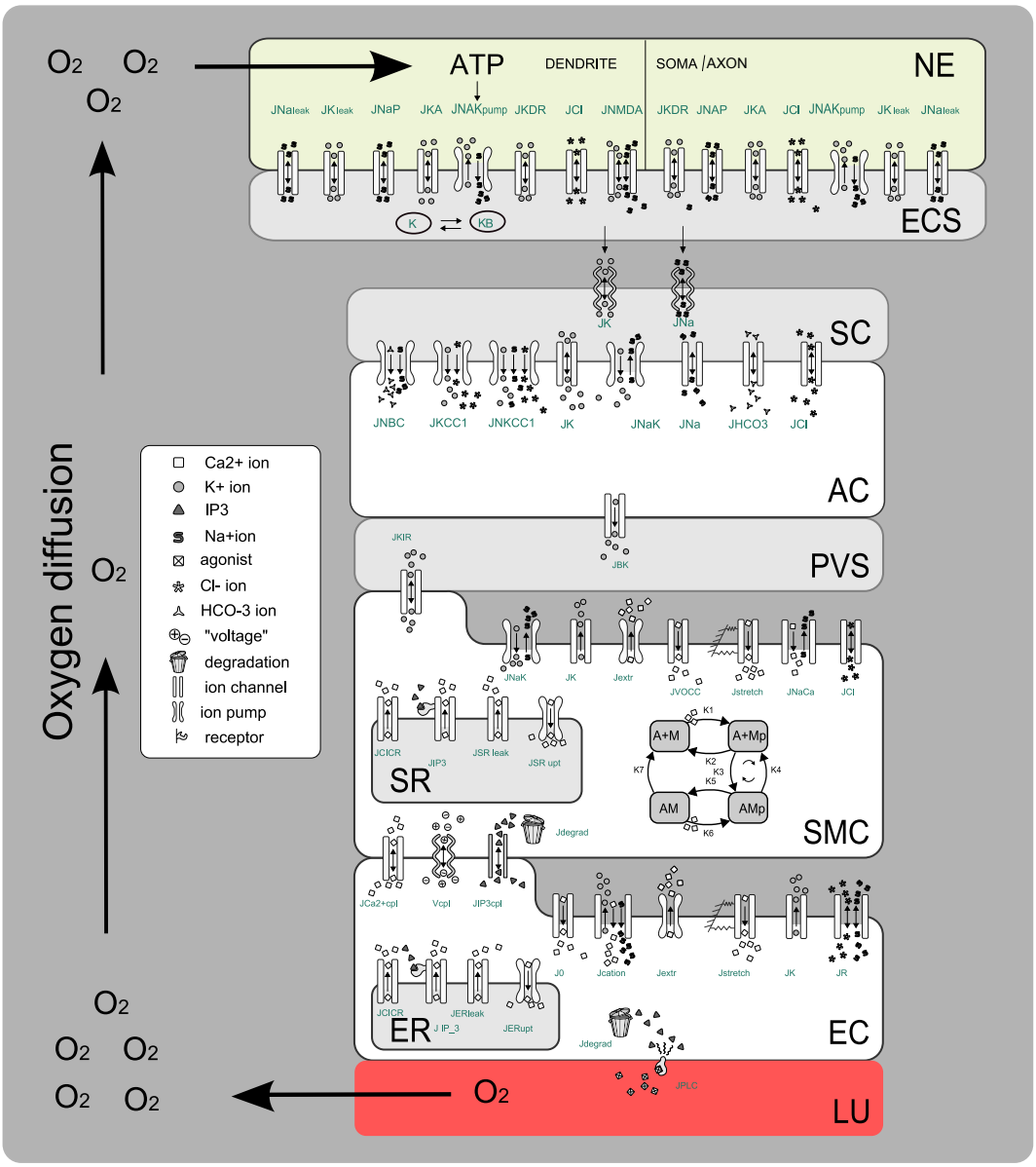

Fig. 4.1 Coupled neurovascular system. Neuron is coupled to the vasculature through the astrocyte and the vasculature is coupled back to the neuron through the sodium potassium exchange pump

between the astrocyte and the neuron is done by assuming that the flux from the neuron into the synaptic space is equal to fraction of the scaled flux from the neuron into the extracellular space. The fraction is equal to the volume ratio of the synaptic space to the extracellular space. The scaling is given by the ratio of the extracellular volume to synaptic volume times the fraction of synapses near the astrocytic end process . The modified equations in this case

are given by

$$\frac{dN_{syn,Na^+}}{dt} = k\frac{dN_{e,Na^+}}{dt}\frac{S_{syn}}{S_e} - J_{Na^+,SC\rightarrow AC} \tag{4.4}$$

$$\frac{dN_{syn,K^+}}{dt} = k\frac{dN_{e,K^+}}{dt}\frac{S_{syn}}{S_e} - J_{K^+,SC\rightarrow AC} \tag{4.5}$$

where k is the scaling factor given by

$$k = \frac{V_e}{V_{syn}} f_{AS} \tag{4.6}$$

where V_{syn} is estimated based on the experimental results of Ventura and Harris [99] who studied the structural relationships between hippocampal synapses and astrocytes using serial electron microscopy and three-dimensional analyses and the experimental data of Megas et al [71] who studied the distribution of inhibitory and excitatory synapses on hippocampal CA1 pyramidal cells. These experimental results were chosen as the morphological and electrical properties of the neuron model are based on hippocampal cells. The experiment done by Megas et al [71] revealed that there was 31700 synapses present in a CA1 pyrammidal cell. The sample volume in the experiment done by Ventura and Harris [99] identified 229 complete synaptic complexes, of which 197 had macular type of synapses and 32 had perforated type of synapses. Only the macular type of synapses has the synaptic specializations necessary for synaptic transmission and they accounted for 86% of the total synapses in the sample volume. Based on these reasons, the interaction between the neuron and astrocyte is assumed to take place through the macular synapses. The volume of the synaptic cleft ranged from 0.15×10^{-15} to $2.1 \times 10^{-15} m^3$ at macular synapses and only a fraction (0.47 ± 0.23) of the macular synapses were found to be surrounded by the astrocytic profiles. Using these data, the scaling factor was estimated to be in the range of 4.204 to 171.

4.3 Coupling between the vasculature and the neuron

The coupling between the vasculature and the neuron is done by giving the vascular response dependent tissue oxygenation changes as an input to sodium potassium exchange pump in the neuron. The blood flow in the perfusing arterioles can be modelled as Poiseuille type [101] where the volume flow rate is proportional to the perfusing arterial radius to the fourth power. The cerebral blood flow, B is given by the equation

$$B = B_0 \frac{R^4}{{R_0}^4} \tag{4.7}$$

where R_0 and B_0 are the steady state values of radius and cerebral blood flow respectively. The sodium potassium exchange pump in the neuron is dependent on oxygen as defined by equation 3.9. The tissue oxygen concentration and the consumption of oxygen by the sodium potassium exchange pump is given by

$$\frac{\mathrm{d}[O_2]}{\mathrm{d}t} = J\frac{[O_2]_b - [O_2]}{[O_2]_b - [O_2]_0} - J_0 P([O_2])(1-\theta) - C_p \tag{4.8}$$

C_p is the consumption of oxygen by the pump defined by

$$C_p = J_0 P([O_2])\theta \frac{\gamma_{s,pump,1}([K^+]_e, [Na^+]_{i,s}) + \gamma_{d,pump,1}([K^+]_e, [Na^+]_{i,d})}{\gamma_{s,pump,1}([K^+]_{e,0}, [Na^+]_{i,0}) + \gamma_{d,pump,1}([K^+]_{e,0}, [Na^+]_{i,0})} \tag{4.9}$$

and

$$P([O_2]) = \frac{\gamma_{pump,2}([O_2]) - \gamma_{pump,2}(0)}{\gamma_{pump,2}([O_2]_0) - \gamma_{pump,2}(0)} \tag{4.10}$$

so that $P([O_2])$ is the pump rate normalized by the steady state pump rate, $[O_2]_b$ is the arterial oxygen concentration at steady state and $[O_2]_0$ is the baseline concentration of oxygen in the tissue. J is the change in oxygen concentration in the blood due to cerebral blood flow

$$J = J_0 \frac{B}{B_0} \tag{4.11}$$

in this case J_0 is the steady state change in oxygen concentration due to cerebral blood flow. The first term in equation 4.8 describes the amount of oxygen supplied to the tissue and the second term describes the consumption of oxygen by pumps and cellular processes that remain constant during neural activation. The equation 4.9 describes the consumption of the sodium potassium exchange pump which is active during neural activation. The parameter $0 < \theta < 1$ is the fraction of oxygen consumed by the pump which has been estimated to have a value between 0.10 to 0.70 [61, 3].

4.4 Results

In this section the results of the coupled neurovascular system is presented for different behaviours of the neuron model. The effects of stimulus conditions and the effects of oxygen dependency of the pump on the neuron pathology is also presented and discussed. The difference between vascular responses for normal and bursting conditions are also presented.

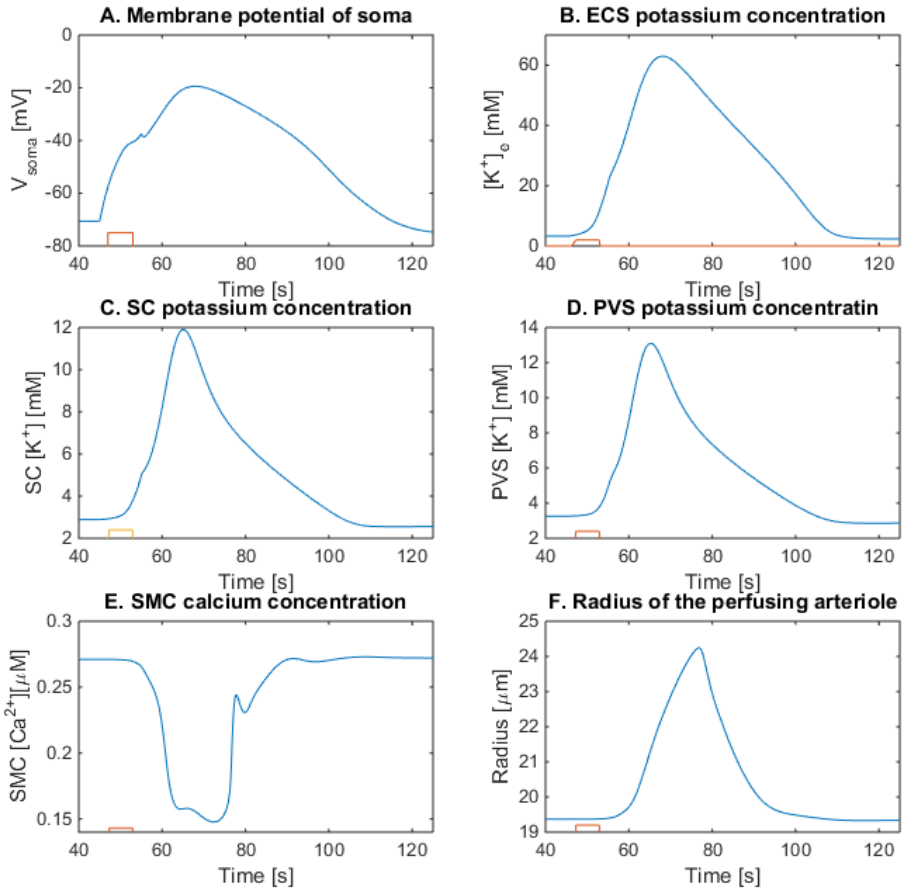

Fig. 4.2 Soma of the neuron model without the NaT channel is stimulated with a current intensity 9.5×10^{-4}mA/cm^2 in rectangular form for 6s causing dilation.

4.4.1 Vascular response for coupling with CSD neuron model without NaT channel

At first to examine the effects of CSD on the vascular response without the NaT channel in the neuron, the soma of the neuron model is stimulated with a current intensity 9.5×10^{-4}mA/cm^2 in rectangular form for 6s. This opens up the voltage dependent ion channels pushing them to a depolarized state as shown in Figure 4.2A. Spiking was not observed for any stimulus conditions and the steady depolarisation lead to a huge rise in extracellular potassium concentration (60 mM) Figure 4.2B. A fraction of this extracellular potassium flows into the synaptic space and increases its potassium concentration to about 12 mM (Figure 4.2C). This then drives the radius change through the K^+ signalling mechanism discussed in the previous chapter shown in Figure 4.2D, 4.2E, 4.2F. When the stimulus intensity and duration are

increased by 50% of its original value, the ECS potassium gets even more higher causing upto 20mM change in the perivascular space (Figure 4.3D) and consequently generating constriction (Figure 4.3E, 4.3F).

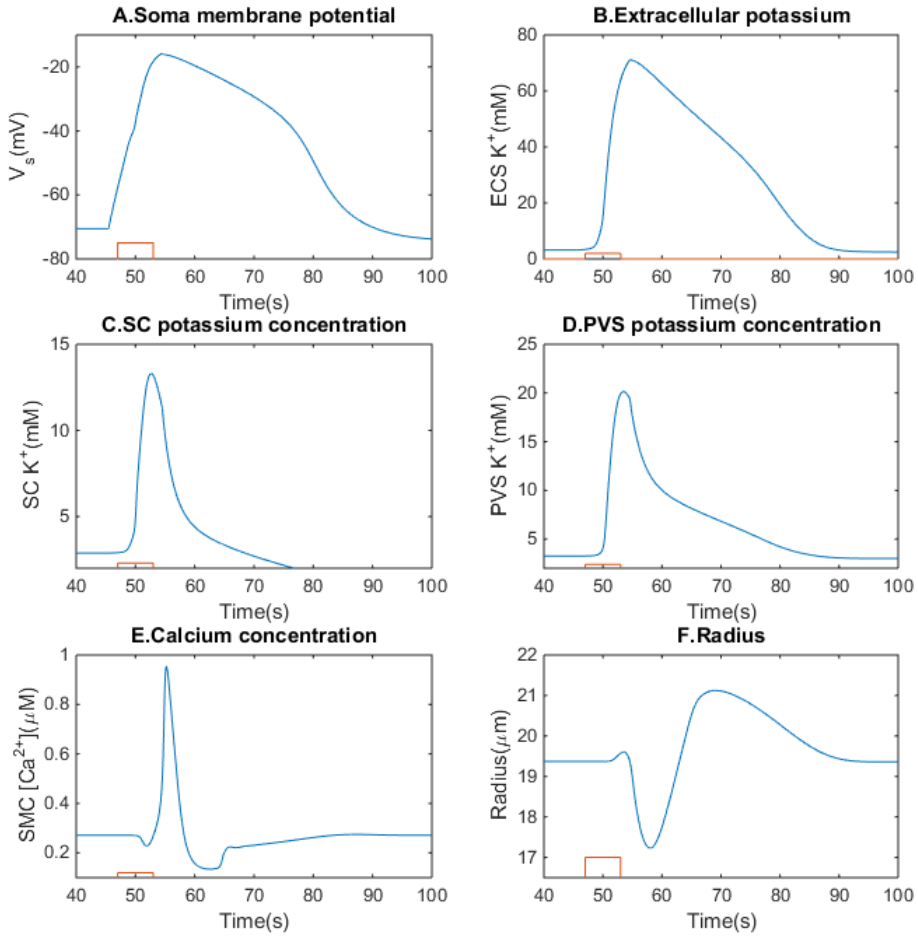

Fig. 4.3 Soma of the neuron model without the NaT channel is stimulated with a current intensity 1.425×10^{-3}mA/cm^2 in rectangular form for 9s causing constriction followed by dilation.

4.4.2 Vascular response for coupling with CSD neuron model with NaT channel

To examine the effects of CSD neuron model with NaT channel on the vasculature, a depolarizing current of intensity 8×10^{-4}mA/cm^2 in rectangular form is applied to cell soma

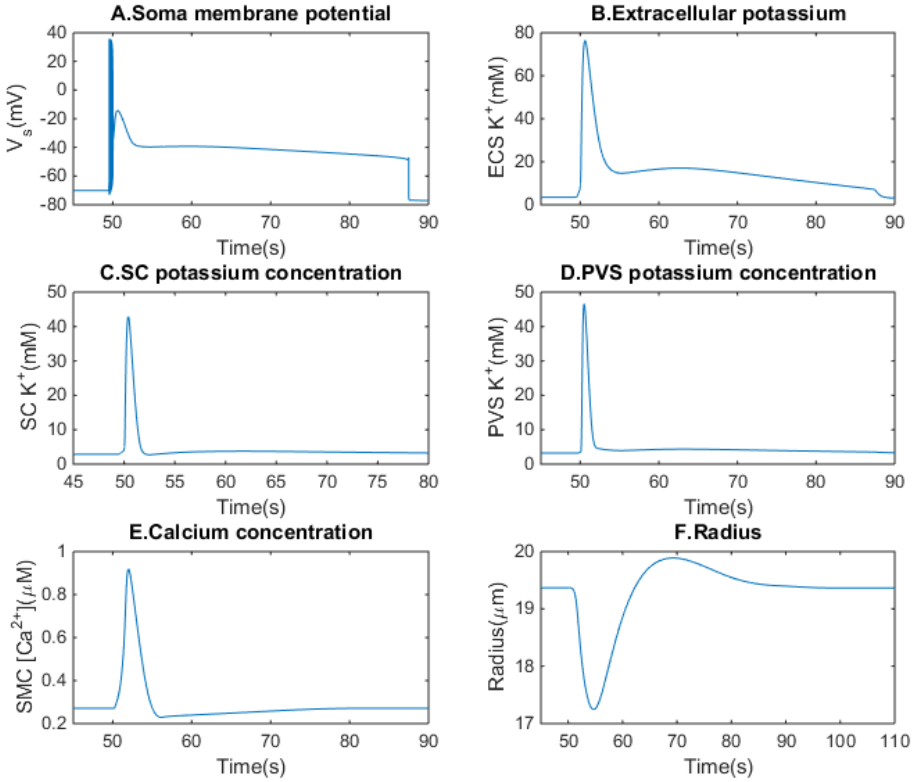

Fig. 4.4 Vascular response during cortical spreading depression of the neuron model with NaT channel. A fraction of extracellular potassium that goes into the synaptic cleft induces contraction through the K^+ signalling mechanism. The soma is then stimulated with a current in rectangular form with intensity 8×10^{-4}mA/cm^2 for 1s.

for 1s and it evoked CSD. As the high extracellular potassium efflux causes the astrocyte to depolarize (Figure 4.4B, 4.4C), the BK channels open leading to an influx of high amount of K^+ ions in the perivascular space (Figure 4.4D). This causes depolarization of the SMC due to the action of the inwardly rectifying potassium channel [24] with consequential increase in calcium concentration (Figure 4.4E) and vessel constriction (Figure 4.4F).

To find the effects of coupling the neuron model to the vasculature, the model output was compared to the neuron model which is uncoupled to the vasculature. Figure 4.5A, 4.5B shows the membrane potential and the ECS potassium changes during the coupled and uncoupled states. When the neuron model is coupled, the number of spikes generated at first does not change but the duration of the CSD increases. This is due to the constriction caused during CSD which decreases the strength of the Na^+/K^+ ATPase exchange pump. To examine the effects of stimulus conditions on CSD, the stimulus was increased by 50% of its

original value. Figure 4.5C, 4.5D shows the effects of stimulus on CSD. As the stimulus is increased the number of spikes generated decreases and the stimulus amplitude is high and the duration of the CSD also decreases.

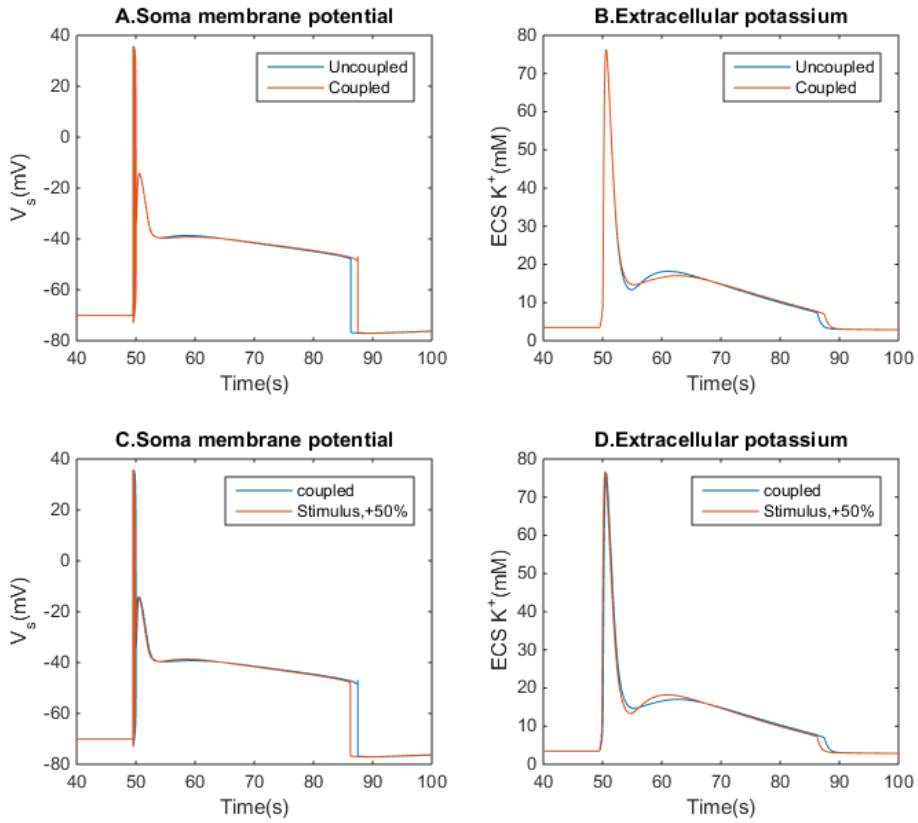

Fig. 4.5 Difference in CSD after coupling to the vasculature and difference in CSD after increasing the stimulus. A,B shows CSD before and after coupling to the vasculature. C,D shows CSD variations for 50% increase in stimulus intensity and duration.

4.4.3 Vascular response during normal neural activity

To regulate the extracellular potassium in the physiological range, the maximum pumping rate is increased to 4 times of the original value and the soma of the neuron is stimulated with a depolarizing current of 8×10^{-3}mA/cm^2 in rectangular form for 10s, the neuron fires (Figure 4.6A) as long as the stimulus exists with corresponding change in extracellular ion concentrations. This increase in extracellular potassium in the physiological range also leads to vasodilation through the K^+ mechanism. The scaling factor k was chosen to be 9 in all

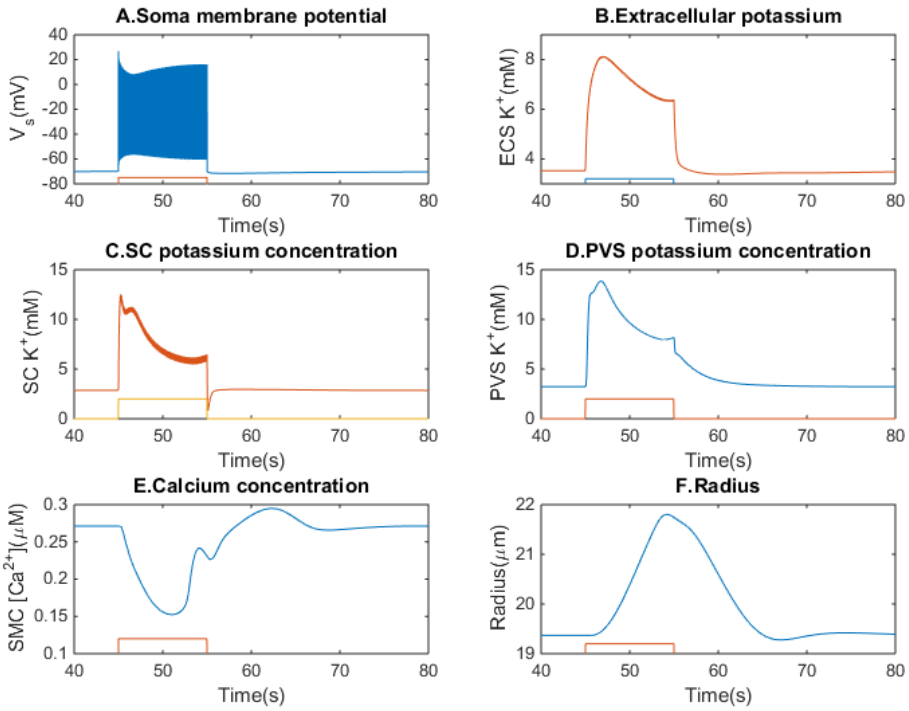

Fig. 4.6 Maximum pumping rate is increased to 4 times of the original value to regulate extracellular potassium concentration and the soma of the neuron is stimulated with a depolarizing current of $0.014 mA/cm^2$ in rectangular form for 10s. A 12.53% increase in radius change is observed for ECS potassium concentration change between 3.5-9mM.

the normal spiking and bursting simulations as this produced maximum dilation. A 12.53% increase in radius change (Figure 4.6F) is observed for ECS potassium concentration change between 3.5-9mM (Figure 4.6B).

4.4.4 Vascular changes as the coupling between neuron and astrocyte is varied

With the maximum pumping rate set to 4 times of the original value and same stimulus condition as above, the coupling between the neuron and the astrocyte is varied by changing the value of k in the estimated physiological range. Figure 4.7 shows the responses of the vasculature for different potassium concentration changes in the synaptic cleft. For values less than or equal to 9, the model gave dilatory response and for values greater than that, the

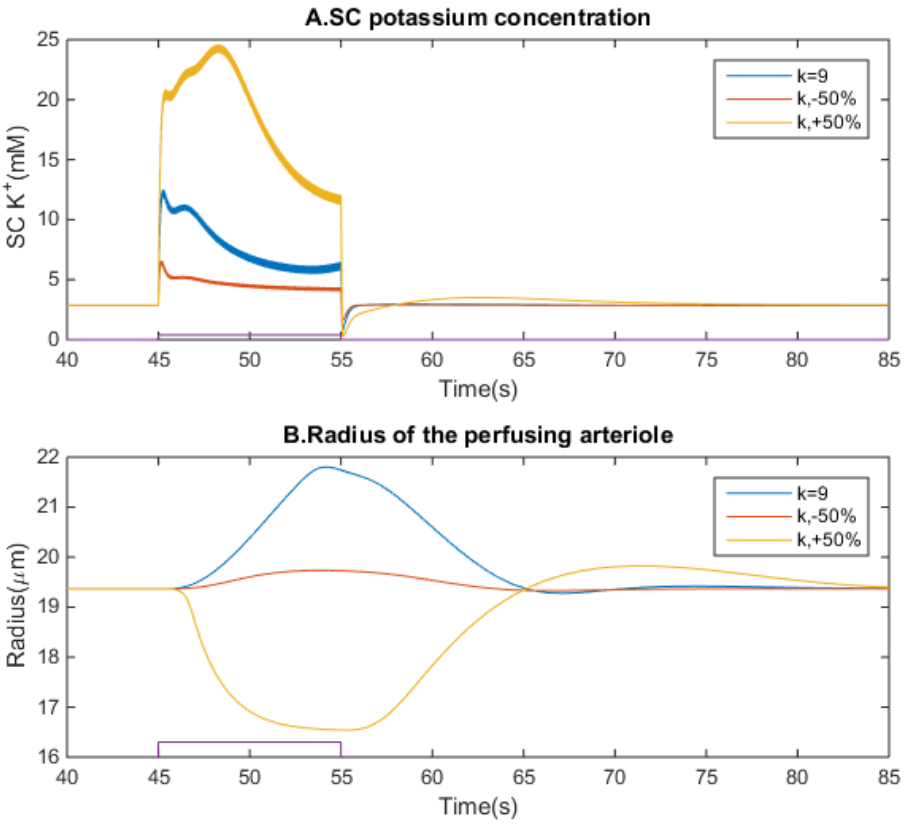

Fig. 4.7 Effects of changing the paramter k on the synaptic potassium concentration and the vascular response. The soma of the neuron is stimulated with a depolarizing current of $0.014 mA/cm^2$ in rectangular form for 10s in all the simulations.

model generated constriction followed by dilation.

4.4.5 Vascular response for neural bursting

With the same magnitude of stimulus current to the soma and the same duration, Imax in increased to 5 times of the original value to observe the vascular response during bursting. The extracellular potassium changes for the first burst was between 3.5-6.5mM with subsequent bursts generating ionic oscillations between 4.5-5.5mM ((Figure 4.8A, 4.8B). This induced only 4.74% increase in radius of the artery.

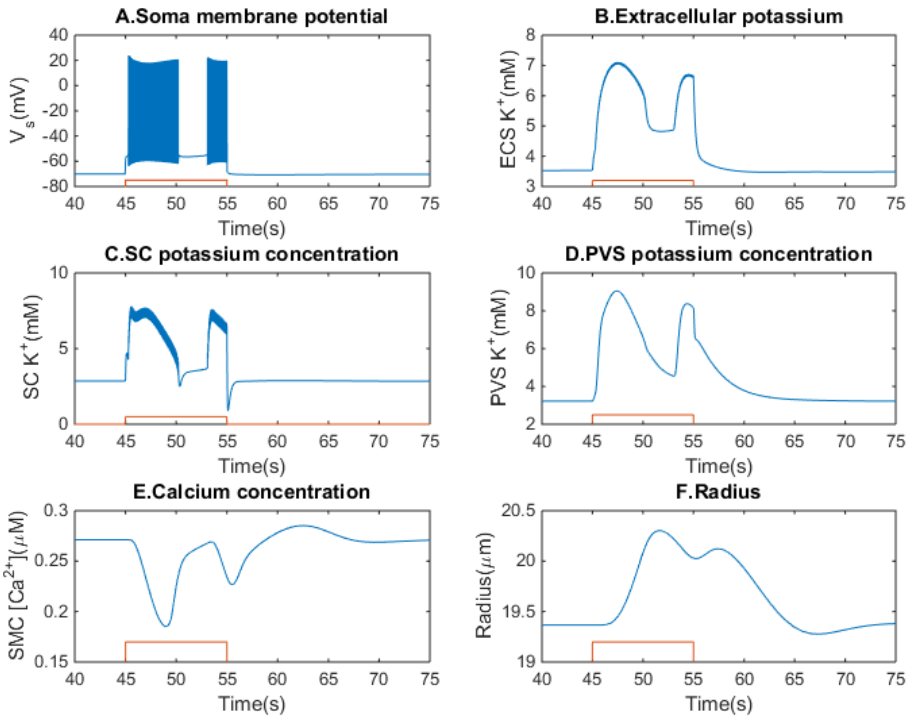

Fig. 4.8 Vascular response during bursting. Only 4.74% increase in radius is observed as the ECS potassium oscillates between 3.5-6.5mM. The soma of the neuron is stimulated with a depolarizing current of $0.012 mA/cm^2$ in rectangular form for 10s.

4.5 Discussion

In this chapter, the results obtained by coupling the neuron, astrocyte and vasculature model are presented. The proposed coupling method includes the essential dynamics of neural activity leading to vascular response through K^+ signalling mechanism and the resultant increase in oxygenation nourishing the neuron. Different neuronal behaviours evoked distinct vascular responses. The vascular response acts as feedback by either enhancing the pumping rate through dilation or weakening the pumping rate through constriction. This interaction between the neurovascular system comprising the neuron,astrocyte and vasculature is always active during any computation in the brain. Hence the models of networks in the brain must take into account the effects introduced by neurovascular response. In addition to this, astrocytes [87] and the Na^+/K^+ ATPase exchange pump [30] are found to be information processing units which again emphasizes the need to include these in any network level models.

A elevation of extracellular potassium in the physiological range is found to induce vasodi-

lation in a number of studies [32], [28]. The current model prediction also suggests the definite role of astrocyte in cerebrovascular regulation activated through elevated extracellular potassium concentrations. Even though some studies have found that neurovascular coupling operates independent of oxygenation changes [66] ,the model results suggests that oxygen has a role to play in neurovascular coupling atleast indirectly by regulating the pump activity, thereby regulating the activity of astrocyte. This was also suggested by a recent experiment which found that during neural activity the tissue oxygen concentration affects how the astrocytes control the vascular response [34].

The neurovascular coupling mechanism is altered in a wide range of neurological diseases such as hypertension, stroke, Alzheimer disease and cortical spreading depression [33]. Hypoxic conditions are also known to affect the activities of the neurons and hence also affects the neurovascular coupling mechanism. Hypoxia also alters the propagation and recovery from cortical spreading depression [16]. The neuron model based on Chang et al and Kager et al generates hypoxia by inducing vasoconstriction. Hypoxic conditions can also be induced in the model by either interrupting the pump activity or by increasing the fraction of oxygen consumed by the pumpθ in equation 4.8. As it is a compartmentalized model it allows for replacing the model components (neuron,astrocyte and vasculature) with a different set of hypotheses and hence can be used to study different pathological conditions. The vascular response during bursting decreased compared to normal neural activity as it did not produce enough potassium in teh extracellular space. This was observed in the experiment done by Kreisman et al [59] showing low oxygenation during seizures. Especially they observed an initial increase in cerebral blood flow followed by a decrease in cerebral blood flow similar to what we observed in our simulations (Figure 4.8).

We have assumed that the functions of the brain activity other than action potential generation and restoration of ionic gradients remains constant during activation. However brain activity also involves other kinds of cellular activities such as synaptic activity and glial activity. These activities can communicate with the vasculature through a multitude of vasoactive factors, for example nitric oxide (NO), adenosine, hydrogen ions (H^+), glutamate, arachidonic acid derivatives and purines [5]. Filosa et al[28], based on their experimental work suggested that when these mechanisms coexist upon brain activity, they interact in a particular way to produce different responses of vessel tone. In spite of the mounting evidence for vasoactive factors released during neural activity, the temporal and spatial conditions determining their release and their combined effect on the vasculature remain to be understood. Hence modelling different neural activities and their associated mechanisms that can vary blood flow, based on experimental data can shed light on the dynamics at play.

4.6 Conclusions

The coupling made between the neuron and the astrocyte leads to the vascular response whereas the coupling made between the neuron and the vasculature provides the energy to the neuron to continue its function. When CSD is induced in neuron model based on Chang et al with a certain stimulus the radius increased by 25.9% and when CSD is induced in the neuron model based on both Kager et al, the radius decreased by 11.5%. However if the stimulus intensity is increased by twice the original value in the neuron model based on Chang et al, it also induced vessel constriction. The percentage increase in radius change induced by the continuously spiking neuron model was 12.53% and that of bursting neuron model was only 4.74%. These vascular responses had their corresponding effects on the tissue oxygenation and thereby an effect on the functioning of the sodium potassium exchange pump.

Chapter 5

Model of fMRI BOLD response

5.1 Introduction

The BOLD signal model is based on the work of Buxton et al [12] and the BOLD response is determined by the neurovascular and neurometabolic responses. The BOLD response depends on the changes in cerebral blood flow, cerebral metabolic rate of oxygen consumption and cerebral blood volume. Based on the experimental finding that in many brain areas CBF increases 2-3 times more than the $CMRO_2$, decreasing the oxygen extraction fraction [31, 47], Buxton et al simulated the BOLD response. The model simulates the experimentally observed BOLD signal transients such as the initial dip, positive or negative BOLD and the post stimulus undershoot. One of the assumptions of the Buxton et al's model was that $CMRO_2$ response was a function of CBF response. This is not the case in reality as the $CMRO_2$ can vary independently of the CBF response. The presented model overcomes this limitation and uses Buxton et al's model to simulate the BOLD signal with the normalized CBF and $CMRO_2$ profiles derived from the neurovascular and neurometabolic coupling models.

5.2 The BOLD model

The BOLD model of Buxton et al[12] considers the vascular component within a certain volume of tissue as an expandable balloon (venous compartment) and describes the non dimensionalized deoxyhemoglobin concentration, $q(t)$, and cerebral blood volume, $v(t)$, by mass conservation equations given by

$$\frac{\mathrm{d}q}{\mathrm{d}t} = \frac{1}{\tau_{MTT}}\left(\frac{M}{M_0} - \frac{q(t)}{v(t)} f_{out}(v,t)\right) \tag{5.1}$$

$$\frac{dv}{dt} = \frac{1}{(\tau_{MTT} + \tau)} \left(\frac{B}{B_0} - v^{\frac{1}{d}} \right) \tag{5.2}$$

where M is the $CMRO_2$ response, M_0 is the equilibrium value of $CMRO_2$, B is the cerebral blood flow as defined in equation 4.7 in chapter 4. Here τ_{MTT} is the mean transit time defined as the time a specified volume of blood spends in the capillary circulation. The mean transit time is assumed to be constant and is estimated by the ratio between the resting venous volume fraction and steady state blood flow. The time-dependent outflow from the venous compartment which is transiently different from cerebral blood flow is given by

$$f_{out}(v) = v^{\frac{1}{d}} + \tau \frac{dv}{dt} \tag{5.3}$$

here d gives an empirical relationship between blood flow and volume. This equation describes the transients which occur in the venous compartment such as viscoelastic effects wherein the blood vessel initially resists a change in volume, but eventually settles into a new resting value according to the empirical relationship between the cerebral blood flow and cerebral blood volume. The transient adjustment required is controlled by the time constant τ. The net extraction fraction of oxygen($E(t)$) is given by

$$E(t) = \frac{ME_0}{B} \tag{5.4}$$

E_0 is the steady state value of the extraction fraction of oxygen. The BOLD signal change from its steady state value is a linear combination of blood flow and venous volume so that

$$\Delta BOLD \approx V_0[a_1(1-q) - a_2(1-v)] \tag{5.5}$$

where V_0 is the resting venous blood volume fraction of the tissue voxel, $a_1 = 3.4$ and $a_2 = 1.0$ are dimensionless parameters based on several experimental and physiological parameters. The values used here are taken from the experimental work of Obata et al[76]. $CMRO_2$ (M) is the oxygen consumed by the neuron given by

$$M = B_0 P([O_2])(1-\theta) + C_p \tag{5.6}$$

where C_p is given in equation 4.9. This equation describes that the cerebral metabolic rate of oxygen is given by the sum of the consumption of oxygen by the pump and the other active processes.

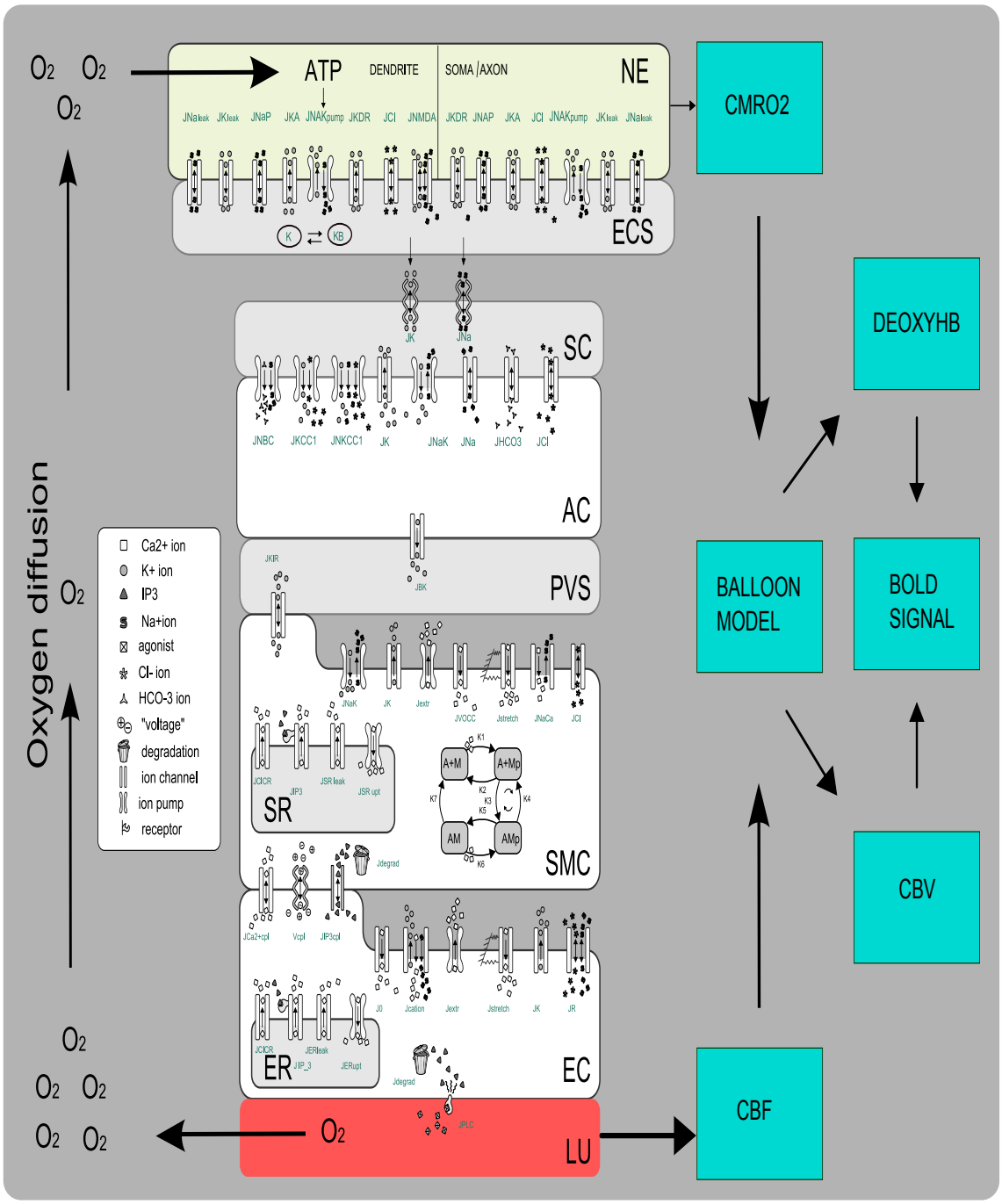

Fig. 5.1 Neurovascular system integrated with the fMRI BOLD model. The neurovascular and neurometabolic responses are used as an input to the balloon model to simulate the BOLD signal.

Table 5.1 Parameter values of the BOLD signal model, from Buxton et al[12]

Parameters	Values	Units	Description
τ_{MTT}	3	s	mean transit time
E_0	0.4	–	initial value of oxygen extraction fraction
V_0	0.03	–	resting venous blood volume fraction
d	0.4	–	parameter giving empirical relation between CBF and CBV
τ	20	s	parameter which alters the transient relationship between CBF and CBV

5.3 Results

In this chapter, the neurovascular system as described in chapter 3 and 4 is integrated with the BOLD model to simulate the BOLD response. The BOLD response for different kinds of neural activity is presented and discussed. The parameters that can determine the BOLD signal transients such as the initial dip and post stimulus undershoot are illustrated.

5.3.1 Blood supply, consumption and oxygen extraction fraction

The neural activation and its consumption of oxygen provides a $CMRO_2$ response while the neurovascular coupling mechanism initiated by the neural activation gives the CBF response. At rest, the CBF and $CMRO_2$ are tightly coupled with a relatively uniform oxygen extraction fraction [38]. However, during neural activation there is a phase lag between them. The ratio of the fractional change of CBF to the fractional change in $CMRO_2$ during activation is the physical basis for the BOLD signal. If the CBF increases more than $CMRO_2$ during neural activation, the oxygen extraction fraction will decrease and it will increase when the $CMRO_2$ increases more than CBF. To investigate this phenomenon we simulated the model with two different parameter sets which will result in the above mentioned scenarios. In all the simulations, the parameter k which is the scaling factor to account for the volume difference between the extracellular space and synaptic space is assumed a value of 9 as it generates maximum dilation unless stated otherwise. For the parameter set mentioned in chapters 3,4,5, and increasing the I_{max} value to 400% of its original value to tightly regulate the extracellular ionic concentrations, stimulating the neuronal soma with a current stimulus in rectangular form with amplitude 0.014 mA/cm^2 and 10 s duration decreases the oxygen extraction fraction. This parameter set is considered as the standard response here. The scenario where the $CMRO_2$ increase is greater than CBF increase, increasing the oxygen extraction fraction is simulated by changing the value of the parameter k to 5 and increasing the fractional consumption of oxygen by the Na^+/K^+ ATPase pump (θ) to 0.30. Figure 5.2

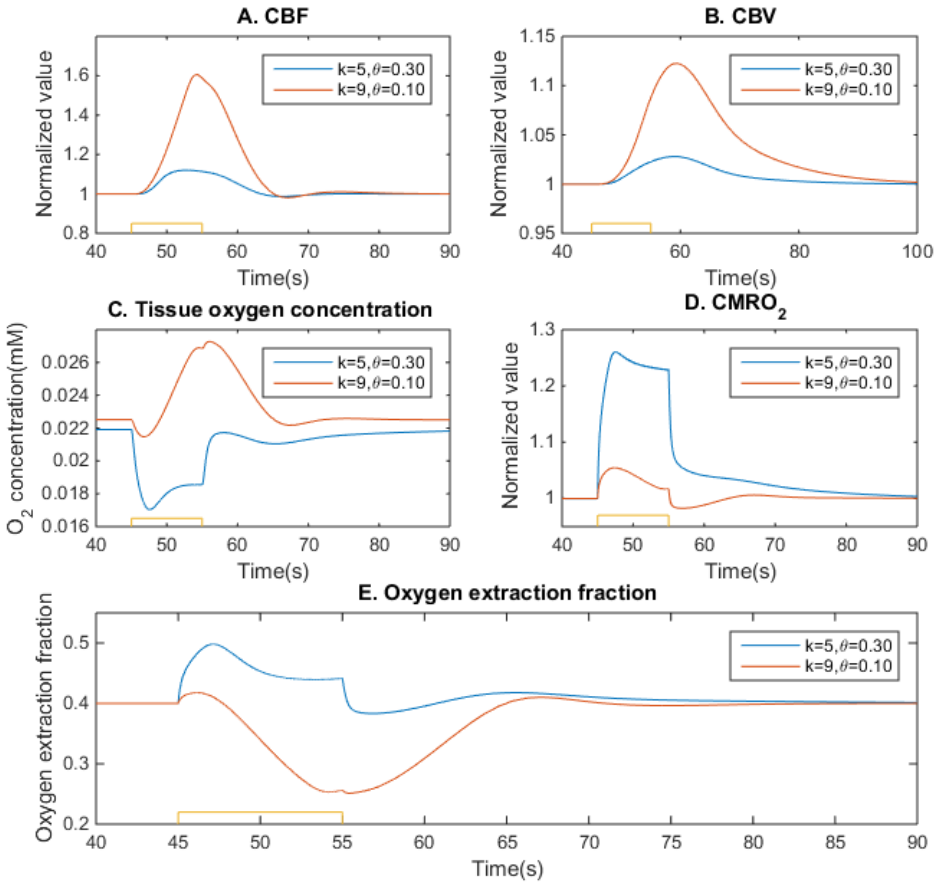

Fig. 5.2 Relative change of CBF to $CMRO_2$ determining the oxygen extraction fraction. The soma of the neuron is stimulated with a depolarizing current of $0.014 mA/cm^2$ in rectangular form for 10s in all the simulations. Using two different parameter sets, the variations in oxygen extraction fraction is illustrated. The parameter set k=9,θ=0.10 decreases the oxygen extraction fraction while the the parameter set k=5,θ=0.30 increases the oxygen extraction fraction.

illustrates how different profiles of CBF and $CMRO_2$ results in distinct oxygen extraction profiles. Figure 5.2A, 5.2B shows the normalized temporal evolution of CBF and CBV. The CBF peak increases to about 60% for the standard parameter set while only 12% CBF peak increase was observed for the second parameter set. The CBV increases as a consequence of the increase in CBF following the empirical relationship between them. The $CMRO_2$ increases as soon as the neuron becomes active (Figure 5.2D) and CBF increases with a delay to that of the $CMRO_2$ response. For the standard parameter set the $CMRO_2$ peak increases to about 5% and for the second parameter set it increases to about 26%. While the 60%

CBF peak increase and 5% $CMRO_2$ peak increase for the standard parameter set increases the tissue oxygen concentration (Figure 5.2c), it decreases the oxygen extraction fraction (Figure 5.2E). On the contrary, for the second parameter set, the 12% CBF peak increase and 26% $CMRO_2$ peak increase decreases the tissue oxygen concentration (Figure 5.2c) increasing the oxygen extraction fraction (Figure 5.2E).

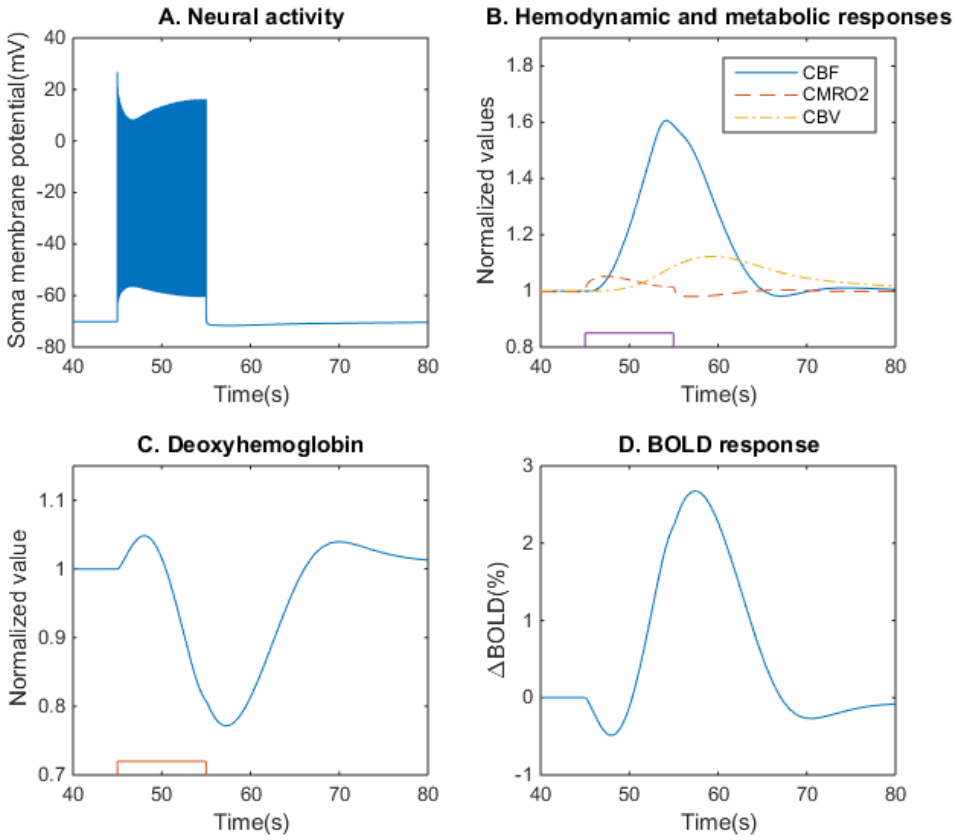

Fig. 5.3 CBF, CBV and $CMRO_2$ determining the deoxyhemoglobin content and consequently the BOLD signal. The soma of the neuron is stimulated with a depolarizing current of $0.014 mA/cm^2$ in rectangular form for 10s.

5.3.2 BOLD signal during normal neural activity

Figure 5.3 shows the profiles of CBF, CBV and $CMRO_2$ determining the deoxyhemoglobin content and consequently the BOLD signal for the same standard stimulus conditions as above . The high fractional increase of CBF to $CMRO_2$ decreases the oxygen extraction fraction which in turn decreases the measured deoxyhaemoglobin content (Figure 5.3C) in

the tissue MRI voxel. This decrease in deoxyhemoglobin in the tissue voxel results in a positive BOLD signal(Figure 5.3D). In the model, for low values of θ the relative change of CBF to $CMRO_2$ matches the experimental observation in different brain areas where CBF increases more than that of $CMRO_2$ [47]. However as θ is increased to about 0.50, the $CMRO_2$ increases more than CBF indicating high neural activity. This matches the experimental observation in the hippocampus that the BOLD signal is either slightly positive or negative [85] indicating high neural activity or/and low vascular response.

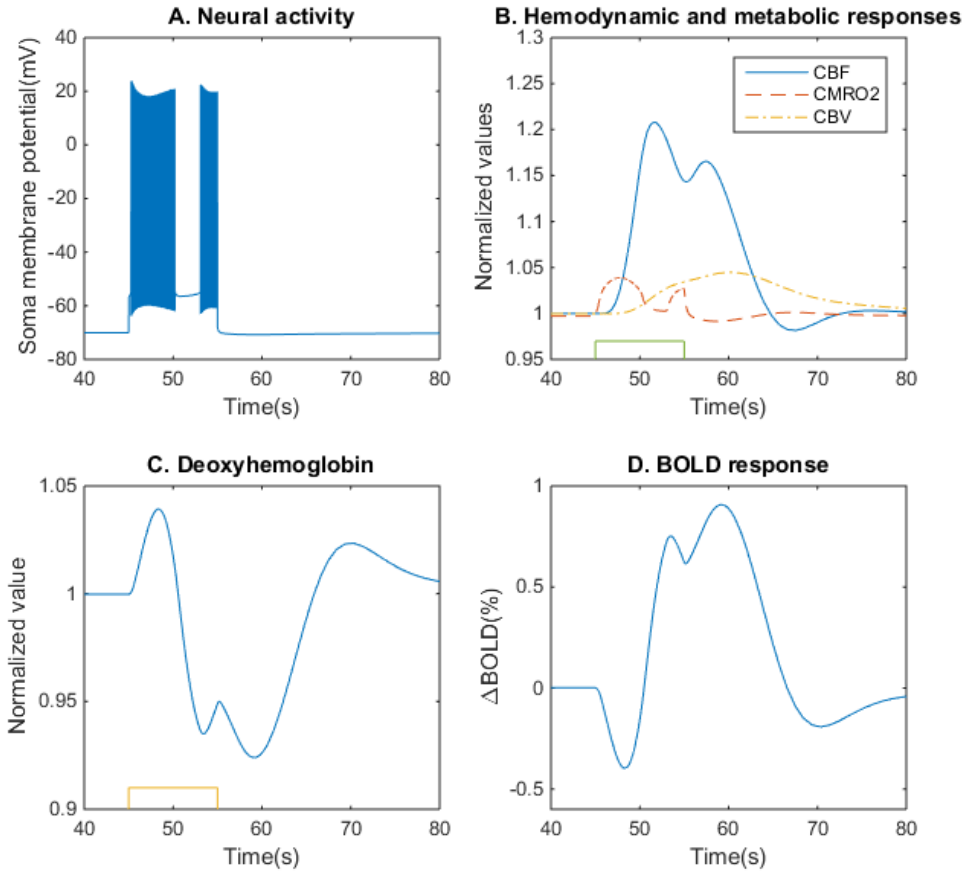

Fig. 5.4 CBF, CBV and $CMRO_2$ determining the deoxyhemoglobin content and consequently the BOLD signal. The soma of the neuron is stimulated with a depolarizing current of $0.012 mA/cm^2$ in rectangular form for 10s.

5.3.3 BOLD signal for bursting in the neuron

Figure 5.4 shows the BOLD response for bursting conditions in the neuron. The bursting condition is simulated for the same parameter set above except that it is stimulated by delivering a sub threshold current to the neuron in rectangular form with amplitude $0.012 mA/cm^2$ and 10 s duration. The bursting (Figure 5.4A) induces 20% CBF peak increase(Figure 5.4B) and 3.9% $CMRO_2$ peak increase. The CBF increases more than $CMRO_2$, decreasing the deoxyhemoglobin content (Figure 5.4C) and consequently generating a positive BOLD response (Figure 5.4D).

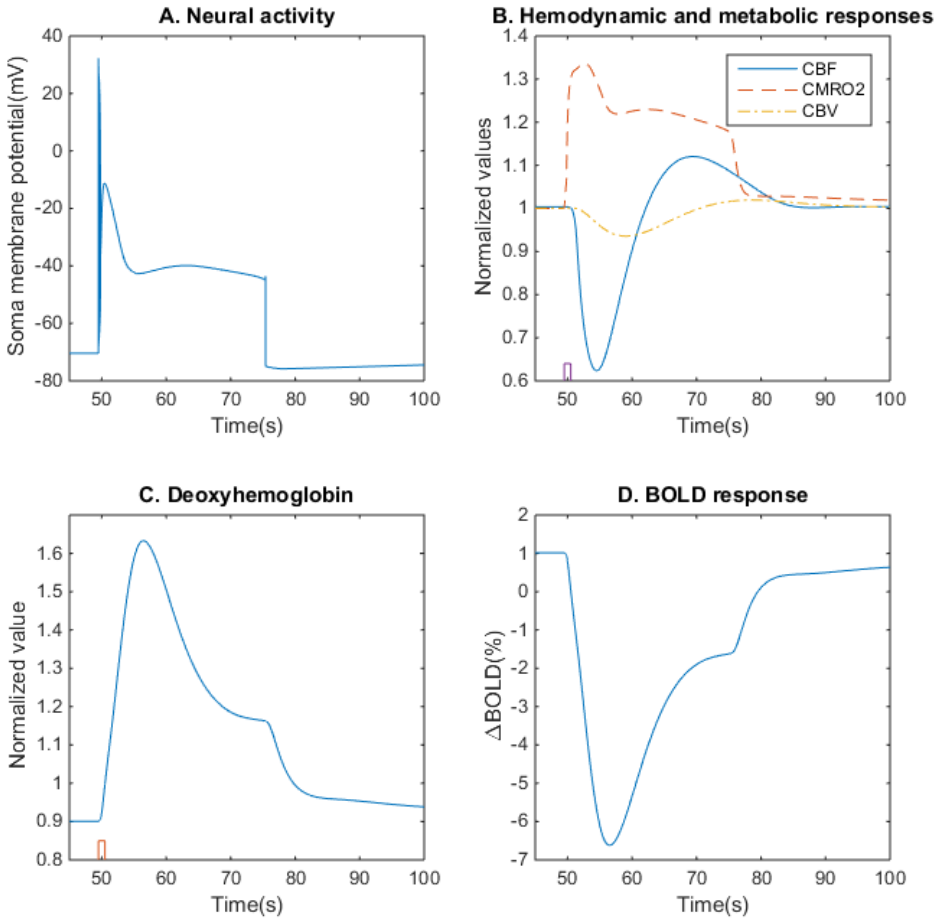

Fig. 5.5 A large negative BOLD response is observed during CSD due to vascoconstriction and a large ionic increase in the ECS

5.3.4 BOLD signal during CSD

Figure 5.5 shows the BOLD response during CSD. When the soma of the neuron model is simulated with the standard parameter set with a stimulus current in rectangular form with amplitude $0.006 mA/cm^2$ and 1 s duration, CSD is generated (Figure 5.5A). During CSD the high ECS potassium increase leads to vasconstriction through the K^+ signalling mechanism reflected in the CBF response (Figure 5.5B). Due to the high rise in ECS potassium, the Na^+/K^+ ATPase pump becomes very active and leads to high $CMRO_2$ (Figure 5.5B). The $CMRO_2$ increases more than CBF and a large negative BOLD response is observed (Figure 5.5D). In an experiment done in the visual cortex exhibiting cortical spreading depression [39], the positive BOLD signal was observed at first and they diminished after a while indicating vasoconstriction following vasodilation giving large negative BOLD signals.

5.3.5 Effects of high $CMRO_2$ on the BOLD signal

For the same stimulus conditions as that of continuous spiking, we varied the fractional consumption of oxygen by the Na^+/K^+ ATPase pump (θ) to investigate its effects on the BOLD response. The initial dip sometimes observed in the BOLD response [91] is essentially due to the phase lag between the CBF and $CMRO_2$. When the parameter θ is increased to 0.30 (Figure 5.6A), the $CMRO_2$ increases and the phase lag becomes more apparent and can be seen as an reduction in tissue oxygen concentration (Figure 5.6B) and increase in the initial dip of the BOLD response(Figure 5.6F). When the parameter θ is increased to 0.50 (Figure 5.6A) the changes in the BOLD response is drastic and negative (Figure 5.6F). The high $CMRO_2$ decreases the tissue oxygen concentration (Figure 5.6B) to a point where it decreases the action of the Na^+/K^+ ATPase pump in the neuron which leads to an increase in ECS potassium concentration (Figure 5.6C) outside the physiological range (4-8 mM). This leads to vasoconstriction (Figure 5.6D) which decreases CBF (Figure 5.6E). Now increase in $CMRO_2$ and the decrease in CBF gives rise to a large negative BOLD response (Figure 5.6F).

5.3.6 Post stimulus undershoot variations in the BOLD response

The post stimulus undershoot often observed in the BOLD response is debated even today of its origins [18]. The post stimulus undershoot is thought to arise due to two possible physiological scenarios. One where it arises from the effects of venous compliance and another where neural activity is sustained beyond the blood flow response or the neural

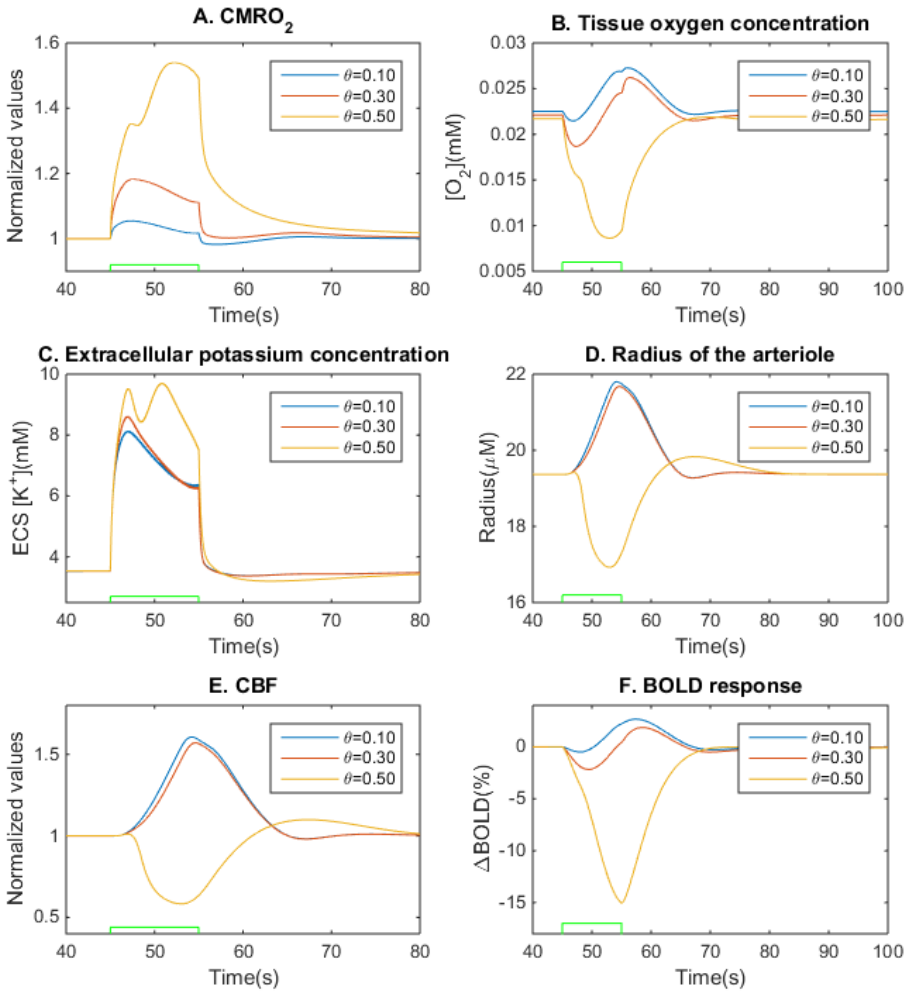

Fig. 5.6 Moderate increases in $CMRO_2$ causes initial dip and high increase lead to a large negative BOLD signal. The soma of the neuron is stimulated with a depolarizing current of $0.012 mA/cm^2$ in rectangular form for 10s in all the simulations.

activity is very high that the blood flow response is insufficient to cater its oxygen needs. When the parameter τ which controls the effects of venous compliance in the model is set to zero in equation (5.2), the post stimulus undershoot depends only on the effects of neural activity. Figure 5.7 illustrates how $CMRO_2$ that rises above the cerebral blood volume at $\tau = 0$ after the end of stimulus can independently cause post stimulus undershoot. Figure 5.7A, 5.7B shows how the post stimulus undershoot vanishes for $\tau = 0$ and $\theta = 0.10$. Here venous compliance effects is absent and the $CMRO_2$ is not large enough and long enough to cause post stimulus undershoot. Figure 5.7A, 5.7B shows how long and high $CMRO_2$ for

$\theta = 0.40$ can cause post stimulus undershoot independent of the vascular compliance effect. When the effect of venous compliance exists along with neural activity the effects on post stimulus undershoot is additive.

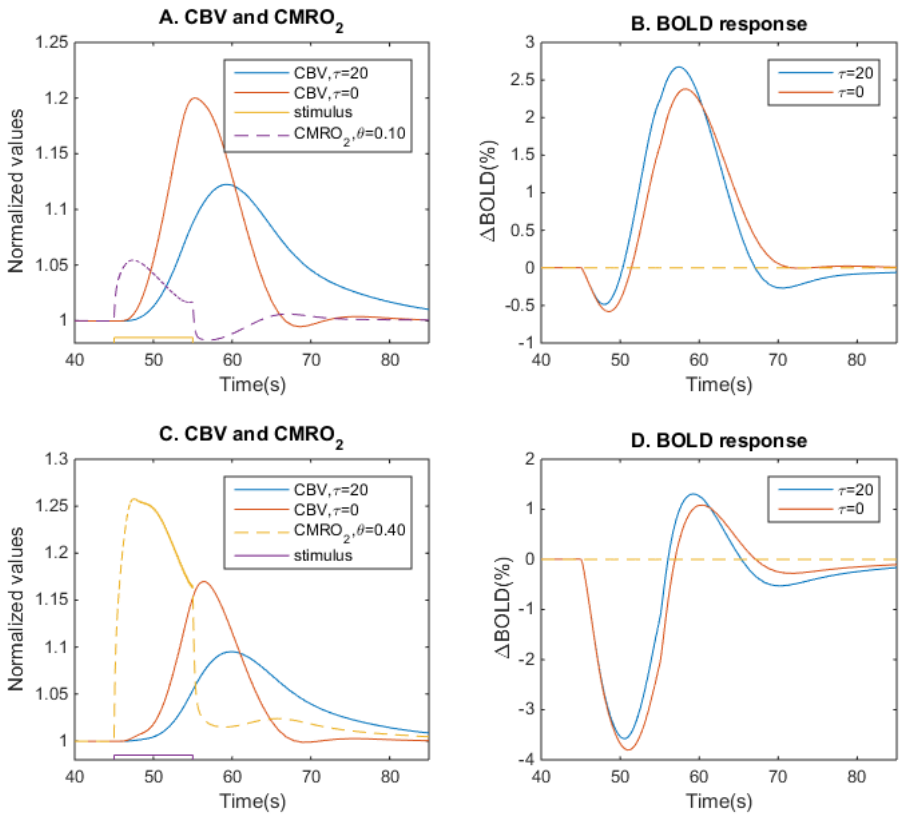

Fig. 5.7 Post stimulus variations due to neural activity and venous compliance. The soma of the neuron is stimulated with a depolarizing current of $0.012 mA/cm^2$ in rectangular form for 10s in all the simulations. Even when $\tau = 0$ we can still observe (Figure 5.7B) an undershoot due to high neural activity (Figure 5.7C)

5.4 Discussions

Using combined modelling of both neurovascular and BOLD responses, we show the different variations in the BOLD signal associated with changes in neuronal, hemodynamic, and metabolic activity. The model can show experimentally observed attributes of the BOLD signal such as the initial dip, positive BOLD, negative BOLD and post stimulus undershoot. Neural activity and their consumption of oxygen utilising ATP plays an important role in

the dynamics of the measured BOLD signal. Different cellular activities in the brain such as maintaining the resting potential, action potential generation, glial activity, pre-synaptic and post-synaptic activities consume different percentages of the total nutrient consumption. Energy costs per signalling event of these activities have been estimated in the brain by summing the ATP consumed by different processes involved [6]. According to these estimates, the processes involved in maintaining resting potential consumes 2%, action potential generation 10%, glial activities 2%, pre-synaptic activities 7% and post-synaptic processes consumes the highest of all which is 75 % of the total energy consumption. The post-synaptic activities involve restoration of ionic gradients and repackaging of the released neurotransmitters into vesicles. This energy budget must be specific to the kind of neural processing happening underneath as a specific task will require different sets of activated neurons or the same neurons activated in a different way. In the model the Na^+/K^+ ATPase pump is assumed to be the only active consumer of oxygen during neural activation and it is estimated to consume 40-50 % of the total oxygen consumption during bain activity [2]. Variations in this percentage of oxygen consumption by the Na^+/K^+ ATPase pump leads to distinct BOLD responses. The importance of the fractional consumption stems from the experimental observation [26] that the same neuron can be stimulated by distinct neural circuits to give different neuronal responses which changes the fractional consumption of active processes.

When CBF increases more than $CMRO_2$, the model gives a positive BOLD signal. In most regions this ratio takes a value between 2 to 4 [64]. A simple explanation of the reason for the high CBF to $CMRO_2$ ratio is that high arterial oxygen concentration might be required for oxygen to diffuse from capillaries to the mitochondria down a concentration gradient from high concentration in the capillary to a lower concentration in the tissue. Another plausible explanation is the oxygen limitation model [11] which is based on the idea that oxygen delivery to the tissue is limited at rest and hence the only way to increase the already limited tissue oxygen is to increase the CBF and facilitate diffusion down the concentration gradient from capillary to tissue. In some brain regions of the cortex the ratio of CBF to $CMRO_2$ is found to be less than unity [36] and in the hippocampus the ratio is less than two in most experiments [81].

Occurrence of an initial dip in the BOLD response is debated for long as many experiments did not observe it [48]. A recent experiment investigating the dependence of initial dip, positive BOLD and the post stimulus undershoot on cortical depth with a 7 T scanner [91] on human subjects found that initial dip and post stimulus undershoot occurred in all the regions examined. They found that the magnitude of the initial dip observed increased with stimulus duration and decreased with cortical depth. The 7 T MRI scanner used in this particular

experiment has high temporal resolution (0.6 s) and hence the dynamics of initial dip which occurs immediately after the neuron becomes active is observed. Most experiments are performed at a scanner strength of 1.5-3 T which has a much lower temporal resolution (2-3 s) and hence could miss the initial dip. This suggests that the initial dip is likely to be present in other regions as well as it is essentially a indicator of increase in neural activity before the CBF response. In the model, increases in $CMRO_2$ increases the magnitude of initial dip observed (Figure 5.6).

The negative BOLD signal change observed in the experiments is very important as it can provide information on disordered conditions such as hypoxia. The negative BOLD response can be explained under three experimental scenarios. A high neural activity can cause the $CMRO_2$ to increase more than CBF and generate a negative BOLD response. This was observed in experiments done in the hippocampus [85] where even though the CBF response was high, a negative BOLD response was observed due to $CMRO_2$ response rising above the CBF response. A low neural activity has also been reported to result in a negative BOLD response [89] in the monkey visual area. A low neural activity could mean that not enough vasoactive factors are released to evoke a CBF response and hence the CBF will stay in its resting state while the $CMRO_2$ response increases depending on amount of neural activity. An induced apnea condition can also result in a negative BOLD signal. Kannurpatti et al [57] found in their experiment that hypoxia induced negative BOLD responses in hippocampus, thalamus, cerebral cortex, and third ventricle [57] with the amplitude of BOLD signal in the hippocampus being the least. Our model result (Figure 5.6) showing the transition from initial dip to negative BOLD response illustrates the mechanism behind the hypoxia induced negative BOLD response with the assumption that hypoxia leads to increased fractional consumption of oxygen by the Na^+/K^+ ATPase pump thereby decreasing the tissue oxygen concentration.

The post stimulus undershoot has two possible explanations. It can either be due to the delayed vascular compliance of the venous blood flow or due to the prolonged time taken for the Na^+/K^+ ATPase pump to restore ionic homeostasis [98]. Our results suggest that both the neural activity and venous compliance effects on the undershoot can coexist and contribute in an additive manner. The experiment done with the 7 T scanner on human subjects also supported the sustained neural activity hypothesis. They found that the post stimulus undershoot was maximum in deep cortical layers where a high density of neurons are present indicating high $CMRO_2$.

5.5 Conclusions

In this chapter we have presented the BOLD responses arising out of the neurovascular and neurometabolic responses for different neuronal behaviours. The relative change of CBF to $CMRO_2$ determines the magnitude of the BOLD signal and whether it is a positive or negative BOLD. The initial dip observed in the BOLD response is a consequence of the delay between the neural activity and the vascular response. The model suggests that both the delayed vascular compliance of the venous blood flow and the prolonged time taken for the Na^+/K^+ ATPase pump to restore ionic homeostasis can contribute to the post stimulus undershoot observed in the BOLD response. A large negative BOLD response was observed for CSD behaviour of the neuron due to the constrictory response of the vessel for high extracellular ionic changes. A negative also arises in the model for large increases in the fractional consumption of oxygen by the Na^+/K^+ ATPase pump. Also variations of any other parameter that drives the extracellular potassium out of the physiological range can also induce a negative BOLD response.

Chapter 6

Sensitivity analysis and comparison to experimental data

6.1 Introduction

It is widely acknowledged now that neurovascular coupling varies between areas with even similar neuronal populations [23] in the brain. This is also reflected in the BOLD responses in different regions and within the same regions. There could be a number of parameters that bring about this changes in different brain regions or within the same region. Hence in this chapter the variations in the vascular response and the BOLD response due to some of the important parameters in the model are illustrated. We compared the CBF response of the model to experimental data from the cortex for different stimulus paradigm. We also compared the simulated BOLD response during bursting conditions to seizure and hypoxic experimental data as bursting is known to be a characteristic of such disordered conditions.

6.2 Results

In this chapter we report the initial dip(first local minimum in the Δ BOLD signal), peak signal(global maximum in $|\Delta BOLD|$) and post-stimulus undershoot(last local minimum in Δ BOLD) for variation in different parameters. In some cases, there is no initial dip or post stimulus undershoot, in which case we report only the peak signal, which may be negative. During neural activation, with the parameter values given in chapters 3,4,5 and with stimulus amplitude of $0.014 mA/cm^2$ and duration of 10 s, the model generated an initial dip of -0.44, a maximum positive BOLD signal of 2.674 and a post stimulus undershoot of -0.26. The

parameters of the neuron model were decreased or increased from their original values in a physiologically relevant range or upto 50% and the resultant peaks of the BOLD signal from resting state are given in Table 6.1. If a physiological range is not available in the literature then the parameters are increased or decreased 50% of its original value to see the effects on the BOLD response. The stimulus duration is indicated on the x axis by a small rectangular box.

6.2.1 Effects of variations to the mean transit time and empirical relationship between flow and volume on the BOLD response

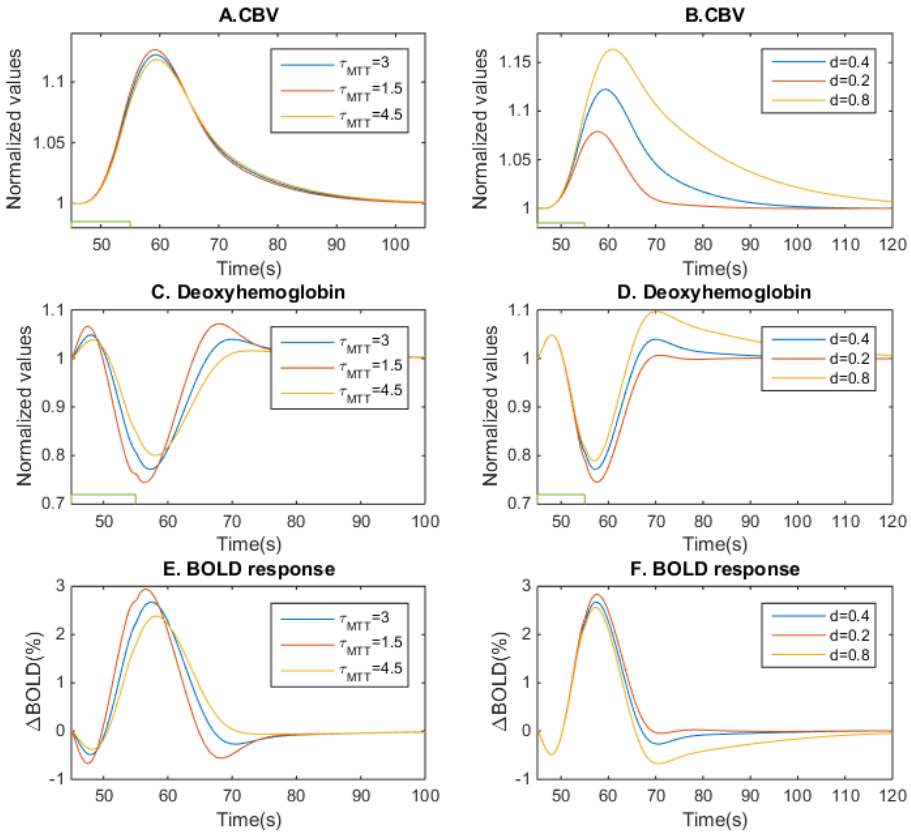

Fig. 6.1 CBV, deoxy-hemoglobin and BOLD responses to variations in mean transit time $1.5 \leq \tau_{MTT} \leq 4.5$ and power law exponent $0.2 \leq d \leq 0.8$ determining the relationship between CBF and CBV. A stimulus amplitude of $0.014 mA/cm^2$ and duration of 10 s was used in all the simulations.

The time a certain volume of blood spends in the capillary circulation is known to have an independent effect on the BOLD response [53]. It is likely to vary across different regions and is controlled by the parameter τ_{MTT} in the model. The Figure 6.1A, 6.1C, 6.1E shows the effects of mean transit time variations on the CBV, deoxyhemoglobin content and the BOLD response. When τ_{MTT} is decreased the blood volume slightly increases in magnitude (Figure 6.1A), the magnitude of the deoxyhemoglobin change also increases (Figure 6.1C). This consequentially gives an increase in the initial dip, positive BOLD and the post stimulus undershoot magnitude (Figure 6.1E). The parameter d that controls empirical relationship between blood flow and volume is varied in a physiologically observed range. Figure 6.1B, 6.1D, 6.1F shows the effects of parameter d variations on the CBV, deoxyhemoglobin content and the BOLD response. When d is decreased, the CBV decreases and deoxyhemoglobin decreases and consequently the positive BOLD response increases. While the initial dip remains the same, the post stimulus undershoot decreases. Increasing the value of d, decreases the positive BOLD and increases the post stimulus undershoot.

6.2.2 Effects of variations to the extracellular space volume, BK channel conductance and potassium ions buffering strength on the BOLD response

The effects of changing some of the important parameters that can affect the K^+ signalling mechanism are illustrated here. When the ECS volume is increased, it decreases the ECS potassium concentration (Figure 6.2A) and leads to a decrease in the magnitude of the positive BOLD response (Figure 6.2B). Only little variations were observed in the initial dip and post stimulus undershoot. When the BK channel conductance in the astrocyte is increased, the positive BOLD and the post stimulus undershoot decreases (Figure 6.2C, 6.2D). Increasing the buffering strength of the potassium buffer in the ECS, lead to a decrease in ECS potassium concentration and counter intuitively caused an increase in radius change (Figure 6.2E). This indicated that the baseline parameter set used here caused an ECS potassium concentration change slightly outside physiological range causing lesser dilation than the dilation caused for ECS potassium concentration in the physiological range. This increase in radius then generated an increase in the initial dip, positive BOLD and the negative BOLD response (Figure 6.2F). When the buffering strength of the potassium buffer in the ECS is decreased, it increased the ECS potassium concentration beyond the physiological range (Figure 6.2D) causing lesser dilation than the baseline value. This then generated a decrease

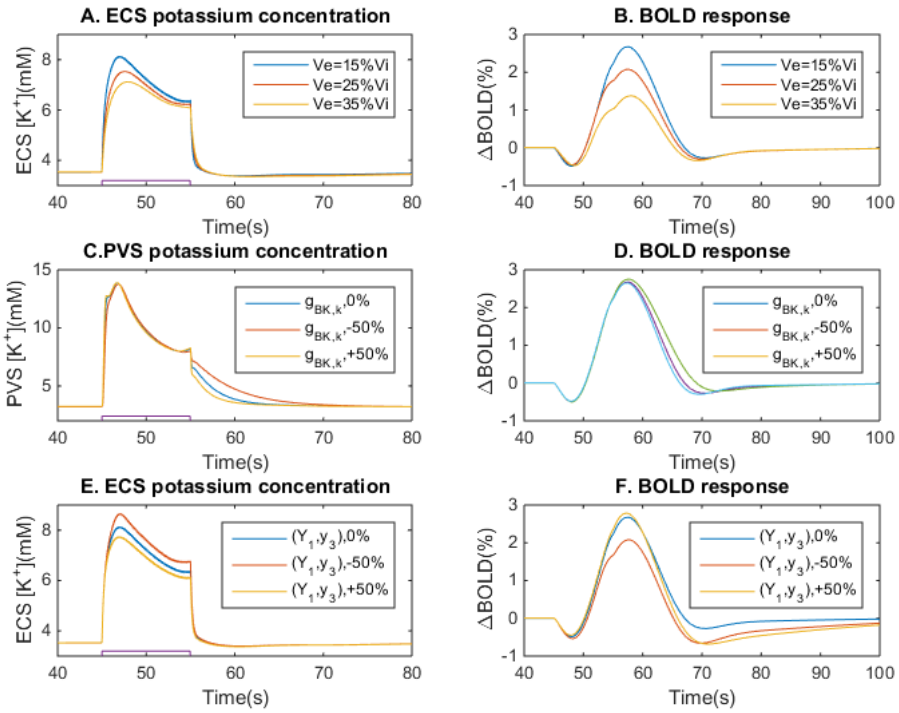

Fig. 6.2 Effects of variations to parameters that affect the K^+ signalling mechanism on the BOLD response. A stimulus amplitude of $0.014 mA/cm^2$ and duration of 10 s was used in all the simulations.

in positive BOLD and an increase in initial dip and post stimulus undershoot (Figure 6.2F).

6.2.3 Effects of variations of bursting frequency on the BOLD response

Neural bursting frequency is known to affect mechanisms in the brain such as long term potentiation (LTP) [37] which is significantly altered in disordered conditions such as Alzheimer's disease [19]. In the model bursting is obtained for sub threshold current stimulus and by increasing I_{max} value, different frequency of bursting is generated. When I_{max} value is increased to 400% of the original value, the bursting frequency was 0.20-0.27 Hz (Figure 6.3A) and the resultant BOLD response had an initial dip of -0.3953, a positive BOLD of 1 and a post stimulus undershoot of -0.2392 (Figure 6.3B).The peak of initial dip, positive or negative BOLD and post stimulus undershoot to the variations of I_{max} is given in Table 6.1. Note that the positive BOLD and initial dip decreases with increase in frequency of bursting and post stimulus undershoot showed mixed patterns for different frequencies.

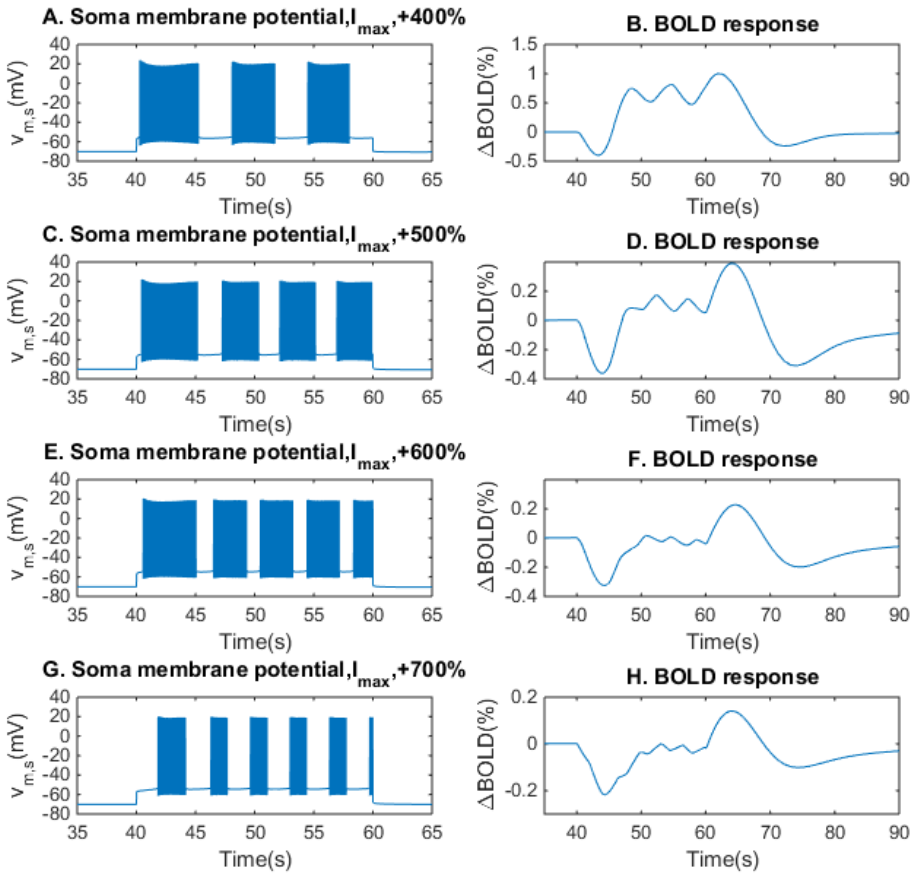

Fig. 6.3 Different bursting frequencies generates distinct BOLD responses. The I_{max} value is increased to tightly regulate the extracellular potassium concentration and generate bursting at different frequencies. A stimulus duration of 20 s was used in all the simulations. However the amplitude of the sub threshold current was different for different I_{max} values.

In addition to the parameters discussed, introducing other ionic regulatory mechanisms such as lateral diffusion would alter the neural behaviour [49] and consequently the BOLD response. However, this is considered to be beyond the scope of this present model. The Hodgkin Huxley type neuron model with time dependent ionic concentrations can have many variants of the active ion channels. Varying the maximal conductance value of any ion channel changes the threshold of input current that can generate spiking or bursting or cortical spreading depression.

Table 6.1 Peak of initial dip, positive or negative BOLD and post stimulus undershoot to the variations of mean transit time (τ_{MTT}), empirical relationship between CBF and CBV (d), ECS potassium buffering strength (Y_1, y_3), astrocytic BK channel conductance $g_{BK,k}$, maximum pumping rate I_{max} and extracellular volume (V_e) in the neurovascular coupling model. The variations of the parameter values were either physiologically known values or it is decreased or increased upto 50% of the baseline values.

Parameter changed	**initial dip**	**Peak signal**	**post stimulus undershoot**
Baseline value	-0.44	2.674	-0.26
$\tau_{MTT}, -50\%$	-0.6689	2.94	-0.5479
$\tau_{MTT}, +50\%$	-0.3823	2.383	-0.06189
$d, -50\%$	-0.44	2.827	-0.04548
$d, +50\%$	-0.44	2.563	-0.6741
$V_e, 0.25 \times V_i\%$	-0.9118	2.839	-0.6831
$V_e, 0.35 \times V_i\%$	-0.9963	3.485	-1.085
$g_{BK,k}, -50\%$	-0.44	2.748	-0.1757
$g_{BK,k}, +50\%$	-0.44	2.647	-0.2978
$Y_1, y_3, -50\%$	-0.5326	2.078	-0.6124
$Y_1, y_3, +50\%$	-0.4284	2.783	-0.6756
$I_{max}, +400\%$	-0.3953	1	-0.2392
$I_{max}, +500\%$	-0.3617	0.3919	-0.3097
$I_{max}, +600\%$	-0.3244	0.2283	-0.1982
$I_{max}, +700\%$	-0.2176	0.1409	-0.1012

6.2.4 Effects of variations of bursting frequency on the BOLD response

Even though a hippocampal neuron is used to simulate the neurovascular coupling and the BOLD response, to investigate if it can be compared with other areas of the brain, we compared the simulated CBF change to experimental CBF change in the cortex [102] for different stimulus conditions. A typical stimulus has a conditioning block (CS) and a probing block (PS) separated by a time interval referred to as the inter block stimulus interval (IBSI). The experimental conditions had used such stimulus conditions to investigate neural adaptation and recovery characteristics and their CBF response. We simulated the neurovascular coupling model with the same stimulus conditions and compared it with their experimental data. Figure 6.4 shows the comparison of simulated CBF change with the experimental data for CS=2s, IBSI=4s, PS=1s stimulus conditions. It shows a reasonably good match. The required scaling of the rate constants controlling the vessel response to match the experimental data indicates that the cortical vessel response is much faster than the vessel response induced by the hippocampal neuron.

Figure 6.5 shows the comparison of simulated CBF change with the experimental data for

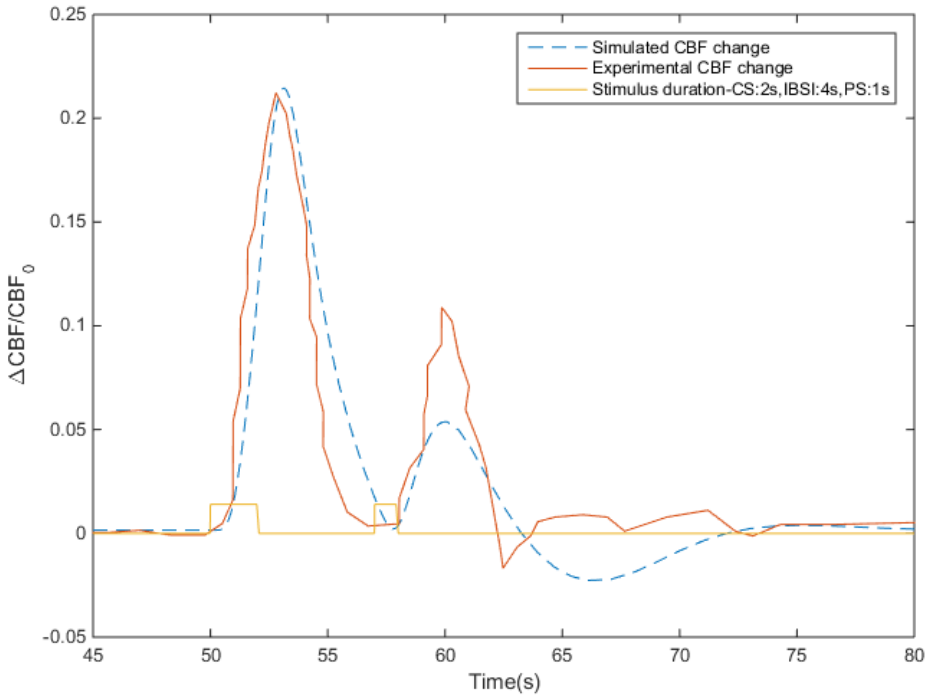

Fig. 6.4 Simulated CBF change compared with experimental CBF change in the cortex [102] for CS=2s, IBSI=4s, PS=1s stimulus conditions. A k value of 5.5 and the rate constants of the cross bridge formation model (Equation 3.22, 3.23, 3.24, 3.25, 3.26) scaled to 10 times of their original values was used in this simulation. Multiple simulations were run with different parameter values and the one that matched closely is shown here. The soma of the neuron is stimulated with a depolarizing current of $0.014 mA/cm^2$ during activation times.

CS=8s, IBSI=4s, PS=1s stimulus conditions. Even though the simulated data matched well with the first peak observed in the experimental data, it did not evoke a small second peak observed. Figure 6.5 shows the comparison of simulated CBF change with the experimental data for CS=16s, IBSI=4s, PS=1s stimulus conditions. Here the mismatch between the simulated and experimental data is more pronounced. The reasons for such a mismatch could be due to the differences in the vessel response across regions [23] or there could be another vasoactive factor released during longer stimulations.

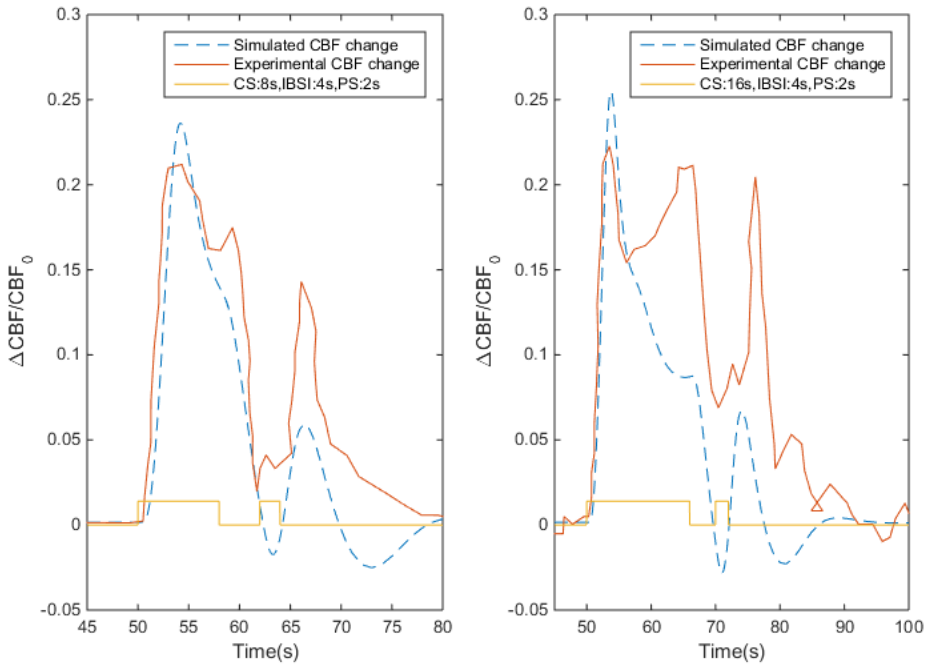

Fig. 6.5 Simulated CBF change compared with experimental CBF change in the cortex [102] for 8 s (CS=8s, IBSI=4s, PS=2s) and 16 s (CS=16s, IBSI=4s, PS=2s) stimulus conditions. A k value of 5.5 and the rate constants of the cross bridge formation model scaled to 5 times of their original values was used for 8s simulations. A k value of 5.5 and the rate constants of the cross bridge formation model scaled to 8 times of their original values was used for 16s simulations. Multiple simulations were run with different parameter values and the one that matched closely by observation is shown here. The soma of the neuron is stimulated with a depolarizing current of $0.014 mA/cm^2$ during activation times

6.2.5 Comparison of seizures and hypoxia in the hippocampus to simulated data

The neuron model used in the simulations is based on hippocampal pyramidal cells and hence we compared our simulated BOLD response to an experimental BOLD signal obtained from the hippocampus during seizures of long durations and 20 s hypoxic conditions. Figure 6.6 shows the 650 s of seizure data obtained from an individual rat in the hippocampus [85] compared with simulated seizures characterized by bursting. By analysing the CBV responses simultaneously Schridde et al reported that the observed large negative BOLD response is due to the $CMRO_2$ value being much higher than the CBF response. So to simulate the high $CMRO_2$ response the parameter θ is increased to 0.80. Even though the simulated profile generating a large negative BOLD followed by a positive BOLD the result

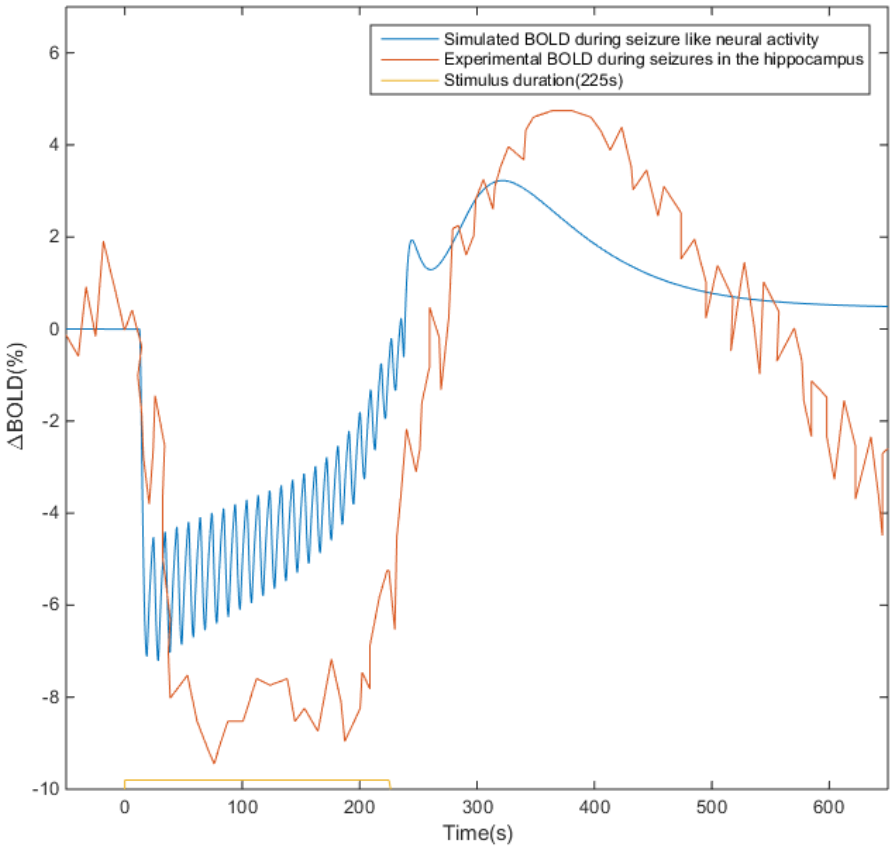

Fig. 6.6 Around 650 s of experimental data with 225 s of seizures obtained from an individual rat in the hippocampus [85] compared with simulated seizures characterized by bursting. A k value of 3.25 and θ value of 0.80 is used in the simulations. Multiple simulations were run with different parameter values and the one that matched closely by observation is shown here.

was similar to the experimental data, it still was not a close match. The differences observed in the simulated and experimental BOLD data could be due to the different frequencies of neural bursting between them.

We used the experimental data of Kannurpatti et al [57] for comparison where they have studied the dynamics of the BOLD signal induced by apnea in the cerebral cortex, hippocampus, third ventricle, and thalamus in the rat brain. Negative BOLD signals observed during apnea correspond to a decrease in arterial oxygen saturation which leads to decreased oxygen concentration in the tissue. We simulated the hypoxic condition by assuming that the fractional consumption of oxygen in the region increases during apnea which increases the value of $CMRO_2$ and thereby causing a negative BOLD signal. It simply means that if

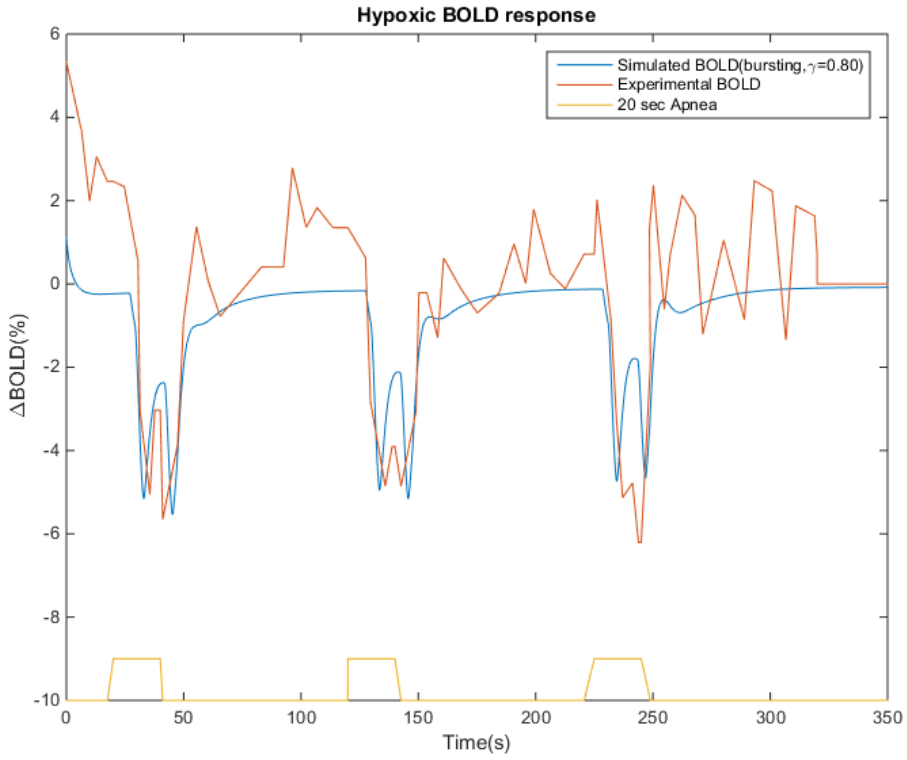

Fig. 6.7 The BOLD signal change from the baseline signal in the hippocampus of a rat during 20 sec of apnea observed in the hippocampus taken from the experimental data of Kannurpatti et al [57] is compared to the simulated BOLD response during bursting. Simulation of the hypoxic condition assumes that the fractional consumption of oxygen in the region increases during apnea as there is less oxygen available for the increased demand. The soma of the neuron is stimulated with a depolarizing current of $0.014 mA/cm^2$ during activation times.

there is less oxygen available to provide for the increased demand, it generates a negative BOLD signal. We plotted the experimental 20 seconds apnea hypoxic data against the simulated negative BOLD signal with $\theta = 0.80$ and a stimulus amplitude of $0.012 mA/cm^2$. Figure 6.7 shows the comparison between the experimental BOLD signal and the simulated BOLD signal during hypoxia. The simulated BOLD signal change is reasonably similar to the experimental negative BOLD signal change. A limitation of the comparison is that the dimensionless parameters a_1 and a_2 from (5.5) which are based on several experimental and physiological parameters were taken from the experimental work of Obata et al [76] and hence the values could be different for this particular experiment.

6.3 Discussion

In this chapter the variations of the BOLD signal that can occur due to the different experimentally relevant parameters in the model are shown. Using some of those variations in parameters, we compared the simulated BOLD response and neurovascular response to some experimental data available in the literature.

The mean transit time which is the time a specific volume of blood spends in the capillary circulation is a factor that can alter the BOLD response independent of the changes in CBF and $CMRO_2$. The factor is mainly attributed due to different distribution of capillaries in a region, their morphology and their interconnections. The independent action of this phenomenon is very evident in pathological conditions such as carotid stenosis where the oxygen extraction fraction increases without any changes to the cerebral blood flow or cerebral blood volume [22]. The presented model prediction shows that decreasing the value of the mean transit time increases the initial dip, positive BOLD and the post stimulus undershoot whilst increasing the value decreases the BOLD transients. Here, the mean transit time is assumed to be constant. However experiments show that it this can increase during during activation [93] and also reduce gradually depending on the strength of stimulus current [86]. It still remains to be understood whether capillary morphology and its effects on the mean transit time has an influence on disordered conditions like hypertension, stroke, Alzheimer's disease and diabetes where oxygen extraction fraction is significantly affected. Jespersen et al [53], with their mathematical model of capillary transit time heterogeneity in the brain suggested that maintaining a low transit time is important during hypoxic conditions and even during normal functional hyperemia.

The relationship between the cerebral blood flow and the cerebral blood volume is particularly important as it is one the fundamental assumptions behind the BOLD response. In the presented model the relationship between blood flow and blood volume is determined by the parameter d in equation (5.2) of chapter 5 which is assumed to be 0.4 following Buxton et al [12]. However this parameter value was originally chosen from whole brain measurements of an animal model. Recent experiments on humans show that this parameter value can range from 0.2 [17] to 0.6 [65]. Variations to this parameter in the model show that decreasing the value, leads to an increase in positive BOLD and a decrease in post stimulus undershoot amplitude and duration and increasing it decreases the amplitude of the positive BOLD while increasing the amplitude and duration of the post stimulus undershoot.

Any parameter that affects the regulation and transmission of potassium ions from the neuron to the smooth muscle cell will have an effect on the vascular response and hence the BOLD signal. We have shown the effects of variations to certain important parameters in the the model. An increase in extracellular volume decreases the peak of the BOLD transients

by decreasing the potassium ion concentration in the extracellular space. An increase in extracellular potassium outside the physiological range (4-8 mM) has a constrictory effect on the arteriole. This is demonstrated by the variations of the parameters g_{BK_k} and Y_1, y_3. In addition to these the variations of the maximum conductance values and gating properties of the ion channels in the neuron, astrocyte, smooth muscle cell and endothelial cell will also have an effect on the neurovascular and the BOLD response.

The motivation for the comparison between simulated cerebral blood flow changes and the experimental cerebral blood flow changes in the cortex is to investigate whether the neurovascular response due to K^+ signalling mechanism in the hippocampus is enough to represent the blood flow response in any other region. The comparison shows that for short stimulus (2 s) conditions the simulated and experimental flow changes matches well. However for longer stimulus conditions (8 s,16 s) it doesn't fit well. The mismatch comes after about 8s where the experimental blood flow response approaches a second peak before decaying down to steady state, whereas the simulated blood flow response decays slowly after the first peak till the end of stimulus and then decays rapidly after the end of stimulus. The reasons for such a discrepancy could be multi fold. One plausible reason is that there could be other vasoactive factors such as nitric oxide released during longer stimulations which might activate the vessel with a different magnitude and time scale. Another possible explanation is that neural activation due to many neurons in a region will release potassium ions into the extracellular space in an activity dependent manner which will cause the vessel response accordingly.

Different frequency of bursting generated by the hippocampal neuron model resulted in distinct BOLD responses. The cellular mechanisms driving such bursts and the purpose of them is not fully understood as it is a result of intrinsic membrane properties. However the persistent sodium channel is thought be driving such bursts in the CA1 hippocampal region [52]. The presented model also has the persistent sodium channel in both soma and dendrite which may be driving the bursts observed in the model. The results presented from the neuron model has burst frequency in the range of 0.2-0.72 Hz. One potent purpose of different frequency of bursts in the CA1 hippocampal region is that it facilitates Long-term potentiation (LTP) which is a strengthening of synapses based on patterns of activity. A study which tested the effects of neural burst frequency over the range of 10 Hz to 0.05 Hz on LTP found that the maximum LTP occured at around 2-3 Hz [37].

Epileptic seizures and cortical spreading depression can lead to hypoxic conditions and the reverse is also found to be true in many experiments [95, 94, 84]. During cortical spreading depression the BOLD response is mostly negative as the high extracellular potassium released during steady depolarisation of the neuronal membrane generates a negative BOLD signal. However seizures generate a mix of positive and negative BOLD responses and

hence can be used to study both of them simultaneously. This mix of both is observed in many experimental conditions studying BOLD responses during seizures in humans [1, 4]. The comparison between experimental seizure data and simulated bursting data showed a reasonable match. The variations observed could be due to the difference of frequency of bursting between the two. The hypoxic experimental data observed in the hippocampus which was also compared with seizure data showed a close match. The hypoxia is induced in the simulated seizure model by increasing the fractional consumption of oxygen by the Na^+/K^+ ATPase pump which decreases the tissue oxygen concentration.

6.4 Conclusions

In this chapter the effects of variations of mean transit time, empirical relationship between CBF and CBV, ECS potassium buffering strength, astrocytic BK channel conductance, maximum pumping rate and extracellular volume in the neurovascular coupling model on the BOLD response are reported. When fine tuning the model to a certain region of the brain, parameters need to be changed according to the experimental data of that region. Different frequency of bursting generated by the hippocampal neuron model resulted in distinct BOLD responses. Comparison of the simulated CBF change to that of cortex showed close match for short simulations, however did not match very well for longer simulations. The comparison of simulated seizures data and experimental seizure data showed a reasonable match. The variations seen might be due to the different burst frequencies. The hypoxic BOLD data showed close match with the simulated bursting data for high $CMRO_2$ values.

Chapter 7

Concluding Remarks

7.1 Findings and conclusions with regard to the research questions

The broad aim of this research was to establish a mathematical framework for modelling a certain hypothesis of neurovascular coupling and its associated BOLD response to compare it with experimental BOLD data and generate verifiable hypothesis. To that end different existing models were used to model the K^+ signalling hypothesis of neurovascular coupling mechanism and its associated neurometabolic response. These responses were then used to simulate the BOLD response and compare it to experimental data. The presented model is able to predict the different transients in the BOLD response such as the initial dip, positive BOLD, negative BOLD and the post stimulus undershoot due to the neurovascular and neurometabolic responses.

In chapter 3, the fundamental units of the neurovascular coupling model such as the neuron, astrocyte and vasculature were presented and the results arising out of them were discussed. The neuron model exhibits different kinds of behaviours such as continuous spiking, bursting and cortical spreading depression for varying regulation of extracellular potassium concentration. In this model the regulation is primarily done by the Na^+/K^+ ATPase exchange pump and the phenomenological potassium buffer. For certain sub threshold stimulus currents the model generates bursting and for high threshold currents it goes into cortical spreading mode. The neurovascular response simulated with the model of Dormanns et al provided 23% increase in radius for a 50s long stimulation and it provided only a 2% increase for 10s long stimulation. The vascular response of the model entered an oscillatory state for certain values of IP_3 production rate in the endothelium and this suppressed the neurovascular coupling mechanism with contraction.

In chapter 4, the coupling made between the neuron and the astrocyte leads to the vascular response whereas the coupling made between the neuron and the vasculature provides the energy to the neuron to continue its function. When CSD is induced in neuron model, the potassium concentration increased to very high values (80-100 mM) inducing 11.5% decrease in the radius. The percentage increase in radius change induced by the continuously spiking neuron model was 14.35% and that of bursting neuron model was 9.3%. These vascular responses had their corresponding effects on the tissue oxygenation and thereby affecting the functioning of the sodium potassium exchange pump.

The neuron model is based on the work of Chang et al [16] and Kager et al[55] who studied cortical spreading depression. The combination of both their model is used to describe neural activation, restoration of ionic gradients and consumption of Na^+/K^+ -ATPase pump. The neuron model is used here to describe a group of neurons in a certain region which can exhibit many different behaviours such as continuous spiking and bursting. To observe normal spiking for longer periods, the extracellular potassium has to be tightly regulated. This was achieved by increasing the maximum pumping rate of Na^+/K^+ ATPase exchange pump which restores the ionic equilibrium. The vascular response was computed based on the work of Dormanns et al [24]. The extracellular ionic changes were given as an input to the astrocyte model to generate a vascular response.

While the results of the model suggests that potassium ions released during neural activity could act as the main mediator in neurovascular coupling, along with cytosolic calcium in the smooth muscle cell it certainly does not rule out the possibility of other mechanisms that can coexist and increase blood flow, such as the nitric oxide signalling mechanism or the archidonic acid to EET pathway [27]. The high potassium efflux from the neuron leading to vasoconstriction in the model shows that the neurovascular coupling response cannot be thought of as a linear function of neural activity in any region as some earlier studies suggested [10]. This also emphasizes the need to understand how each of the experimentally identified vasoactive factors influence the blood vessel response.

In chapter 5 we have presented the BOLD responses arising out of the neurovascular and neurometabolic responses for different neuronal behaviours. The relative change of CBF to $CMRO_2$ determines the magnitude of the BOLD signal and whether it is a positive or negative BOLD. The initial dip observed in the BOLD response is a consequence of the delay between the neural activity and the vascular response. The model suggests that both the delayed vascular compliance of the venous blood flow and the prolonged time taken for the Na^+/K^+ ATPase pump to restore ionic homeostasis can contribute to the post stimulus undershoot observed in the BOLD response. A negative BOLD response was observed for bursting behaviour and CSD behaviour of the neuron. However, it can arise for variation of

the parameter θ and any other parameter that drives the extracellular potassium out of the physiological range. Low values of $CMRO_2$ gave an initial dip and large values gave a large negative BOLD response. The post stimulus undershoot observed in the BOLD response can either be due to the delayed vascular compliance of the venous blood flow or due to the prolonged time taken for the Na^+/K^+ ATPase pump to restore ionic homeostasis [98] as shown in our results.

In chapter 6 the effects of variations of mean transit time, empirical relationship between CBF and CBV, ECS potassium buffering strength, astrocytic BK channel conductance, maximum pumping rate and extracellular volume in the neurovascular coupling model on the BOLD response are reported. When fine tuning the model to a certain region of the brain, parameters need to be changed according to the experimental data of that region. Different frequency of bursting generated by the hippocampal neuron model resulted in distinct BOLD responses. Comparison of the simulated CBF change to that of cortex showed close match for short simulations, however did not match very well for longer simulations. The comparison of simulated seizures data and experimental seizure data showed a reasonable match. The variations seen might be due to the different burst frequencies. The hypoxic BOLD data showed close match with the simulated bursting data for high $CMRO_2$ values.

A model of neurovascular coupling and associated BOLD signals from various time-varying stimuli is presented. We have shown that varying the volumetric ratio of synaptic to extracellular space and the fraction (k) of available synapes per astrocyte leads to substantially different BOLD signals. Experimental data indicates that this value of k can vary substantially from 4 to greater than 150. The model shows that varying k by 50% leads to substantial dilation or contraction. Predominantly this is due to the factor k representing the amount of K^+ flux entering the synaptic cleft which having been taken up by the astrocyte, its subsequent depolarisation and thence outflux into the perivascular space causes the smooth muscle cell to hyperpolarise and shut off any Ca^{2+} entering the cytosol. The factor k has a particular sensitivity to the resulting vascular radius. From an anatomical point of view areas of the brain tissue may very well have a substantial variation in the number of synapses available to a single astrocyte causing differing BOLD signals for similar stimuli.

Bursting phenomena provides relatively clear BOLD signals as long as the time between bursts is not too short where the BOLD signal remains constant even though the neuron is in a predominant bursting mode. Simulation of cortical spreading depression exhibits large negative BOLD signals. Visco-elastic effects of the capillary bed do not seem to have a large effect on the BOLD signal even for relatively high values of oxygen consumption. Finally comparison with experimental data shows good agreement when smooth muscle cell kinetics are changed to increase the rate of change of the arteriolar radius. The model does

not compare well for stimuli between 8 and 16 seconds. It is suggested that this is due to buffering of the K^+ concentration in the ECS and the subsequent large times taken to reach steady state. This could be improved by varying the buffering parameters however this will be explored further in future works.
The modelling framework presented in this thesis may play an important role in driving the future of research on neurovascular coupling and the BOLD response. It provides a way of combining neurovascular and BOLD models by computing the associated metabolic response. Such a framework will allow to test and validate any underlying hypothesis of neurovascular and neurometabolic mechanisms. Previous modelling efforts have either focused on the neurometabolic response [54] or the mechanism of neurovascular coupling [27, 24] or determining the BOLD response from CBF and $CMRO_2$ [12], but none of these integrated all of these responses simultaneously. The presented model also emphasises the need to quantify the responses in a region with respect to neural function by showing that the responses change significantly for different underlying neural activities such as continuous spiking, bursting and Cortical spreading depression.

7.2 Model Limitations and Future works

In the presented model, the functions performed by the neuron such as continuous spiking and bursting are assumed to be a group of active neurons in a certain region of the brain. However a certain function performed in a region could evoke different amplitude and patterns of neural activity within the same region [26]. This could also evoke different neurovascular response and neurometabolic response and hence different BOLD response. Hence the neuron model must be expanded to connect with other neuron models through the synaptic space and extracellular space to simulate specific functions involving synaptic activity and extracellular space ion propagation. By connecting them together certain functions performed in the brain such as Long term Potentiation (LTP) could be simulated and its BOLD response could be explored. The LTP is known to be affected during pathological conditions such as Alzheimer's disease [19]. The amyloid beta peptides (Abeta) are believed to play a role in the development of memory loss which is a characteristic of Alzheimer's disease. Experimental studies found that hippocampal slices with low concentration of Abeta had LTP induction inhibition. The neurovascular response is also found to be altered during Alzheimer's disease. Hence modelling the LTP and its vascular response will enable to study the neurovascular mechanism with respect to the underlying neural function causing it.
The neurovascular mechanism has been proven to be one of the most complex mechanisms

in the brain due to the many parameters involved in it. For many years, researchers believed that a single vasoactive factor can induce vasodilation but recently it became clear that many factors that are vasoactive can act in concert to determine the vessel response [29]. Hence systematically modelling all these mechanisms that are known to contribute to the vascular response can elucidate the dynamics at play. In addition to that it will also give more information on the neural activity underlying the BOLD signal. As the BOLD signal is also determined by the cerebral metabolic rate of oxygen, the mechanisms underlying metabolism in the brain must also be modelled to understand it further. The cerebral metabolic rate of oxygen in the presented model is based on the assumption that 95% of oxygen available in the tissue are produced by aerobic mechanism and 5% by non aerobic mechanism. Recent experiments have highlighted the possibility of energy substrates other than glucose such as lactate that can account for 10-12 % of glucose metabolism in the human brain even when enough oxygen is available [97]. In addition to that, it is assumed the Na^+/K^+ ATPase pump is the only active consumer of the oxygen during neural activity. However there could be other active functions in the neuron performing other tasks and consuming oxygen. Modelling an hypothesis of metabolism including all these aspects is likely to result in more accurate $CMRO_2$ response.

The comparison of simulated CBF changes to experimental CBF changes in the cortex suggested that for longer simulations, there could be other active vasoactive factors that can control the vascular response. Hence modelling other signalling mechanisms such as nitric oxide pathways along with the K^+ signalling mechanism might change the dynamics of the CBF response and hence the BOLD response. The apnea condition is simulated in the model by the increasing the fractional consumption of the Na^+/K^+ ATPase pump. Even though both of it leads to decreased tissue oxygen concentration, modelling the exact mechanism through which hypoxia affects the neural activity may be better. Another limitation of the comparison with the BOLD responses is that the dimensionless parameters a_1 and a_2 (Equation 5.5) which are based on several experimental and physiological parameters were taken from the experimental work of Obata et al [76] and hence the values could be different for any other particular experiment. Hence a method to determine these parameters based on the experimental conditions needs to be established .

The model is not able to provide definitive information on the complex cellular functions from a simple BOLD response to a stimulation due to its non-unique nature (the model is not a one-to-one mapping meaning that several parameter settings can evoke the same BOLD signal). However, it does provide a better insight into the possible causes of various BOLD signals associated with various cortical or hippocampal stimuli at this stage. Detailed models that can represent all the physiological parameters that can cause a change in the

fMRI BOLD signal and repetitive comparison to the experimental data will help us suss out the actual mechanism behind the signal.
During the last two decades fMRI has proven to be an established tool in studying the human brain. However it still has not been used to study the underlying neural architecture and functions in the brain. Complex models that address this question is the need of the hour as many brain disorders can be studied using this. Constructing a detailed compartmental model with all the cell types involved which will allow to relate a certain brain function performed in a region to the neurovascular and neurometabolic responses will pave the way forward. This presented research work is one step towards that.

References

[1] Aghakhani, Y., Bagshaw, A. P., Bénar, C. G., Hawco, C., Andermann, F., Dubeau, F., and Gotman, J. (2004). fMRI activation during spike and wave discharges in idiopathic generalized epilepsy.

[2] Ames, A. (2000). CNS energy metabolism as related to function. *Brain Research Reviews*, 34:42–68.

[3] Aperia, A. (2001). Regulation of sodium/potassium atpase activity: Impact on salt balance and vascular contractility. *Current Hypertension Reports*, 3(2):165–171.

[4] Archer, J. S., Abbott, D. F., Waites, A. B., and Jackson, G. D. (2003). fMRI "deactivation" of the posterior cingulate during generalized spike and wave. *NeuroImage*, 20(4):1915–1922.

[5] Attwell, D., Buchan, A. M., Charpak, S., Lauritzen, M., Macvicar, B. A., and Newman, E. A. (2010). Glial and neuronal control of brain blood flow. *Nature*, 468:232–243.

[6] Attwell, D. and Iadecola, C. (2002). The neural basis of functional brain imaging signals. *Trends in Neurosciences*, 25:621–625.

[7] Attwell, D. and Laughlin, S. B. (2001). An energy budget for signaling in the grey matter of the brain. *Journal of cerebral blood flow and metabolism : official journal of the International Society of Cerebral Blood Flow and Metabolism*, 21:1133–1145.

[8] Bennett, M. R., Farnell, L., and Gibson, W. G. (2008). Origins of blood volume change due to glutamatergic synaptic activity at astrocytes abutting on arteriolar smooth muscle cells. *Journal of Theoretical Biology*, 250:172–185.

[9] Billig, S. (2012). A heart beat is enough. http://www.deutschlandfunk.de/ein-herzschlag-genuegt.676.de.html?dram:article_id=210454. [Online; accessed 03-March-2017].

[10] Boynton, G. M., Engel, S. A., Glover, G. H., and Heeger, D. J. (1996). Linear Systems Analysis of Functional Magnetic Resonance Imaging in Human V1. *The Journal of Neuroscience*, 16(13):4207–4221.

[11] Buxton, R. B. (2002). Coupling between CBF and CMRO2 during neuronal activity. *International Congress Series*, 1235:23–32.

[12] Buxton, R. B., Uludağ, K., Dubowitz, D. J., and Liu, T. T. (2004). Modeling the hemodynamic response to brain activation. *NeuroImage*, 23 Suppl 1:S220–33.

[13] Buxton, R. B., Wong, E. C., and Frank, L. R. (1998). Dynamics of blood flow and oxygenation changes during brain activation: The balloon model. *Magnetic Resonance in Medicine*, 39:855–864.

[14] Campbell, W. B., Gebremedhin, D., Pratt, P. F., and Harder, D. R. (1996). Identification of epoxyeicosatrienoic acids as endothelium-derived hyperpolarizing factors. *Circulation research*, 78(3):415–23.

[15] Cannon, R. C., Turner, D. A., Pyapali, G. K., and Wheal, H. V. (1998). An on-line archive of reconstructed hippocampal neurons. *Journal of Neuroscience Methods*, 84:49–54.

[16] Chang, J. C., Brennan, K. C., He, D., Huang, H., Miura, R. M., Wilson, P. L., and Wylie, J. J. (2013). A Mathematical Model of the Metabolic and Perfusion Effects on Cortical Spreading Depression. *PLoS ONE*, 8.

[17] Chen, J. J. and Pike, G. B. (2009a). BOLD-specific cerebral blood volume and blood flow changes during neuronal activation in humans. *NMR in Biomedicine*, 22(10):1054–1062.

[18] Chen, J. J. and Pike, G. B. (2009b). Origins of the BOLD post-stimulus undershoot. *NeuroImage*, 46(3):559–568.

[19] Chen, Q. S., Kagan, B. L., Hirakura, Y., and Xie, C. W. (2000). Impairment of hippocampal long-term potentiation by Alzheimer amyloid beta-peptides. *Journal of neuroscience research*, 60(1):65–72.

[20] Chih, C.-P. and Roberts Jr, E. L. (2003). Energy substrates for neurons during neural activity: a critical review of the astrocyte-neuron lactate shuttle hypothesis. *Journal of cerebral blood flow and metabolism : official journal of the International Society of Cerebral Blood Flow and Metabolism*, 23:1263–1281.

[21] Cloutier, M., Bolger, F. B., Lowry, J. P., and Wellstead, P. (2009). An integrative dynamic model of brain energy metabolism using in vivo neurochemical measurements. *Journal of Computational Neuroscience*, 27:391–414.

[22] Derdeyn, C. P., Videen, T. O., Yundt, K. D., Fritsch, S. M., Carpenter, D. A., Grubb, R. L., and Powers, W. J. (2002). Variability of cerebral blood volume and oxygen extraction: stages of cerebral haemodynamic impairment revisited. *Brain*, 125(3):595–607.

[23] Devonshire, I. M., Papadakis, N. G., Port, M., Berwick, J., Kennerley, A. J., Mayhew, J. E. W., and Overton, P. G. (2012). Neurovascular coupling is brain region-dependent. *NeuroImage*, 59(3):1997–2006.

[24] Dormanns, K., van Disseldorp, E. M. J., Brown, R. G., and David, T. (2015). Neurovascular coupling and the influence of luminal agonists via the endothelium. *Journal of theoretical biology*, 364:49–70.

[25] Ekstrom, A. (2010). How and when the fMRI BOLD signal relates to underlying neural activity: The danger in dissociation.

[26] Enager, P., Piilgaard, H., Offenhauser, N., Kocharyan, A., Fernandes, P., Hamel, E., and Lauritzen, M. (2009). Pathway-specific variations in neurovascular and neurometabolic coupling in rat primary somatosensory cortex. *Journal of cerebral blood flow and metabolism : official journal of the International Society of Cerebral Blood Flow and Metabolism*, 29:976–986.

[27] Farr, H. and David, T. (2011). Models of neurovascular coupling via potassium and EET signalling. *Journal of theoretical biology*, 286(1):13–23.

[28] Filosa, J. A. and Blanco, V. M. (2007). Neurovascular coupling in the mammalian brain. *Experimental physiology*, 92:641–646.

[29] Filosa, J. a., Bonev, A. D., Straub, S. V., Meredith, A. L., Wilkerson, M. K., Aldrich, R. W., and Nelson, M. T. (2006). Local potassium signaling couples neuronal activity to vasodilation in the brain. *Nature neuroscience*, 9(11):1397–1403.

[30] Forrest, M. D. (2014). The sodium-potassium pump is an information processing element in brain computation. *Frontiers in Physiology*, 5(Nov).

[31] Fox, P. T. and Raichle, M. E. (1986). Focal physiological uncoupling of cerebral blood flow and oxidative metabolism during somatosensory stimulation in human subjects.

Proceedings of the National Academy of Sciences of the United States of America, 83:1140–1144.

[32] Girouard, H., Bonev, A. D., Hannah, R. M., Meredith, A., Aldrich, R. W., and Nelson, M. T. (2010). Astrocytic endfoot Ca2+ and BK channels determine both arteriolar dilation and constriction. *Proceedings of the National Academy of Sciences of the United States of America*, 107:3811–3816.

[33] Girouard, H. and Iadecola, C. (2006). Neurovascular coupling in the normal brain and in hypertension, stroke, and Alzheimer disease. *Journal of applied physiology (Bethesda, Md. : 1985)*, 100(1):328–35.

[34] Gordon, G. R. J., Choi, H. B., Rungta, R. L., Ellis-Davies, G. C. R., and MacVicar, B. A. (2008). Brain metabolism dictates the polarity of astrocyte control over arterioles. *Nature*, 456(7223):745–9.

[35] Gore, R. W. and Davis, M. J. (1984). Mechanics of smooth muscle in isolated single microvessels. *Annals of biomedical engineering*, 12(5):511–520.

[36] Grimm, S., Boesiger, P., Beck, J., Schuepbach, D., Bermpohl, F., Walter, M., Ernst, J., Hell, D., Boeker, H., and Northoff, G. (2009). Altered negative BOLD responses in the default-mode network during emotion processing in depressed subjects. *Neuropsychopharmacology : official publication of the American College of Neuropsychopharmacology*, 34(4):932–843.

[37] Grover, L. M., Kim, E., Cooke, J. D., and Holmes, W. R. (2009). Ltp in hippocampal area ca1 is induced by burst stimulation over a broad frequency range centered around delta. *Learning & memory*, 16 1:69–81.

[38] Gusnard, D. A., Raichle, M. E., and Raichle, M. E. (2001). Searching for a baseline: functional imaging and the resting human brain. *Nature reviews. Neuroscience*, 2:685–694.

[39] Hadjikhani, N., Sanchez Del Rio, M., Wu, O., Schwartz, D., Bakker, D., Fischl, B., Kwong, K. K., Cutrer, F. M., Rosen, B. R., Tootell, R. B., Sorensen, A. G., and Moskowitz, M. A. (2001). Mechanisms of Migraine Aura Revealed by Functional MRI in Human Visual Cortex. *Proceedings of the National Academy of Sciences of the United States of America*, 98(8):4687–92.

[40] Hai, C. M. and Murphy, R. A. (1989). Ca^{2+}, crossbridge phosphorylation, and contraction. *Annual review of physiology*, 51:285–298.

[41] Hall, J. E. and Guyton, A. C. (2010). *Guyton and Hall textbook of medical physiology*.

[42] Hamilton, N. B., Attwell, D., and Hall, C. N. (2010). Pericyte-mediated regulation of capillary diameter: a component of neurovascular coupling in health and disease. *Frontiers in neuroenergetics*, 2(May):1–14.

[43] Harder, D. R., Narayanan, J., Birks, E. K., Liard, J. F., Imig, J. D., Lombard, J. H., Lange, A. R., and Roman, R. J. (1996). Identification of a putative microvascular oxygen sensor. *Circulation research*, 79(1):54–61.

[44] Heinrich, R. and Schuster, S. (1996). *The regulation of cellular systems*.

[45] Hodgkin, a. L. and Huxley, a. F. (1952). A quantitative description of membrane current and its applicaiton to conduction and excitation in nerve. *J Physiol*, 117:500–544.

[46] Hoffmeyer, H. W., Enager, P., Thomsen, K. J., and Lauritzen, M. J. (2007). Nonlinear neurovascular coupling in rat sensory cortex by activation of transcallosal fibers. *Journal of cerebral blood flow and metabolism : official journal of the International Society of Cerebral Blood Flow and Metabolism*, 27(3):575–87.

[47] Hoge, R. D., Atkinson, J., Gill, B., Crelier, G. R., Marrett, S., and Pike, G. B. (1999). Linear coupling between cerebral blood flow and oxygen consumption in activated human cortex. *Proceedings of the National Academy of Sciences of the United States of America*, 96:9403–9408.

[48] Hu, X. and Yacoub, E. (2012). The story of the initial dip in fMRI.

[49] Hubel, N. and Dahlem, M. a. (2014). Dynamics from seconds to hours in hodgkin-huxley model with time-dependent ion concentrations and buffer reservoirs. *PLoS computational biology*, 10(12):e1003941.

[50] Iadecola, C. (2004). Neurovascular regulation in the normal brain and in Alzheimer's disease. *Nature reviews. Neuroscience*, 5(5):347–60.

[51] Iadecola, C. and Nedergaard, M. (2007). Glial regulation of the cerebral microvasculature. *Nature neuroscience*, 10(11):1369–1376.

[52] Jensen, M. S., Azouz, R., and Yaari, Y. (1996). Spike after-depolarization and burst generation in adult rat hippocampal CA1 pyramidal cells. *The Journal of physiology*, 492 (Pt 1(1 996):199–210.

[53] Jespersen, S. N. and Ostergaard, L. (2012). The roles of cerebral blood flow, capillary transit time heterogeneity, and oxygen tension in brain oxygenation and metabolism. *Journal of Cerebral Blood Flow & Metabolism*, 32(2):264–277.

[54] Jolivet, R., Coggan, J. S., Allaman, I., and Magistretti, P. J. (2015). Multi-timescale Modeling of Activity-Dependent Metabolic Coupling in the Neuron-Glia-Vasculature Ensemble. *PLOS Computational Biology*, 11:e1004036.

[55] Kager, H., Wadman, W. J., and Somjen, G. G. (2000). Simulated seizures and spreading depression in a neuron model incorporating interstitial space and ion concentrations. *Journal of neurophysiology*, 84(1):495–512.

[56] Kager, H., Wadman, W. J., and Somjen, G. G. (2002). Conditions for the triggering of spreading depression studied with computer simulations. *Journal of neurophysiology*, 88:2700–2712.

[57] Kannurpatti, S. S., Biswal, B. B., and Hudetz, A. G. (2003). Regional dynamics of the fMRI-BOLD signal response to hypoxia-hypercapnia in the rat brain. *Journal of Magnetic Resonance Imaging*, 17:641–647.

[58] Koenigsberger, M., Sauser, R., Beny, J., and Meister, J. (2006). Effects of arterial wall stress on vasomotion. *Biophysical journal*, 91(5):1663–1674.

[59] Kreisman, N. R., Sick, T. J., and Rosenthal, M. (1984). Concepts of brain oxygen sufficiency during seizures. *Adv Exp Med Biol*, 180:381–392.

[60] Kudryashov, N. and Chernyavskii, I. (2008). Numerical simulation of the process of autoregulation of the arterial blood flow. *Fluid Dynamics*, 43(1):32–48.

[61] Laughlin, S. B., de Ruyter van Steveninck, R. R., and Anderson, J. C. (1998). The metabolic cost of neural information. *Nature neuroscience*, 1:36–41.

[62] Lauritzen, M. (2001). Relationship of Spikes, Synaptic Activity, and Local Changes of Cerebral Blood Flow.

[63] Leithner, C., Royl, G., Offenhauser, N., Füchtemeier, M., Kohl-Bareis, M., Villringer, A., Dirnagl, U., and Lindauer, U. (2010). Pharmacological uncoupling of activation induced increases in CBF and CMRO2. *Journal of cerebral blood flow and metabolism : official journal of the International Society of Cerebral Blood Flow and Metabolism*, 30(2):311–322.

[64] Leontiev, O., Dubowitz, D. J., and Buxton, R. B. (2007). CBF/CMRO2 coupling measured with calibrated BOLD fMRI: Sources of bias. *NeuroImage*, 36(4):1110–1122.

[65] Lin, A.-L., Fox, P. T., Yang, Y., Lu, H., Tan, L.-H., and Gao, J.-H. (2008). Evaluation of mri models in the measurement of cmro2 and its relationship with cbf. *Magnetic resonance in medicine*, 60(2):380–389.

[66] Lindauer, U., Leithner, C., Kaasch, H., Rohrer, B., Foddis, M., Füchtemeier, M., Offenhauser, N., Steinbrink, J., Royl, G., Kohl-Bareis, M., and Dirnagl, U. (2010). Neurovascular coupling in rat brain operates independent of hemoglobin deoxygenation. *Journal of cerebral blood flow and metabolism : official journal of the International Society of Cerebral Blood Flow and Metabolism*, 30(4):757–768.

[67] Longden, T. A., Hill-Eubanks, D. C., and Nelson, M. T. (2016). Ion channel networks in the control of cerebral blood flow. *Journal of Cerebral Blood Flow & Metabolism*, 36:492–512.

[68] Makani, S. and Chesler, M. (2010). Rapid rise of extracellular pH evoked by neural activity is generated by the plasma membrane calcium ATPase. *Journal of neurophysiology*, 103(2):667–76.

[69] Mazel, T., Simonova, Z., and Sykova, E. (1998). Diffusion heterogeneity and anisotropy in rat hippocampus. *Neuroreport*, 9:1299–1304.

[70] McBain, C. J., Traynelis, S. F., and Dingledine, R. (1990). Regional variation of extracellular space in the hippocampus. *Science (New York, N.Y.)*, 249:674–677.

[71] Megias, M., Emri, Z., Freund, T., and Gulyas, A. (2001). Total number and distribution of inhibitory and excitatory synapses on hippocampal CA1 pyramidal cells. *Neuroscience*, 102(3):527–540.

[72] Mintun, M. A., Lundstrom, B. N., Snyder, A. Z., Vlassenko, A. G., Shulman, G. L., and Raichle, M. E. (2001). Blood flow and oxygen delivery to human brain during functional activity: theoretical modeling and experimental data. *Proc Natl Acad Sci U S A*, 98(12):6859–64.

[73] Mulligan, S. J. and MacVicar, B. A. (2004). Calcium transients in astrocyte endfeet cause cerebrovascular constrictions. *Nature*, 431(7005):195–199.

[74] Newman, E. A. (1984). Regional specialization of retinal glial cell membrane. *Nature*, 309(5964):155–157.

[75] Nicholson, C. and Phillips, J. M. (1981). Ion diffusion modified by tortuosity and volume fraction in the extracellular microenvironment of the rat cerebellum. *The Journal of physiology*, 321:225–257.

[76] Obata, T., Liu, T. T., Miller, K. L., Luh, W. M., Wong, E. C., Frank, L. R., and Buxton, R. B. (2004). Discrepancies between BOLD and flow dynamics in primary and supplementary motor areas: Application of the balloon model to the interpretation of BOLD transients. *NeuroImage*, 21:144–153.

[77] Ostby, I., Oyehaug, L., Einevoll, G. T., Nagelhus, E. A., Plahte, E., Zeuthen, T., Lloyd, C. M., Ottersen, O. P., and Omholt, S. W. (2009). Astrocytic mechanisms explaining neural-activity-induced shrinkage of extraneuronal space. *PLoS Computational Biology*, 5.

[78] Peppiatt, C. M., Howarth, C., Mobbs, P., and Attwell, D. (2006). Bidirectional control of CNS capillary diameter by pericytes. *Nature*, 443(7112):700–4.

[79] Powers, W. J., Hirsch, I. B., and Cryer, P. E. (1996). Effect of stepped hypoglycemia on regional cerebral blood flow response to physiological brain activation. *Am J Physiol*, 270(2 Pt 2):H554–9.

[80] Raichle, M. E. and Mintun, M. A. (2006). Brain work and brain imaging. *Annual review of neuroscience*, 29:449–476.

[81] Restom, K., Bangen, K. J., Bondi, M. W., Perthen, J. E., and Liu, T. T. (2007). Cerebral blood flow and BOLD responses to a memory encoding task: A comparison between healthy young and elderly adults. *NeuroImage*, 37(2):430–439.

[82] Roman, R. J. (2002). P-450 metabolites of arachidonic acid in the control of cardiovascular function. *Physiological reviews*, 82(1):131–185.

[83] Roy, C. S. and Sherrington, C. S. (1890). On the Regulation of the Blood-supply of the Brain. *The Journal of physiology*, 11:85–158.17.

[84] Rubaj, A., Zgodziński, W., and Sieklucka-Dziuba, M. (2003). The epileptogenic effect of seizures induced by hypoxia: The role of {NMDA} and ampa/ka antagonists. *Pharmacology Biochemistry and Behavior*, 74(2):303 – 311.

[85] Schridde, U., Khubchandani, M., Motelow, J. E., Sanganahalli, B. G., Hyder, F., and Blumenfeld, H. (2008). Negative BOLD with large increases in neuronal activity. *Cerebral Cortex*, 18:1814–1827.

[86] Schulte, M. L., Wood, J. D., and Hudetz, A. G. (2003). Cortical electrical stimulation alters erythrocyte perfusion pattern in the cerebral capillary network of the rat. *Brain Research*, 963(1-2):81–92.

[87] Schummers, J., Yu, H., and Sur, M. (2008). Tuned responses of astrocytes and their influence on hemodynamic signals in the visual cortex. *Science (New York, N.Y.)*, 320(5883):1638–43.

[88] Shih, A. Y., Driscoll, J. D., Drew, P. J., Nishimura, N., Schaffer, C. B., and Kleinfeld, D. (2012). Two-photon microscopy as a tool to study blood flow and neurovascular coupling in the rodent brain. *Journal of cerebral blood flow and metabolism : official journal of the International Society of Cerebral Blood Flow and Metabolism*, 32 7:1277–309.

[89] Shmuel, A., Augath, M., Oeltermann, A., and Logothetis, N. K. (2006). Negative functional MRI response correlates with decreases in neuronal activity in monkey visual area V1. *Nature neuroscience*, 9:569–577.

[90] Siero, J. C., Bhogal, A., and Jansma, J. M. (2013). Blood Oxygenation Level–dependent/Functional Magnetic Resonance Imaging: Underpinnings, Practice, and Perspectives. *PET Clinics*, 8(3):329–344.

[91] Siero, J. C. W., Hendrikse, J., Hoogduin, H., Petridou, N., Luijten, P., and Donahue, M. J. (2015). Cortical depth dependence of the BOLD initial dip and poststimulus undershoot in human visual cortex at 7 Tesla. *Magnetic Resonance in Medicine*, 73(6):2283–2295.

[92] Sobey, C. G. and Faraci, F. M. (1997). Effects of a novel inhibitor of guanylyl cyclase on dilator responses of mouse cerebral arterioles. *Stroke*, 28(0039-2499 (Print)):837–842.

[93] Stefanovic, B., Hutchinson, E., Yakovleva, V., Schram, V., Russell, J. T., Belluscio, L., Koretsky, A. P., and Silva, A. C. (2008). Functional reactivity of cerebral capillaries. *Journal of cerebral blood flow and metabolism : official journal of the International Society of Cerebral Blood Flow and Metabolism*, 28(5):961–972.

[94] Sukhotinsky, I., Dilekoz, E., Moskowitz, M. A., and Ayata, C. (2008). Hypoxia and hypotension transform the blood flow response to cortical spreading depression from hyperemia into hypoperfusion in the rat. *Journal of Cerebral Blood Flow and Metabolism*, 28:1369–1376.

[95] Taylor, F. R. (2007). Cortical spreading depression causes and coincides with tissue hypoxia.

[96] Traub, R. D., Jefferys, J. G., Miles, R., Whittington, M. A., and Tóth, K. (1994). A branching dendritic model of a rodent CA3 pyramidal neurone. *The Journal of physiology*, 481 (Pt 1):79–95.

[97] Vaishnavi, S. N., Vlassenko, a. G., Rundle, M. M., Snyder, a. Z., Mintun, M. a., and Raichle, M. E. (2010). Regional aerobic glycolysis in the human brain. *Proceedings of the National Academy of Sciences*, 107(41):17757–17762.

[98] Van Zijl, P. C. M., Hua, J., and Lu, H. (2012). The BOLD post-stimulus undershoot, one of the most debated issues in fMRI. *NeuroImage*, 62:1092–1102.

[99] Ventura, R. and Harris, K. M. (1999). Three-dimensional relationships between hippocampal synapses and astrocytes. *The Journal of neuroscience : the official journal of the Society for Neuroscience*, 19(16):6897–6906.

[100] Yemisci, M., Gursoy-Ozdemir, Y., Vural, A., Can, A., Topalkara, K., and Dalkara, T. (2009). Pericyte contraction induced by oxidative-nitrative stress impairs capillary reflow despite successful opening of an occluded cerebral artery. *Nature medicine*, 15(9):1031–1037.

[101] Zamir, M. and Budwig, R. (2002). *Physics of Pulsatile Flow*, volume 55.

[102] Zheng, Y., Pan, Y., Harris, S., Billings, S., Coca, D., Berwick, J., Jones, M., Kennerley, A., Johnston, D., Martin, C., Devonshire, I. M., and Mayhew, J. (2010). A dynamic model of neurovascular coupling: implications for blood vessel dilation and constriction. *NeuroImage*, 235:1135–1147.

[103] Zonta, M., Angulo, M. C., Gobbo, S., Rosengarten, B., Hossmann, K.-A., Pozzan, T., and Carmignoto, G. (2003). Neuron-to-astrocyte signaling is central to the dynamic control of brain microcirculation. *Nature neuroscience*, 6(1):43–50.

.1 Model code

You can go to the page containing the code by clicking on the line below.
Code of BOLD model